Friedrich Lindebner, BSc

Spectroscopic Investigation of Cu and Cr Doped Helium Nanodroplets

MASTER THESIS

For obtaining the academic degree
Diplom-Ingenieur

Master Programme of
Technical Physics

Graz University of Technology

Supervisor: Univ.-Prof. Dipl.-Phys. Dr.rer.nat. Wolfgang E. Ernst

Institute of Experimental Physics

Graz, October 2013

Abstract

Superfluid helium nanodroplets (He_N) offer an unique environment for the spectroscopic investigation of atoms, molecules and clusters. During the course of this work copper and chromium doped He_N were investigated by exploiting both mass- and optical spectroscopy. Preliminary measurements concerned the heating and doping characteristics of a Cu evaporation source. Mass spectra of doped He_N revealed that small copper clusters were formed, including up to seven atoms. With the sequential doping of He_N with Cu and Cr the formation of mixed Cr_nCu_m clusters was achieved and the optimal pickup conditions for different Cu cluster sizes were examined.

Electronic excitation spectra in the region of the Cu $^2P_{1/2,3/2} \leftarrow {}^2S_{1/2}$ transition were obtained exploiting the Photoionisation (PI) and Beam Depletion (BD) methods. The PI and BD spectra show similar droplet broadened absorption features, which is characteristic for atoms submerged in He_N. The appearance of sharp lines at the energies of the free atom transitions in the PI spectrum suggests the ejection of a portion of the dopants by the interaction with the ionising laser. The recorded spectra were compared with simulated absorption spectra from literature which turned out to be in good agreement.

Zusammenfassung

Supraflüssige Heliumnanotröpfchen (He_N) bieten eine einzigartige Umgebung zur spektroskopischen Untersuchung von Atomen, Molekülen und Clustern. Im Zuge dieser Arbeit wurden Kupfer und Chrom dotierte He_N mit Hilfe von massenspektroskopischen und optischen Methoden untersucht. Es wurden die Heiz- und Dotiereigenschaften einer Verdampfungsquelle zur Einbringung von Kupfer in die Tröpfchen untersucht. Von den dotierten Heliumtröpfchen wurden Massenspektren aufgenommen, welche die Bildung von Kupferclustern mit bis zu sieben Atomen bestätigen. Das sequentielle Dotieren der Tröpfchen mit Kupfer und Chrom führte zur Bildung von gemischten Cr_nCu_m Clustern, wobei in einem weiteren Schritt die optimalen Rahmenbedingungen für die Entstehung verschiedener Clustergrößen bestimmt wurden.

Die elektronischen Anregungsspektren im Bereich des Cu $^2P_{1/2,3/2} \leftarrow {}^2S_{1/2}$ Übergangs wurden mit Hilfe von Photoionisationsspektroskopie (PI) und Beam Depletion (BD) bestimmt. Sowohl das PI als auch das BD Spektrum zeigen tropfenverbreiterte Absorptionsbereiche, charakteristisch für ein Fremdatom im Inneren eines He_N. Die Anwesenheit scharfer Absorptionslinien an den Positionen der freien Atomübergänge im PI Sepktrum legt den Schluss nahe, dass einige der Cu Atome durch die Wechselwirkung mit dem Ionisationslaser aus dem Tropfen geschleudert und als freie Atome ionisiert werden. Die aufgenommenen Spektren wurden mit simulierten Absorptionen aus der Literatur verglichen, wobei eine gute Übereinstimmungen der Ergebnisse festgestellt wurde.

Danksagung

An dieser Stelle seien all jene Personen erwähnt, die mir bei der Durchführung und Fertigstellung dieser Arbeit mit Rat und Tat zur Seite standen.

Bei Herrn Univ.-Prof. Dipl.-Phys. Dr.rer.nat. Wolfgang E. Ernst möchte ich mich dafür bedanken, dass er mir ermöglichte meine Masterarbeit am Institut für Experimentalphysik zu absovieren und mir dabei als Betreuer wertvolle Ratschläge geben konnte.

Andreas Kautsch möchte ich für den fortwährenden Beistand während der gesamten Arbeit danken. Vor allem dafür, dass er bei allen Messungen mit dabei war und auch an oft zermürbenden Messtagen nie die Freude an der Arbeit verlor und mich somit mitreißen konnte. Weiters möchte ich ihm auch für das ausführliche Korrekturlesen dieser Arbeit danken.

Bei meinen Labornachbarn Florian Lackner und Günter Krois möchte ich mich für die Geduld bedanken, die sie bei der Beantwortung meiner unzähligen “Wo ist das?”- und “Wie funktioniert das?”-Fragen aufgebracht haben.

Weiters danke ich allen Kolleginnen und Kollegen des Instituts für das sehr freundliche und angenehme Arbeitsumfeld.

Zum Schluss möchte ich meiner Familie und meinen Freunden danken, die nach langen Messtagen für den nötigen Ausgleich sorgten.

Deutsche Fassung:
Beschluss der Curricula-Kommission für Bachelor-, Master- und Diplomstudien vom 10.11.2008
Genehmigung des Senates am 1.12.2008

EIDESSTATTLICHE ERKLÄRUNG

Ich erkläre an Eides statt, dass ich die vorliegende Arbeit selbstständig verfasst, andere als die angegebenen Quellen/Hilfsmittel nicht benutzt, und die den benutzten Quellen wörtlich und inhaltlich entnommenen Stellen als solche kenntlich gemacht habe.

Graz, am ……. ……..
(Unterschrift)

Englische Fassung:

STATUTORY DECLARATION

I declare that I have authored this thesis independently, that I have not used other than the declared sources / resources, and that I have explicitly marked all material which has been quoted either literally or by content from the used sources.

……. ……..
date (signature)

Contents

List of Figures

List of Tables

1 Introduction

Transition metal clusters exhibit outstanding properties, somewhere in between those of the atom and the bulk. These clusters are used for the realisation of highly active catalysts, quantum dots, and ferrofluids for cell-separation, just to name a few [1]. Superfluid He_N provide a perfect environment for the preparation and investigation of such clusters at a temperature of as low as 0.38 K [2]. The transparency of helium allows spectroscopic investigations over a wide spectral range from UV to IR and the incorporation of dopants into the helium droplets from the gas phase enables one to dope virtually any species to He_N that can be vaporised. Many measurements concerning elementary materials on He_N have been carried out concerning alkaline metals and alkaline earth metals, whereas he number of examined transition metals is very low, compared to the number of available species[1].

The doping of Cu to He_N was first reported by Stiles and Miller who investigated the bonding of Cu clusters to the HCN molecule [3] and there exist many publications on the matrix isolation spectroscopy of Cu [4–6]. Another technique used to study the interaction of copper with He is the spectroscopic study of Cu atoms injected into a fountain of superfluid He [7]. A computational study on the solubility of copper in helium was carried out by Mella and Cargnoni, who also calculated absorption spectra [8]. As well, the formation of big, unusual Cu clusters in He_N was very recently studied [9].

This master thesis focuses on the spectroscopic investigation of Cu and Cr doped He_N. Along with an analysis of small Cu and mixed CrCu clusters, it contains the first experimentally determined electronic excitation spectra of Cu doped He_N. The spectra were obtained using the beam depletion and

[1] A list of investigated materials doped to helium droplets can be found in reference [2].

photoionisation techniques.

The measurements for this thesis were carried out on a Helium Nanodroplet Isolation (HENDI) apparatus which was adapted from a molecular beam apparatus by Markus Koch during his doctoral thesis [10]. This is the same apparatus where Cr was doped to He_N for the first time [11, 12].

This thesis is structured into six chapters. Chapter two deals with the theoretical background where special attention is paid to electronic excitations, the droplet-dopant interaction, and photoionisation. The experimental setup used for the measurements is described in chapter three. All results are presented in chapter four and discussed in chapter five, where the latter includes a comparison of measured spectra with available literature. In the final chapter the conclusions are summarised and an outlook on possible topics for further investigation is given. Some practical aspects of my work are enclosed in the appendix.

2 Theoretical Background

In the following section the theoretical background, required to interpret the results in this work, will be discussed. The focus is on mass spectroscopy, electronic excitations, and photoionisation. As well, the interaction of dopant and droplet will be considered and informations about the technique itself will be presented.

2.1 Superfluid Helium Nanodroplets

Helium is the lightest of the noble gas atoms and the second most abundant element in the universe [13]. It has the unique property of not forming a solid at low temperatures but instead undergoing a radical change to a superfluid phase below 2.186 K [13]. Within this work superfluid helium nanodroplets (He_N) are used as a nano-matrix for HENDI spectroscopy. The main focus of this thesis is therefore on the doped droplet and less on the droplet itself. In this section some basic properties and applications of He_N will be mentioned. For a more detailed consideration, I want to refer to the review articles [2] and [14] and the references therein.

A beam of He_N is produced by the expansion of high pressure He into a vacuum vessel through a cooled nozzle. Typical conditions for this expansion are a nozzle diameter (d_{nozzle}) of 5 µm, a helium nozzle pressure (p_{He}) of 50 bar and a nozzle temperature (T_{nozzle}) of $10 - 20$ K. Due to this free jet expansion the gas-phase He is adiabatically cooled and clusters are formed by condensation.

These clusters are then further cooled by evaporation of He atoms from the droplet surface at a very high cooling rate. The temperature levels out at a value of 0.38 K after a time of approximately 10^{-4} s [2]. The temperature of the droplet is henceforth fixed to this value by further evaporative cooling. This is of special interest when energy is transferred to the droplet for example by means of incorporation of a dopant atom or molecule. Every time energy is transferred to the droplet, He atoms are evaporated from its surface and the droplet shrinks. Because of this fixed temperature He_N are also referred to as nano-cryostats. The number of He atoms detached can be estimated by the bulk liquid He binding energy, which has a value of [15]

$$E_{He_n-He} = 5\,\mathrm{cm}^{-1}. \tag{2.1}$$

So 1 eV of energy introduced in the system leads to the evaporation of 1600 He atoms. With this low temperature the superfluidity of He_N was predicted and could be shown by Hartmann et al. [16] with the observation of rotational constants of SF_6.

HENDI-spectroscopy is sometimes specified as a mixture of inert-gas matrix spectroscopy and molecular beam spectroscopy that combines the advantages of both techniques. This is reasonable since every droplet acts as a nano-matrix while it travels through the vacuum vessel like molecules in an usual molecular beam do. Temperatures in the sub-Kelvin region are also feasible in solid inert gas matrices, however, the effect of the host on the dopant tends to be much higher in solid matrices than it is in He_N. As an example, there are no secondary trapping sites in He_N but they share the important property of transparency over a wide spectral range with inert-gas matrices.

The possibility of relatively easy and controlled doping of He_N by the pickup of atoms out of the gas phase in a pickup-cell, offers the chance to tailor-make molecules and clusters. As the dopants move freely inside or on the surface of the droplet, weak Van-der-Waals interactions are sufficient to lead to the agglomeration of atoms and molecules.

Due to these special properties of He_N it is possible to analyse states of atoms and molecules which are hard to access with other techniques. One example

is the spectroscopy of alkali and silver dimers in their high spin triplet states [17, 18]. Also very unstable compounds might be analysed and subsequent pickup of two different species offers the possibility to form so called core-shell structures [19].

From the conditions of the droplet formation (d_{nozzle}, p_{He}, T_{nozzle}) one is able to estimate the mean number of He atoms per droplet to be [10]

$$\bar{N} = k_1 \cdot {p_{He}}^{k_2} \cdot {T_{nozzle}}^{k_3} \cdot {d_{nozzle}}^{k_4} \tag{2.2}$$

$$k_1 = 4 \cdot 10^5,\ k_2 = 0.97,\ k_3 = -3.88,\ k_4 = 2$$

As the temperature has a negative exponent in Equation 2.2, a higher nozzle temperature corresponds to smaller droplets. Application of this formula to the usual conditions stated above results in a mean droplet size between $4 \cdot 10^3$ and $4 \cdot 10^4$ He atoms. Although, there is a wide range of droplet sizes corresponding to one nozzle temperature described by a log-normal distribution [20]. The diameter of the droplets can be evaluated if they are assumed to have the same density as bulk liquid He [2]. Using

$$R = 2.22\text{Å} \cdot \bar{N}^{1/3} \tag{2.3}$$

leads to a droplet diameter in the range of 7 nm to 15 nm, corresponding to nozzle temperatures of 20 K to 10 K, respectively.

The droplet velocity can be calculated by thermodynamic considerations, which are explained in detail in reference [12]. The resulting velocities are in the range of a few hundred meters per second. For a HENDI apparatus with a length of about two meters this results in a droplet flight time of several milliseconds where at the end they collide with the vacuum chamber wall and evaporate.

2.2 Copper [13]

The name "copper" originates from the Latin word *cuprum* which stands for the island Cyprus. Cu is known to mankind since historic ages and is one of the technically most important metals, for example it is the main part of the alloys brass and bronze. For modern applications Cu is widely used in electric circuits due to its high conductivity. In the periodic table Cu is situated in group eleven along with the other coinage metals gold and silver. The electron configuration of Cu is $[Ar]3d^{10}4s^1$ leading to a $^2S_{1/2}$ ground state which is therefore similar to that of alkali atoms. Some basic physical properties of Cu are:

Atomic number: 29

Abundant isotopes: ^{63}Cu (69.15%) and ^{65}Cu (30.85%)

Melting point: 1358 K

Boiling point: 2385 K

First ionisation energy: 62317.46 cm^{-1}

For the doping process the vapour pressure of Cu is of interest. It can be calculated using the following formula and constants [13]:

$$\log p = 5.006 + A + BT^{-1} + C \log T + DT^{-3} \tag{2.4}$$

For 298 K $< T <$ 1357.77 K (solid): A = 9.123; B = -17748; C = -0.7317; D = 0;

For 1357.77 K $< T <$ 1850 K (liquid): A = 5.849; B = -16415; C = -0.7317; D = 0;

Where p is the pressure in Pascal and T is the temperature in Kelvin.

Figure 2.1 shows the calculated vapour pressures of Cu and Cr. Stiles and Miller [3] state evaporation temperatures of 1030 °C, 1130 °C and 1200 °C for the pick up of one, two or three Cu atoms, respectively, that results in vapour pressures between 10^{-3} mbar and 10^{-2} mbar. Comparing this with chromium (see section 3.3), it is clearly evident that Cr has a lower vapour pressure

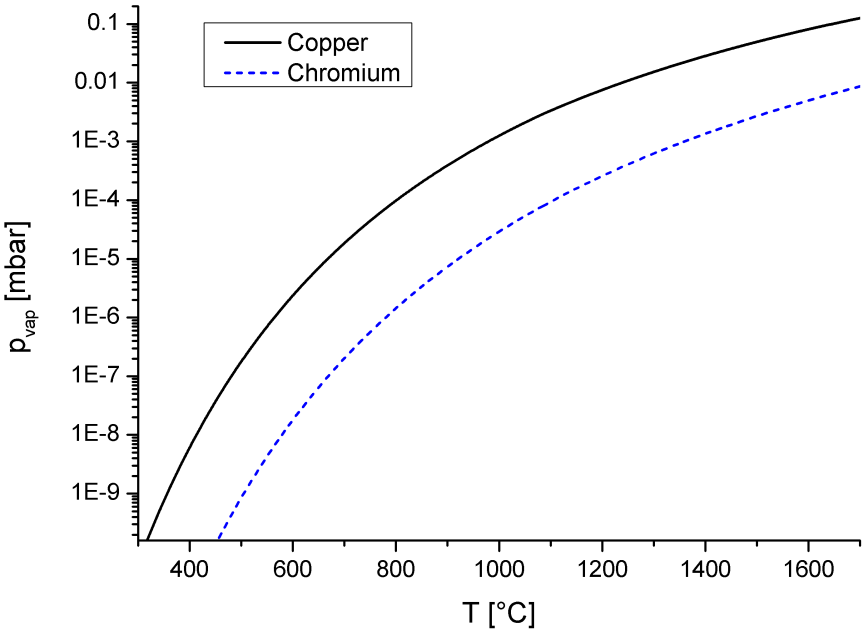

Figure 2.1: Vapour pressures of Cu and Cr calculated using equation 2.4 and converted to the units stated.

than Cu at all temperatures. Due to this fact the doping of Cr is technically more demanding than that of Cu. To reach a vapour pressure of the order of 10^{-3} mbar a Cr source temperature of 1350 °C has to be reached. The whole process of droplet doping and the experimental setup is described in section 3.3.

During the experiments several transitions between electronic energy levels of Cu were observed. Figure 2.2 shows a Grotrian diagram of Cu which includes all states below the ionisation limit and the properties of all accessed states are summarised in table 2.1. A detailed discussion of all considered transitions is provided in the chapters 4 and 5.

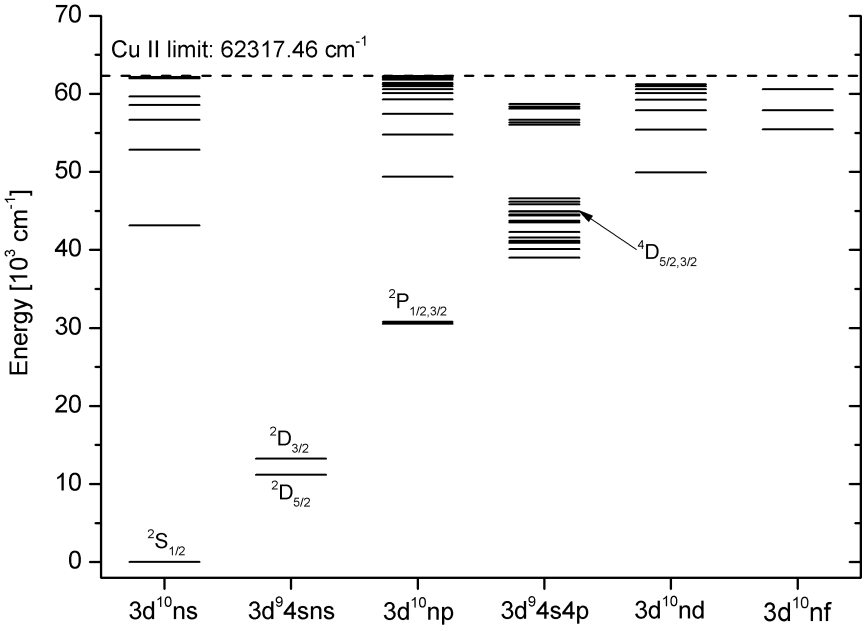

Figure 2.2: Grotrian diagram of Cu including all states below the ionisation limit. States that are important for the discussion of the results are explicitly labeled. (Energies from reference [21])

Table 2.1: Electron configurations of accessed Cu states [21].

state	energy [cm^{-1}]	electron configuration	parity
$^2S_{1/2}$	0	[Ar]$3d^{10}4s$	even
$^2D_{5/2}$	11202.565	[Ar]$3d^94s^2$	even
$^2D_{3/2}$	13245.423	[Ar]$3d^94s^2$	even
$^2P_{1/2}$	30535.302	[Ar]$3d^{10}4p$	odd
$^2P_{3/2}$	30783.686	[Ar]$3d^{10}4p$	odd
$^4D_{5/2}$	44406.268	[Ar]$3d^94s4p$	odd
$^4D_{3/2}$	44544.153	[Ar]$3d^94s4p$	odd

2.3 Chromium [13]

The name "chromium" originates from the Greek word *chroma*, meaning *colour* because various Cr compounds have intense colours used as pigments in paints. Bulk Cr is paramagnetic at ambient temperatures, a single Cr atom however has a very high magnetic moment of six Bohr magnetons due to its six unpaired spins. There exist also ferromagnetic materials consisting of chromium and

palladium [22]. For all of these reasons, Cr is a very profitable subject for magnetic measurements.

Some basic physical properties of Cr are:

Atomic number: 24

Electron configuration: $[Ar]3d^5 4s^1$

Ground state: a^7S_3

Abundant isotopes: ^{52}Cr (83.8%), ^{53}Cr (9.5%), ^{50}Cr (4.3%,) and ^{54}Cr (2.4%)

Melting point: 2180 K

Boiling point: 2755 K

First ionisation energy: $54578\,cm^{-1}$

The vapour pressure of Cr is depicted in figure 2.1. Due to the high multiplicity, the electronic spectrum of a Cr atom is a lot more complicated than that of the Cu atom so the interpretation of electronic transitions can be a very demanding task.

2.4 CrCu Mixed Metal Dimer

M. Wang, B. Wang, and Z. Chen state in the introduction of their publication on the magnetic coupling of CrCu (2007):

> "Among these mixed transition metal dimers, the CrCu molecule is one of the least understood systems both experimentally and theoretically." [23]

This proclamation refers to the fact that only few investigations of the CrCu molecule have yet been carried out. The dissociation energy has been determined

by mass spectrometric methods and is found to be [24]

$$E_{diss} = (12000 \pm 2000)\,\mathrm{cm}^{-1} \tag{2.5}$$

Several Electron Spin Resonance (ESR) experiments were carried out in rare gas matrices [25–27] leading to three different ground state assignments, which highlights the complexity of the system. Ultimately, the ground state was found to be $X^6\Sigma^+$ [23]. A few more works concerning the CrCu molecule are cited in reference [23], giving a good overview of the topic.

The formation of small mixed CrCu clusters, after subsequent pickup of both species by He_N, is studied in this thesis by means of mass spectrometric techniques (see section 4.2).

2.5 Interaction of Dopant and Droplet

Out of all cryogenic matrices used in spectroscopy, superfluid He and especially He_N show the weakest interaction with a dopant [14]. Nevertheless, there is a certain amount of influence on the dopant behaviour. The theoretic framework for the consideration of interactions between impurities and a liquid He matrix is represented by the *Atomic Bubble Model* proposed by J. Jortner et al. in 1965 [28]. The main statement of this work is that impurities in bulk liquid He are surrounded by a void bubble and that additional energy, required for the bubble-formation, is responsible for the blue-shift in optical spectra. Moroshkin et al. published a paper on *Atomic and Molecular Defects in Solid ^{4}He* [29], which is the source of the following statements. The interaction of the dopant with the surrounding He is a quantum-mechanical many body problem. Such big systems tend to be intractable and several simplifications need to be made. Fortunately, the very nature of He suggests two reasonable simplifications. Due to the strong overlap of the He wave functions, condensed He can be treated as a continuous medium. The fact that the Pauli repulsion between impurity and He is by far stronger than the He-He interaction can be used to further simplify

the problem. This strong repulsion leads to the formation of a bubble around the impurity [28]. The size of the bubble is determined by the equilibrium between the repulsive energy and the energy associated with the formation of such a bubble. According to reference [29], the energy of the dopant-bubble system is given by

$$E_{tot} = E_{int} + pV_{bubble} + \sigma S_{bubble} + \frac{\hbar}{8m_{He}} \int \frac{(\Delta\rho(R))^2}{\rho(R)} d^3R \qquad (2.6)$$

where E_{int} represents the interaction energy between the dopant and the droplet, the second term is the pressure-volume work required for the formation of the bubble (p... He pressure, V_{bubble}... bubble volume), the third term represents the surface tension energy of the bubble (σ... surface tension parameter, S_{bubble}... bubble surface area), and the last term stands for the volume kinetic energy and can be attributed to the localisation of He atoms at the bubble interface ($\rho(R)$... He density, m_{He}... He mass). A bubble radius of 4.0 Å is reported for a Cu atom in superfluid helium [6] and, using a Diffusion Monte Carlo (DMC) method, Cargnoni and Mella [8] find that the Cu atom resides in a He cavity with a radius of 3 Å.

The atomic bubble model is able to describe the shape of electronic transition lines of atoms embedded in a He environment. Relying on the Frank-Condon principle, one can assume that shape and size of the bubble do not change during an electronic excitation as electronic transitions and the motion of an ensemble of atoms happen on very different time scales [29]. The electronic orbitals of the initial and the final state of the transition usually have unequal spatial extensions, therefore, the electron orbital changes its distance to the bubble surface which changes the interaction energy in equation 2.6. This energy manifests in a shift of the transition energy, where absorptions are usually blue shifted. This explains the shifts in the spectra recorded in chapter 4. Line broadening can be attributed to the coupling of the dopant wave function to oscillation modes of the bubble [29].

2.6 Electronic Transitions [30]

In the results section of this thesis different electronic excitation spectra of Cu doped He_N are presented and discussed. These spectra were recorded with different spectroscopic methods, which are all based on resonant laser excitation of the dopant atom. A resonant electronic transition occurs when the energy of the incident photon matches the gap between two discrete states of the atom. To express this in a more mathematical manner

$$h\nu = E_i - E_f \tag{2.7}$$

where h is Planck's constant, ν is the frequency of the incident photon, E_i is the energy of the ground state, and E_f is the energy of the excited state. In experiments (see for example figure 4.15), transitions lines have a finite line width that would not be expressed by equation 2.7 if the states had only one defined energy. With the Heisenberg uncertainty principle one of several mechanisms accountable for line broadening can be explained. As the stationary states have finite lifetime, also their energy has a finite uncertainty according to

$$\tau \cdot \Delta E \geq \hbar \tag{2.8}$$

where τ is the lifetime of the state, ΔE is the energy uncertainty, and $\hbar$ is Planck's constant divided by 2π. Due to the energy deviation of the atomic states there is a lower limit for the linewidth of an atomic transition. Usually this natural linewidth is by far exceeded when additional line broadening mechanisms are taken into account. The most important line broadening mechanism in He_N is the interaction of the dopant with the surrounding environment. The droplet broadening is about six orders of magnitude higher than the natural linewidth.

The energy of the states in an atom with N electrons is described by the stationary Schrödinger equation

$$\hat{H}\psi = E\psi \tag{2.9}$$

with a Hamiltonian of the form

$$\hat{H} = -\frac{\hbar^2}{2m_e}\sum_{j=1}^{N}\nabla_j{}^2 - \sum_{j=1}^{N}\frac{Ze^2}{4\pi\epsilon_0 r_j} + \frac{1}{2}\sum_{j=1}^{N}\sum_{j\neq k}^{N}\frac{e^2}{4\pi\epsilon_0|r_j - r_k|} \tag{2.10}$$

where the first term corresponds to the kinetic energy of the electrons, the second one describes the Coulomb interaction of the electron with the nucleus, and the last term takes the electron-electron interaction into account. This problem is only analytically solvable for $N = 1$ electron, respectively the hydrogen atom. For multi-electron atoms, approximations need to be made. Therefore approximate solutions for the electron wave-functions can be gained from the Schrödinger equation

$$\hat{H}\psi_n = E_n\psi_n \tag{2.11}$$

The solutions ψ_n of equation 2.11 are totally anti-symmetric products of N single electron wave-functions and as such characterised by N sets of quantum numbers (n, l, m_l, s, m_s). In the case of the Cu ground state the electronic configuration reads as

$$1s^2 2s^2 2p^6 3s^2 3p^6 3d^{10} 4s^1 \quad \text{or short} \quad [Ar]3d^{10}4s^1 \tag{2.12}$$

For the nomenclature of states in multi-electron atoms the sets of quantum numbers are organised into term-symbols. These term symbols have the form

$${}^{2S+1}L_J \tag{2.13}$$

where S is the total spin quantum number, L is the total angular momentum quantum number, and J is the total orbital momentum quantum number. The expression $(2S + 1)$ is also referred to as the multiplicity. For Cu the ground state term symbol is

$${}^2S_{1/2} \tag{2.14}$$

that can be deduced from the ground state electron configuration by the application of Hund's rules, namely:

1. For a given electron configuration the ground state term is the one with

the maximum multiplicity.

2. For a given multiplicity the term with the highest L is lowest in energy.

3. If the outermost shell is less than half filled the state with the lowest J is the ground state; if the outermost shell is more than half filled the state with the highest J is the ground state.

In the case of Cu only the 4s electron is in an unfilled electronic shell and is therefore the only one to be considered, what makes the job a lot easier. The spin of a single electron is $1/2$, therefore, the multiplicity equals two. The angular momentum of the s electron is zero so the symbol is S and the orbital momentum equals the sum of the spin ($1/2$) and the orbital momentum (0) which gives $1/2$.

The rate at which transitions between states occur can be calculated with Fermi's golden rule that can be written as

$$\Gamma_{i\to f} = \frac{2\pi}{\hbar}\rho(E_f)|\langle f|H_T|i\rangle|^2 \tag{2.15}$$

where $\Gamma_{i\to f}$ is the transition rate between the initial (i) and the final (f) state, $\rho(E_f)$ is the density of final states and H_T is the transition Hamiltonian. In the case of interaction with electro-magnetic radiation the transition Hamiltonian is the dipole operator[1] μ and the transition matrix element reads as

$$\langle f|H_T|i\rangle = \int_{-\infty}^{\infty} \psi_f^* \mu \psi_i d^3r. \tag{2.16}$$

For a transition to occur, the transition rate has to be non-zero that can only be the case if the transition matrix element is non-zero. Therefore, the transition rules explained in the following section can be deduced from equation 2.16.

[1] Only in case of the electric dipole approximation. To obtain electric and magnetic multi-pole transitions a more general approach has to be used.

2.7 Selection Rules [31]

The dipole selection rules for electronic transitions can be extracted from the transition matrix element in equation 2.16. The right side of this equation represents an integral over the whole space that equals zero if the integrand function is odd. The dipole operator is proportional to the position operator and is therefore odd. This means that the product of the initial and the final wave-function has to be odd to obtain an even integrand and a non-zero transition rate, so the parity of the wave-function has to change in dipole allowed transitions. A multi-electron state has odd parity if an odd number of electrons resides in orbitals with an odd angular momentum. Therefore, the angular momentum has to change during an electric dipole transition. This can also be interpreted in terms of conservation of momentum. As the absorbed photon has an angular momentum of one, the angular momentum of the initial and the final state need to differ by one. The first selection rule reads as

$$\Delta l = \pm 1 \tag{2.17}$$

This rule is true for one-electron transitions, in the case of multi-electron atoms there might be more than one electron involved in a transition. The more general rule is that during a transition

parity has to change.

The transition Hamiltonian has no part that affects the electron spin, so the spin of the initial and the final state need to be identical, as the integral over the orthogonal spin functions would otherwise equal zero. The spin selection rule is therefore

$$\Delta s = 0, \tag{2.18}$$

meaning that spin does not change during electric dipole transitions so that there are no transitions allowed between states with different multiplicities. This rule is only restrictive in the regime of LS-coupling which holds for light atoms. For bigger atoms this selection rule becomes more and more softened and intercombination transitions between states of different multiplicity become

more probable. Two intercombination transitions between the quartet and the doublet multiplicity system are visible in the photoionisation spectrum of Cu doped He_N (figure 4.15).

The third selection rule restricts the change of the total orbital momentum J. It takes into account that although the total spin does not change, the direction of the spin with respect to the angular momentum might change and therefore compensates the change in angular momentum.

$$\Delta J = 0, \pm 1 \tag{2.19}$$

There is also a fourth selection rule concerning the magnetic quantum number m, stating that $m = 0, \pm 1$. In the absence of a magnetic field these sub-states are degenerate. As this is the case for all experiments presented in this work, this rule is not of concern for interpreting the results.

2.8 Photoionisation

Photoionisation (PI) is the process of ionising an atom or molecule with the help of electromagnetic radiation. In other words, an electron is detached from an atom or molecule by the energy of a photon. This can be expressed like this:

$$At + \hbar\omega \rightarrow At^+ + e^- + E_{kin} \tag{2.20}$$

where ω is the angular frequency of the incident photon and E_{kin} is the kinetic energy of the electron. The ionisation process is only possible if the energy of the incident photon is high enough to overcome the ionisation potential, the energy required to remove an electron from an atom or molecule. From the conservation of energy, the excess kinetic energy is

$$E_{kin} = \hbar\omega - E_{IP} = \frac{\hbar^2 k^2}{2m_e}, \tag{2.21}$$

where E_{IP} is the ionisation potential of the atom or molecule and k is the wave vector. PI can be considered as a transition of an electron from a bound discrete state to a free continuum state with a momentum k corresponding to the kinetic energy.

In PI spectroscopy with lasers usually two subsequent transitions lead to ionisation of the atom that can be detected with any kind of ion detector. The first step is a resonant transition between two states of an atom, resulting in an excited atom. By absorption of a second photon the atom is further excited over the ionisation threshold and therefore ionised. If the two photons have the same wavelength the process is called one Colour Resonant two Photon Ionisation (1CR2PI), if they are of different wavelength it is called two Colour Resonant two Photon Ionisation (2CR2PI). The way to obtain an excitation spectrum with this technique is to scan the wavelength of a laser that provides the photons for the first resonant excitation step. If the wavelength matches with an allowed transition of the atom the detected ion yield increases. PI spectra that were obtained this way are presented and discussed in sections 4.5 and 5, respectively.

2.9 Relaxations in Helium Nanodroplets

After the excitation of an atom there are usually two ways of relaxation to its ground state, fluorescence and non-radiative relaxation. In the case of fluorescence the excited state's energy is carried away in the form of a photon. This is the preferred relaxation mechanism for gas-phase atoms. However, fluorescence might be suppressed, like in the case of metastable states where the optical transition is dipole forbidden. In this case radiative transitions are still possible but far less likely via electric or magnetic multi-pole transitions and multi-photon mechanisms. In the case of non-radiative relaxation, the atom's excess energy is lost via coupling to other atoms, for example by a collision in the gas phase or by phonons in a solid.

For an excited dopant inside or on the surface of a He_N, alongside fluorescence [32] and non-radiative relaxation, but also ejection and relaxation outside the droplet are possible. The question if a dopant submerges into the droplet or not, may be answered by examining the dopant-helium pair potential [33]. As this potential significantly depends on the dopant's electron configuration, a species that is submerged in its ground state might be ejected upon excitation, leaving the bare dopant atom in the gas phase [8]. Similar effects occur to species that are attached to the surface of He_N [34].

It seems likely that fluorescence is quenched and selection rules are weakened inside He_N, as similar effects are found in rare gas matrices [5]. Therefore, the possible ejection of dopants changes the available relaxation paths, because after ejection the free atom selection rules apply and the fluorescence is not quenched if allowed transitions are available.

3 Experimental Setup

In this chapter the experimental setup and the procedures used for the different measurement techniques are presented.

Figure 3.1a and 3.1b show a sketch and a picture of the HENDI apparatus, respectively. The apparatus consists of three main vacuum chambers, the **source chamber** where the He_N beam is generated (section 3.2), the **pickup chamber** where the droplets are doped (section 3.3), and the **measurement chamber** providing several access points for measurement devices (section 3.5). A Quadrupole Mass Spectrometer (QMS) is attached in a small separately pumped chamber at the end of the measurement chamber. The HENDI apparatus is described in detail in reference [10] and the properties of the parts labeled in the sketch are explained in the further sub-sections of this chapter.

In operation the cold-head situated in the source chamber is cooled down to below 20 K and helium is expanded through a 5 µm nozzle attached to it. After expansion the liquid droplets form and cool down to their characteristic temperature (0.38 K) [2]. To minimise the divergence of the droplet beam it is passed through a skimmer at the junction between the source chamber and the pickup chamber. In the pickup chamber the beam is chopped by a chopper wheel to obtain the possibility of background subtraction in the measurements. Then follows the dopant pickup as the beam passes two sequentially arranged evaporation cells. The first one is a Cr high-temperature electron-bombardment source which was designed by Martin Ratschek in the course of his master thesis and is described in detail in references [11] and [12]. The second source is the resistively heated Cu source, described more detailed in section 3.3. They can either be operated independently or simultaneously, resulting in He_N doped with pure or mixed metal clusters. The beam then passes on into the measurement

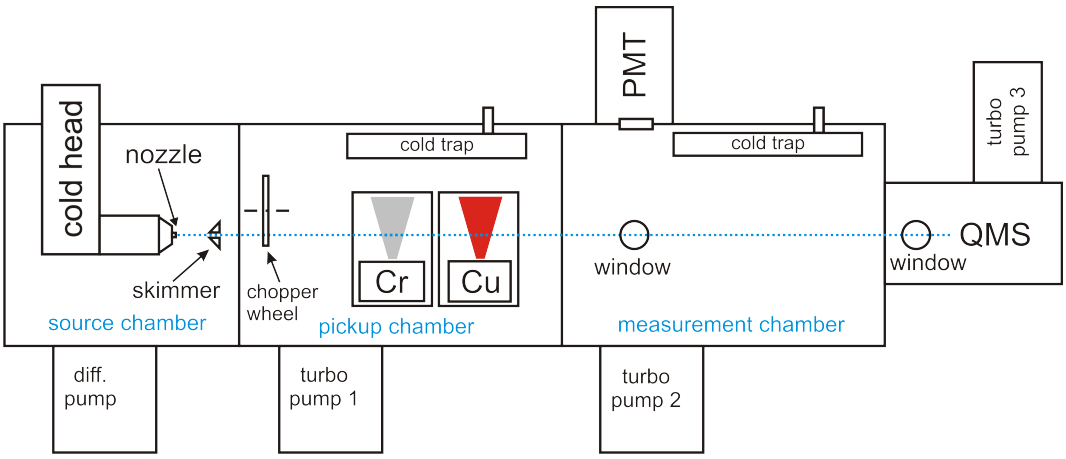

(a) Schematic sketch of the HENDI apparatus.

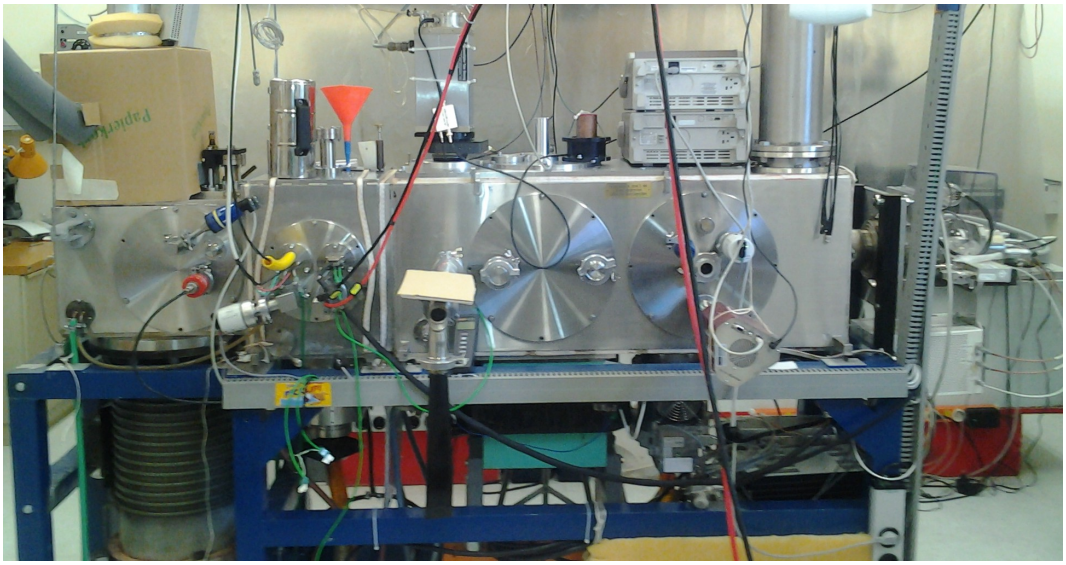

(b) Picture of the HENDI apparatus.

Figure 3.1: Comparison of a scetch and a picture of the HENDI apparatus.

chamber where it is analysed. All around this chamber measurement devices can be attached. During this work two of them where of major interest, namely the QMS and a Photomultiplier Tube (PMT) which is attached to an optical system for fluorescent light detection. The journey of the droplet beam ends after several milliseconds in the ionisation chamber of the QMS.

3.1 Vacuum System

A sufficient vacuum system is a prerequisite for the realisation of a HENDI apparatus, so there is the need for differentially pumped chambers. Due to the expansion of He into the vacuum the final pressure in the source chamber is a lot higher than in the other chambers and fairly high pump rates must be ensured.

To realise the high pump rate in the source chamber, an oil diffusion pump (Varian 0163) is used. It is backed by a roots pump (Oerlikon Leybold RuVac WS500) attached to a rotary vane pump (Alcatel T2 100SD). During the measurements a pressure of about 10^{-4} mbar is reached in this chamber, which is monitored with a cold cathode vacuum gauge (Leybold-Inficon 850-610-G2).

For the evacuation of the pickup- and measurement chamber two turbo molecular pumps (Leybold Torbovac 361 and Pfeiffer TMU251P) are used. The rough pump for both volumes is a rotary vane pump (Varian CD-700). In the pickup chamber pressures in the region of 10^{-6} mbar are achieved and measured with a full-range-gauge (Pfeiffer Vacuum PKR 251). The operation pressure in the measurement chamber is in the order of 10^{-7} mbar and is monitored with a full-range-gauge (Pfeiffer Vacuum PKR 250). The pickup chamber and the measurement chamber are equipped with liquid nitrogen cold traps for a further improvement of the vacuum.

The QMS chamber is pumped by a separate turbo molecular pump (Pfeiffer TMU065) backed up with a membrane pump (ABM) where pressures in the mid 10^{-8} mbar region are reached. The vacuum gauge is an ionisation gauge (Granville Phillips 274002).

The pressures stated above shall be understood as exemplary values, as these vary in accordance to the experimental conditions and preliminary preparation of the chamber (for example the time elapsed since the last flooding of the chamber or a bake-out of the chamber).

A residual gas analysis of the vacuum in the measurement chamber revealed that the most abundant residual gases are N_2, O_2, and H_2O. It shall also be mentioned that a fragment of the diffusion pump oil "alkyl-naphtalen" with a mass of 219 u [35] was detected in a PI-mass spectrum after ionisation with the XeCl laser. However, this can be neglected because of the mass selective detection at the dopant atom- or cluster masses.

3.2 Droplet Generation

The He_N are produced in the source chamber of the apparatus. The main component is a He closed cycle refrigerator cold head (Leybold RGD1245) attached to a compressor unit (Leybold RW 4000 EU). The helium is expanded through a 5 µm orfice in the nozzle which is linked to the cold head so it can be cooled down to approximately 11 K. Under typical conditions ($T_{nozzle} = 15\,\mathrm{K}$, $p_{He} = 50\,\mathrm{bar}$) the average number of He atoms per droplet is 10^4 which corresponds to a droplet diameter of 10 nm (see also section 2.1).

A skimmer, which is used to lower the radial dispersion of the droplet beam, has a diameter of 300 µm and is located 61 mm downstream from the nozzle [10]. After passing the skimmer the droplet beam enters the pickup chamber where it is interrupted by a chopper wheel. The chopper wheel consists of two open and two closed positions equally distributed around its circumference. With photodiodes the position of the chopper is detected. This chopping setup is used for differential measurements to subtract background influences not originating from the droplet beam.

3.3 Doping the Droplets

During the measurements for this work two evaporation sources were installed in the pickup chamber. One high temperature source was used for Cr, the other resistively heated source was used for the evaporation of Cu.

3.3.1 Cu Evaporation Source

The Cu source is a resistively heated evaporation source with an aluminium oxide (alumina) coated tungsten wire basket with a diameter of 23 mm. It is designed for a maximum power of 768 W [36], however, during this work only approximately 300 W of electrical power were dissipated using a Power Supply (EA-PS 9080-100) with a maximum output power of 3000 W. The alumina crucible is covered with a homemade molybdenum lid which has a 2 mm wide and 20 mm long slit, oriented along the direction of the He_N beam. Figure 3.2 shows a photograph of the crucible and the bottom side of the lid. From this it is evident that the Cu is melted and a lot of material is deposited on the colder lid. To trap the Cu which is not picked up by the He droplets and prevent the emitted radiation from heating the vacuum chamber, the whole crucible is mounted in a water cooled Cu cylinder that provides two rather small holes for the He_N beam to pass through. To reduce the cooling water consumption, both the Cr source and the Cu source share the same cooling water circuit with the cooling shield that separates the cold head from the radiation and oil of the diffusion pump.

In contrast to the Cr source there is no urgent need for a closed loop control in case of the Cu source. It is sufficient for a stable operation of the source to set the desired Cu source heating current (I_{Cu}) on the mains unit and wait until an equilibrium temperature is reached. As the electrical resistivity of the Cu source tungsten wire rises with temperature, the Cu source heating voltage (U_{Cu}) required to force the current through the source rises until an equilibrium temperature is reached. Therefore, the resistance of the source, calculated from U_{Cu} and I_{Cu}, can be used to estimate the Cu source temperature.

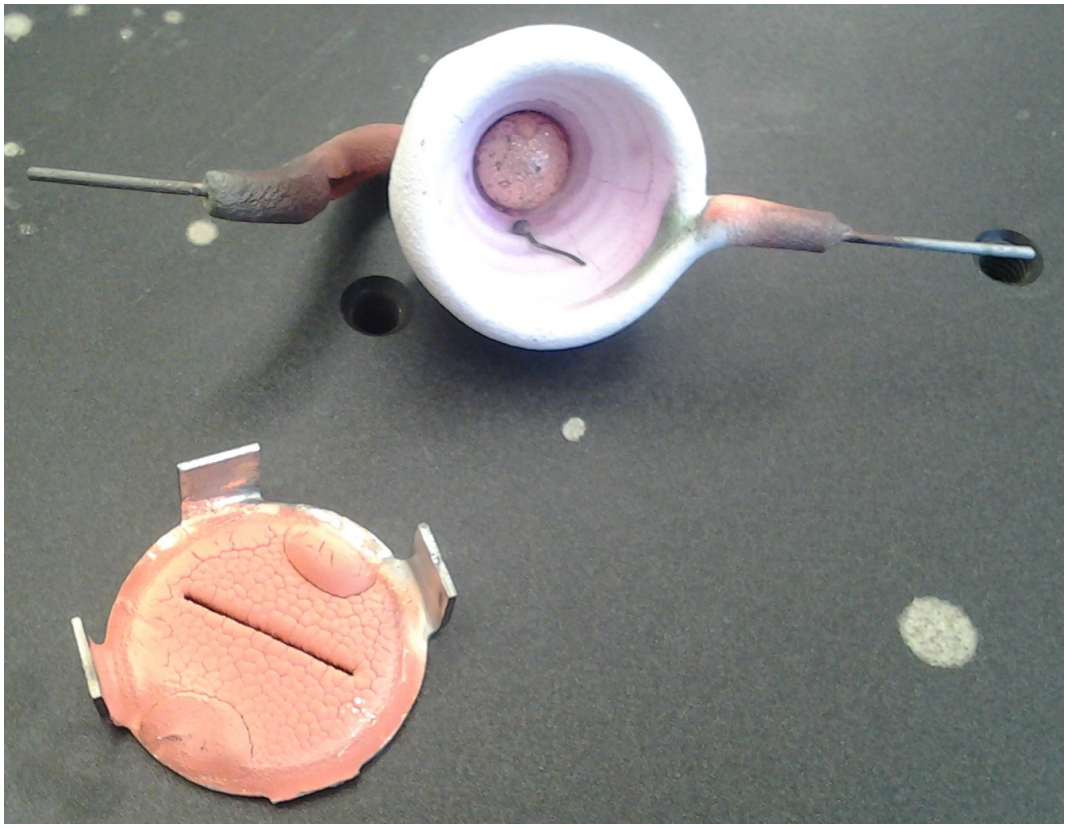

Figure 3.2: Fotograph of the Cu source crucible and the lid.

Once stabilised, the heating power does not change significantly over several hours. The optimum source conditions for the pickup of one or more Cu atoms may although vary slightly on a daily basis, therefore, the cluster pickup maxima should be determined every measurement day. This is accomplished by monitoring the cluster size with the QMS and usually takes ten to 15 minutes. Under usual pickup conditions, the heating current is chosen between 25 and 30 A and the corresponding voltages are seven to eleven volts.

During the first measurements with the Cu source several efforts were made to measure the temperature of the source with a low-cost approach. Two type K thermocouples connected to a data logger (Voltcraft k204) were used for the measurements. The ends of the first couple were positioned inside the crucible in direct contact to the Cu. The end of the second thermocouple was positioned on the lid of the crucible. Unfortunately, several problems occurred during the temperature measurements. Due to thermal expansion the sensor

attached to the lid of the crucible separated from its position, which could be solved by squeezing the the sensor into the gap between the crucible and the lid. Secondly, type K thermocouples are made of the alloys ALUMEL® and CHROMEL® which both have melting points around 1400 °C [37]. This can also be assigned as an estimate for the maximum temperature reached during the measurements, as the thermoelements accidentally melted more than once. A part of a molten thermocouple can be seen in figure 3.2. The biggest problem, which ultimately caused failure of all sensors, is the fact that evaporated Cu is deposited on the wires which leads to the build-up of a second contact point between the two wires, resulting in unusable outputs. Remedy could in principle be achieved by using isolated thermoelements sealed in an isolating material.

The usual operating temperature of the Cu source is approximately 1000 °C. At this temperatures black bodies glow in a light yellowish red. This glow could be observed through the on axis window, usually used for BD experiments. This brought up a problem, as the light was very intense and also irradiated the Laser Induced Fluorescence (LIF) detection system, making fluorescence measurements virtually impossible. To overcome this issue the crucible was lowered to increase the distance between the source and the He_N beam axis. Fortunately, no major decrease in the Cu pickup was observed.

3.3.2 Cr Evaporation Source

The Cr source is described in detail in references [11] and [12], therefore, only a brief description is given here. Electron bombardment is used to heat the Cr evaporation source which has the advantage that high temperatures, sufficient to evaporate Cr ($\approx 1700\,\mathrm{K}$), can be reached and almost no magnetic stray fields are created by high currents. The latter is especially important for magnetic measurements like Magnetic Circular Dichroism (MCD) and Electron Spin Resonance ESR.

The principle of electron bombardment heating is rather simple. Electrons are emitted from hot filaments (extracted from standard 20 W, 12 V halogen

light bulbs) and accelerated towards a tantalum crucible by a high voltage ($U = 1000\,\mathrm{V}$). The Cr filled crucible is heated by the impact of the electrons and Cr atoms effuse through a slit in the lid of the crucible and intersect the $\mathrm{He_N}$ beam some millimetres above the source. Control of the source temperature and thus the rate of Cr pickup is achieved by regulating the electron emission with the filament power. An Eurotherm Proportional Integral Derivative (PID) controller is used to regulate the filament voltage. Control over the PID-controller is granted by LabVIEW programs.

3.4 Lasers

All laser excitations presented in this work were carried out with a pulsed dye laser system. The system consists of a XeCl pump laser, which is also used as ionisation laser in the photoionisation experiments and a tunable dye laser.

3.4.1 Excimer Pump Laser

The pulsed Xenon-Chloride excimer laser (Radiant Dyes RD EXC 200) has a fixed wavelength of 308 nm, a nominal maximum pulse energy of 200 mJ, and a pulse length of $20 - 30\,\mathrm{ns}$ with a maximum repetition rate of 100 Hz. The laser action is achieved by stimulated emission of photons from an electronic transition between a metastable excited state of the XeCl excimers, that are produced in a high-voltage gas discharge, and the unstable ground state. Excimers . The operation gas of the laser is a mixture of Ne (98 vol%), Xe (1.875 vol%), and HCl (0.125 vol%).

3.4.2 Dye Laser

The Lambda Physik FL 3002 tunable dye laser in principle consists of a wavelength selective grating and two dye cuvettes. The first cuvette is used in the Littrow-type oscillator and as a pre-amplifier [38], the second cuvette acts as the main amplifier. During the measurements three laser dyes, DCM, Coumarin 307, and Coumarin 153 were used (properties stated in table 3.1). The output wavelength of the dye laser is scanned by the tilting angle of the grating, controlled with a MATLAB® program via a General Purpose Interface Bus (GPIB) port.

Table 3.1: Laser dye specifications. [39]

Dye	Peak wavelength [nm]	Tuning range [nm]	Efficiency [%]
DCM	640	605 - 698	15
Coumarin 153	544	520 - 602	16
Coumarin 307	500	479 - 555	17

3.4.3 Second Harmonic Generation

Second Harmonic Generation (SHG) is a process in non-linear optics where a lasers frequency is doubled inside a crystal with non-zero second order dielectric susceptibility. The FL3002 offers a crystal tilter stage equipped with a KDP (potassium dihydrogen phosphate) crystal (FL30) and a compensation quartz plate. The crystal allows SHG of fundamental wavelengths between 530 nm and 670 nm resulting in second harmonics between 265 nm and 335 nm. For the measurements presented in this work the longer wavelength part of this range is relevant. By the use of DCM as laser dye, the second harmonic range between 312 nm and 335 nm is accessible. The tilt angle of the crystal is related to the fundamental wavelength by an equation given in reference [38] and controlled with a MATLAB® program (see section A.2.4).

3.5 Detection Methods

In the following sections the detection methods, which were used to collect the data presented in this work, are described.

3.5.1 Quadrupole Mass Spectrometer

The mainly used measuring instrument in this work is the QMS to record mass spectra of the doped droplet beam. The mass spectrometer system is a Balzers QMG 422 and consists of the following parts:

- QMS 422 control unit
- QMA 400 analyser with secondary electron amplifier SEV 217
- QMH 400-5 high frequency generator
- CP 400 ion counter pre-amplifier
- Crossed beam ion source
- IS 420 ion source supply unit
- HV 421 high voltage supply for SEV
- QC 422 quadrupole controller
- AS 420 adapter SIMS

For the purpose of characterising the pickup statistics and BD experiments, the electron impact ion source of the QMS was used. For the PI measurements the pulsed laser was used for ionisation. During the measurements the QMS was mounted in two different ways, on-axis (rod-system in line with He_N beam) and off-axis (90° to He_N beam). The latter orientation provides an access window on the axis of the He_N beam and is therefore used for BD experiments. The on-axis window is also very convenient for the positioning of components along the droplet beam axis, as this is done by looking along the beam path with a telescope. When the QMS is mounted in the on-axis position, it interferes with the telescope view and has to be removed for these adjustments. The on-axis mode is used for PI measurements, as it provides two opposed access windows

which allow to intersect the droplet beam with a laser beam in right angles in the ionisation volume of the QMS.

The QMS system allows the variation of plentiful parameters. Some of the most crucial are the voltages in the ion optics of the crossed beam ion source and the rod system. These voltages are responsible for extraction of the ions from the ionisation volume, focusing and acceleration of the ions. The recommended default values lead to suitable results when the QMS is mounted on-axis and the electron impact ionisation source is used. For the off-axis position and especially for PI, better values for the ion optic voltages were found by my predecessors on this machine. The different sets of voltages are referred to as the **original-**, the **tilted-** and the **photoionisation** values and are stated in table 3.2. If parameters for experiments were chosen to be different from the listed ones, they are stated explicitly.

Table 3.2: QMS ion source operating voltages.

	V_1	V_2	V_3	V_4	V_5	V_6	V_7
original	100	70	15.75	9	300	300	110
tilted	88	70	15	10.5	260	300	110
PI	53	60	11	6.25	350	330	120

Another value of extraordinary importance is the Secondary Electron Multiplier (SEM) voltage U_{SEM}, which sets the gain level. The recommended maximum value is 3.5 kV [40] and the voltages applied during this work range from 2.5 kV to 2.7 kV.

The third important parameter is the QMS filament current (I_{fil}) of the ion source. For most of the measurements that employed the cross beam ion source, a filament current of 0.5 mA was used. During the PI measurements the filament was of course turned off.

3.5.2 Beam Depletion

For BD experiments (section 4.3) a counter-propagating He_N beam and laser setup is used. Therefore, the QMS is mounted in its off-axis position, allowing

to shine the laser through a wedged quartz window anti-parallel to the He droplet beam. This is done to increase the interaction volume compared to a crossed beam setup. When the laser photon energy matches an electronic transition of the dopant, energy is transferred to the dopant-droplet system (see section 2.5). This leads to evaporation of He atoms, the total destruction of the He droplet or the ejection of the dopant from the droplet. Thus the overall flux of He and doped droplets is decreased. By scanning the laser over a certain wavelength range and simultaneously monitoring the He or dopant flux by means of mass spectrometry or other suitable detection methods (for example a Langmuir-Taylor detector), one is able to obtain the pure absorption spectrum of the dopant-droplet system. In the case of the BD spectra presented in section 4.3, the QMS was used to monitor the ion-signal at the mass of the most abundant Cu isotope (63 u), because monitoring the He_2 depletion signal at mass eight showed a poor signal to noise ratio.

The Cu $^2P_{1/2,3/2} \leftarrow {}^2S_{1/2}$ transition which is examined by BD in this work lies at about $310-340$ nm in the near UV region ($300-400$ nm). These wavelengths are only accessible with our dye laser, when doubling the frequency with the use of second harmonic generation (SHG).

The optical setup for the BD experiments is shown in figure 3.3. For the sake of convenience it is drawn linearly where in fact four mirrors are used to guide the beam from the laser in Cluster Lab I (CLI) to the HENDI apparatus in Cluster Lab II (CLII). For the same reason the optical path through the components, for example in the prism (P), is only drawn symbolically. The following components are plotted in the optical setup sketch:

XeCl ... Pulsed XeCl excimer laser (Radiant Dyes RD EXC 200)

Dye laser ... Lambda Physik FL3002

P ... Quartz prism used to split the fundamental beam from the second harmonic.

WM ... Wavemeter (Coherent Wavemaster)

L1 ... Lens ($f = 1500\,\text{mm}$) used to pre-focus the beam. Otherwise it is not possible to direct the beam to the other lab through the hole in the wall.

L2 ... Lens ($f = 2000\,\text{mm}$) used to focus the beam into the apparatus.

QP ... Quartz plate used to decouple a small part of the laser beam for analysis.

PD ... Photodiode for triggering the measurements on the laser pulses.

Spec ... Small USB-Spectrograph (Ocean Optics USB 4000) to analyse the spectral composition of the beam and to detect Amplified Spontaneous Emission (ASE).

DR ... Diffuse reflector (PTFE plate) to provide less intense light for the spectrograph.

QMS ... Quadrupole mass spectrometer.

HENDI ... Helium nanodroplet isolation apparatus.

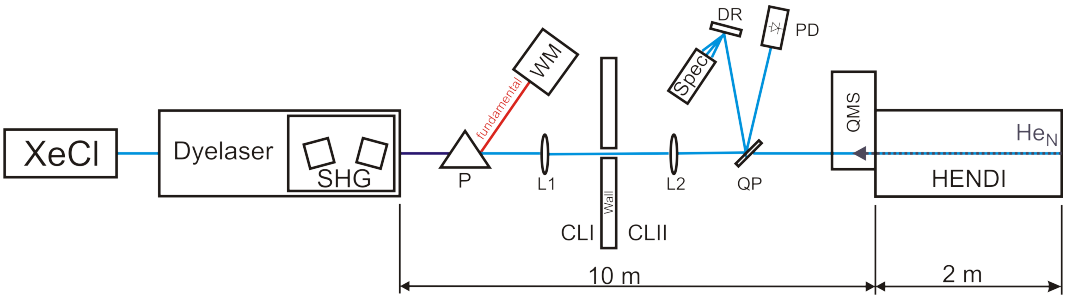

Figure 3.3: Optical setup for beam depletion experiments. (abbrevations explained in the text)

The necessity of SHG to reach the wavelength region of interest turned out to be a problem, as the beam was displaced considerably while scanning the laser wavelength leading to a miss-alignment with respect to the droplet beam. This happened although a compensator plate was installed in the crystal tilting mechanics. The beam displacement is worsened by the long optical path of the laser beam (almost 10 meters). To assure alignment of the laser and the droplet beam the setup had to be readjusted for every wavelength chosen, therefore,

no decent continuous scans were possible. The realignment was accomplished by tilting and linearly displacing one of the mirrors and with this workaround it was possible to record a spectrum in the wavelength region of interest.

The signal acquisition is performed with a two channel counter (Stanford Research SR400) connected to the QMS. The input signal of the SR400 is pre-amplified and discriminated by the QMS. The trigger signal for the counter is provided by the photodiode. The gate of the first channel is set to maximise the depletion signal, therefore, covering the timespan of droplets arriving at the detector influenced by the laser pulse. The gate of the other counting channel is adjusted to count the background ion signal. This means that the trigger-delay time is set long enough to ensure that there is no more influence on the ion counts from the laser pulse. The counting gates are visualized in figure 4.13 (section 4.3). The depletion signal is calculated by subtracting the count rates of the two channels.

3.5.3 Laser Induced Fluorescence

Beforehand, during the measurements for this work no LIF signal from Cu doped helium nanodroplets could be detected. It is not clear if this happened due to errors during the measurement or because of physical reasons, so only a brief description of the experimental setup is given here.

Laser induced fluorescence measurements were performed using a crossed beam arrangement where the He_N beam is perpendicularly intersected by the excitation laser (otherwise similar setup as in section 3.5.2). The interaction volume is located within a collimating mirror and a condenser lens oriented perpendicular to both the laser and the droplet beam. The emitted fluorescent light is reflected upwards where it is collected and guided by a system of lenses and focussed onto the active layer of a photomultiplier tube (EMI 9863QB/360). It should be mentioned that the condenser lens of this optical setup is made of B270 which, according to the manufacturer [41], is transparent from 320 nm to 2600 nm. The wavelengths of interest extend to the very edge of this range, where a large portion of the intensity is absorbed by the material. Therefore

only fluorescence in the visible wavelength region is well detectable. Like in the BD experiments, a fast photodiode is used to generate a trigger signal from the incoming laser pulses. The PMT signal and the trigger signal are fed to a counter (Stanford Research SR400) to perform gated single photon counting, or to a boxcar averager and gated integrator (Stanford Research SR250) for analogue signal acquisition. The objective is to measure an integral LIF spectrum by scanning the laser wavelength over the same interval as in the BD experiments and record the non-dispersed fluorescent light intensity.

At the beginning of the measurements with the Cu evaporation source a problem occurred, as the glowing crucible was mounted very close to the droplet beam axis and therefore shined light into the LIF detection volume (see section 3.3). The photon flux from the glowing source exceeded the PMT specifications which made LIF measurements impossible. Small changes in the source adjustment made it possible to mount the crucible in a lower position and to reduce this problem.

3.5.4 Photoionisation

In the PI experiments a laser is used to ionise the species doped to the He droplets. This happens in the ionisation region of the QMS, where usually electrons emitted by a filament ionise the atoms or molecules. As the ionisation energies of bare atoms and small clusters are usually of the magnitude of several eV, two photon processes are required to ionise the dopant when using visible or near UV laser radiation. The two absorbed photons can either be of the same or different energies. In the present work almost exclusively two Colour Resonant two Photon Ionisation (2CR2PI) schemes were applied. One photon is provided by the second harmonic of the tune-able dye laser (FL3002) and the other one originates from the XeCl pump laser. Therefore, a small part of the pump beam is uncoupled inside the dye laser. Both laser beams are then guided, focussed, and intersected inside the ionisation region of the QMS. A sketch of the optical setup can be found in figure 3.4.

Additionally to the parts described in section 3.5.2 the following short terms

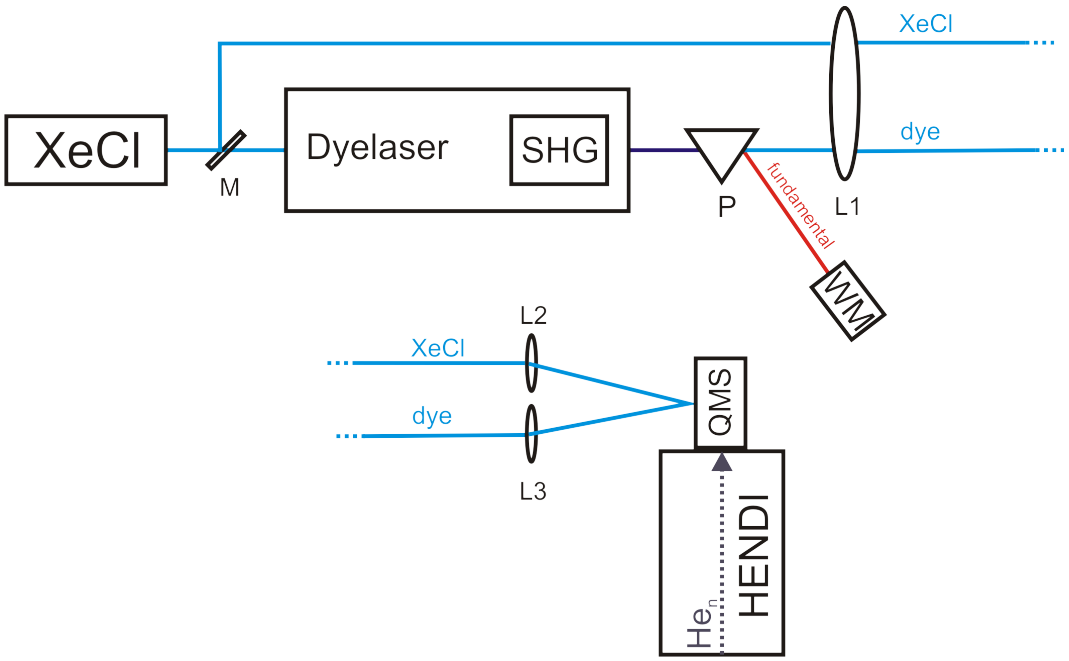

Figure 3.4: Optical setup for photoionisation experiments. (abbrevations explained in text)

are used in the optical setup sketch:

M . . . Mirror used to decouple a fraction of the XeCl laser beam.

L2 . . . Lens ($f = 750\,\mathrm{mm}$) used to focus the XeCl-laser beam into the ionisation region.

L3 . . . Lens ($f = 1000\,\mathrm{mm}$) used to focus the dye laser beam into the ionisation region.

The detection system for PI measurements is similar to that in BD experiments. The pre-amplified and discriminated output signal from the QMS is fed to the SR400 counter. The only difference is, that no trigger signal is necessary as there are no ions produced in between the laser pulses. For the PI measurements the chopper is turned off to maximise the photo ion signal because the element specific excitation with the laser renders it unnecessary to take a background signal.

For 2CR2PI the spatial adjustment of the two lasers is crucial, as perfect overlap

of the laser beams at the ion extraction position inside the QMS ionisation region has to be ensured. The best point for overlapping the beams is first found by trial and error and then improved by systematic alternation of both beam positions. Along with the location of the lasers in the ionisation region, also the focusing of the two lasers has a huge impact on the ion yield, as the area of the beam directly influences the laser power density.

The ionisation chamber of the QMS is equipped with one wedged and one planar quartz window. The laser beams enter the chamber through the wedged window and exit through the plain one where they undergo further analysis. A laser power meter (Coherent Field Max II, measurement head J-50MUV-193) was used to measure the SHG pulse energy during the measurements.

The second window also allows to put a screen directly behind the ionisation volume which can be very helpful for the beam adjustment. As stated above, the overlap of the two lasers is very important. Unfortunately the SHG crystal caused serious beam displacement when the wavelength was scanned, therefore, the SHG beam position had to be tracked manually. This was accomplished by first optimizing the signal at a fixed wavelength, marking the spot of the laser on the screen behind the ionisation volume and manually correcting the shift of the beam during the scan.

4 Results

The following chapter contains the conclusions drawn from the data collected during the work for this thesis. The first part deals with the characterisation of the Cu source. In the next step the observation of mixed CrCu clusters is considered and finally optical spectra of Cu doped helium nanodroplets are presented.

4.1 Characterisation of the Cu Source

In this section characterisation measurements of the Cu source, which is described in detail in section 3.3, are presented. These measurements feature the source temperature dependency on the heating power dissipated by the system, a closer look on the Cu pickup statistics and a mass spectrometric study of the Cu doped helium nanodroplets.

4.1.1 Heating Characteristics

First tests of the Cu source were carried out in absence of the He_N beam. In these experiments the temperature of the evaporation crucible was determined as a function of the heating current which was manually adjusted on the mains unit. The temperature of the Cu was measured five minutes after setting the heating current. The dependence of the source temperature on the heating current and the heating power is illustrated in figure 4.1. As indicated by the

linear fits in figure 4.1b, the source temperature shows nearly linear dependence on the heating power. Every plot shows two lines representing the two Type-K thermocouples that were installed in the source chamber. One was located directly in the melting crucible, the other one was meant to be in contact with the molybdenum cover of the crucible, but turned out to have detached during heat-up resulting in a temperature drop above 60 W heating power. The non-linearity of the curves in figure 4.1a can be attributed to the fact that the dissipated power rises like the square of the current and that the resistance of the source crucible rises with temperature.

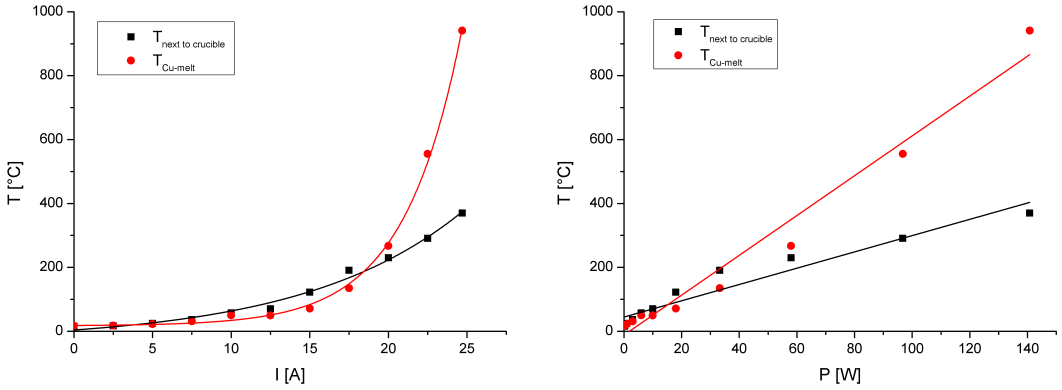

(a) Dependence of source temperature on heating current. (solid lines are exponential fits.)

(b) Dependence of source temperature on heating power. (solid lines are linear fits.)

Figure 4.1: Cu source heating characteristics.

The temperature dependence of the electric resistance can be expressed in terms of

$$R = R_0 \left[1 + \alpha \left(T - T_0\right)\right] \tag{4.1}$$

which can be rearranged to

$$T = T_0 + \frac{1}{\alpha}\left[\frac{R}{R_0} - 1\right] \tag{4.2}$$

Using Ohm's law $U = RI$ this equation can be fitted to the data presented in figure 4.1 and the following values are obtained (T_0 is fixed at room temperature):

$$T_0 = 300\,\mathrm{K}, \qquad \alpha = 4 \pm 1 \cdot 10^{-3}\,\mathrm{K}^{-1}, \qquad R_0 = 5.8 \pm 0.1 \cdot 10^{-2}\,\Omega \tag{4.3}$$

Assuming the resistance of the Cu source only originates from the tungsten wire basket, the specific resistance can be estimated from R_0 by $\rho = R_0 A/l$ including the cross-section area ($A = 1.2\,\mathrm{mm}^2$) and the length ($l \approx 0.7\,\mathrm{m}$) of the tungsten wire. This leads to a specific resistance of $\rho = 9.6 \cdot 10^{-8}\,\Omega\mathrm{m}$. Both the specific resistance (ρ) and the temperature coefficient (α) are in acceptable agreement with literature values [13]. Equation 4.2 and coefficients 4.3 can be used to estimate the temperature from I_{Cu} and U_{Cu}.

Unfortunately the relatively low melting point of the Type-K thermocouples (about 1400°C) turned out to be a problem, as the sensors melted and had to be replaced. Thus, the temperatures stated in this section are not directly comparable to the ones in the following parts of this thesis.

4.1.2 Doping Characteristics

In this section the process of doping the He_N beam with one or more Cu atoms per droplet is analysed by means of mass spectrometric methods. All presented spectra were obtained by electron impact ionisation of the seeded droplets and ion detection with the quadrupole mass spectrometer.

A mass spectrum of the Cu doped droplet beam is shown in figure 4.2. It clearly shows the occurrence of small Cu clusters (Cu_n) from n=2 to n=7. Detection of bigger clusters is limited by the mass range of the QMS with a maximum mass to charge ratio of $500\,\mathrm{u/e}$. The insert in figure 4.2 shows an enlarged plot of the Cu_7^+-peaks. Due to the two stable Cu isotopes (^{63}Cu and ^{65}Cu) there is not a single Cu_7^+ cluster peak but a series of peaks for all permutations spanning from $m = 441\,\mathrm{u}$ ($^{63}Cu_7^+$) up to $m = 455\,\mathrm{u}$ ($^{65}Cu_7^+$). The peak at 455 u is not plotted in the insert as it is predominated by background signal. The red bars represent the calculated isotopic pattern of the Cu_5 mass spectrum which was calculated using the SIS isotope distribution calculator [42] and is in good agreement with the measured mass spectrum. Along with the seven peak complexes corresponding to the Cu clusters, several other accumulations of peaks are visible in figure 4.2. These features can be assigned to complexes of Cu clusters and one, two or three water molecules and their fragments attached. In order

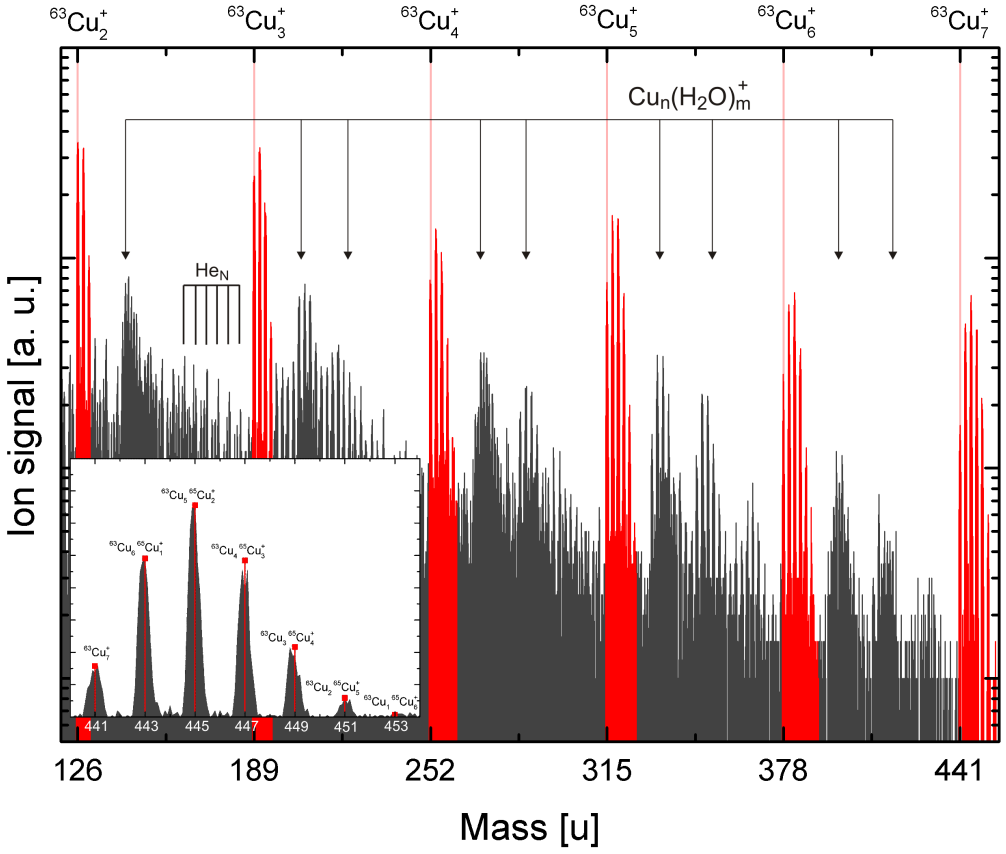

Figure 4.2: Mass spectrum of Cu doped He_N. (Cu source: $I_{Cu} = 26.6\,\mathrm{A}$, $U_{Cu} = 8.73\,\mathrm{V}$; Coldhead: $T_{nozzle} = 13.5\,\mathrm{K}$; QMS: $I_{Fil} = 0.25\,\mathrm{mA}$, $U_{SEV} = 2700\,\mathrm{V}$, tilted voltages)

to decrease the amount of water incorporated into the He_N the cryotraps in the pickup- and measurement chamber were filled with liquid nitrogen. The use of the cold traps had a measurable effect on the pressure in the vacuum chambers which dropped in the measurement chamber from $2.9 \cdot 10^{-7}\,\mathrm{mbar}$ to $1.8 \cdot 10^{-7}\,\mathrm{mbar}$ and decreased in the pickup chamber from $1.5 \cdot 10^{-6}\,\mathrm{mbar}$ to $1.4 \cdot 10^{-6}\,\mathrm{mbar}$. About 40 minutes elapsed until these equilibrium pressures were reached.

While the use of the cold traps had only little impact on the number of detected Cu-water complexes it led to a significant improvement of the pure Cu_n^+ signal. Figure 4.3 shows a comparison of the Cu-cluster ion signal with filled and empty cold traps. The data in this figure represents the sum over all isotopic

compositions of the different cluster sizes. The blue line in figure 4.3 corresponds to the intensities extracted from the mass spectrum plotted in figure 4.2 which was recorded with the cold traps in use. The black and red data points are calculated from two mass spectra recorded without liquid nitrogen cold traps. The blue and the red curve originate from two subsequent mass scans. By comparing them it is evident that the signal is enhanced by approximately 35% (average over all Cu-cluster sizes) with the use of the cryo traps.

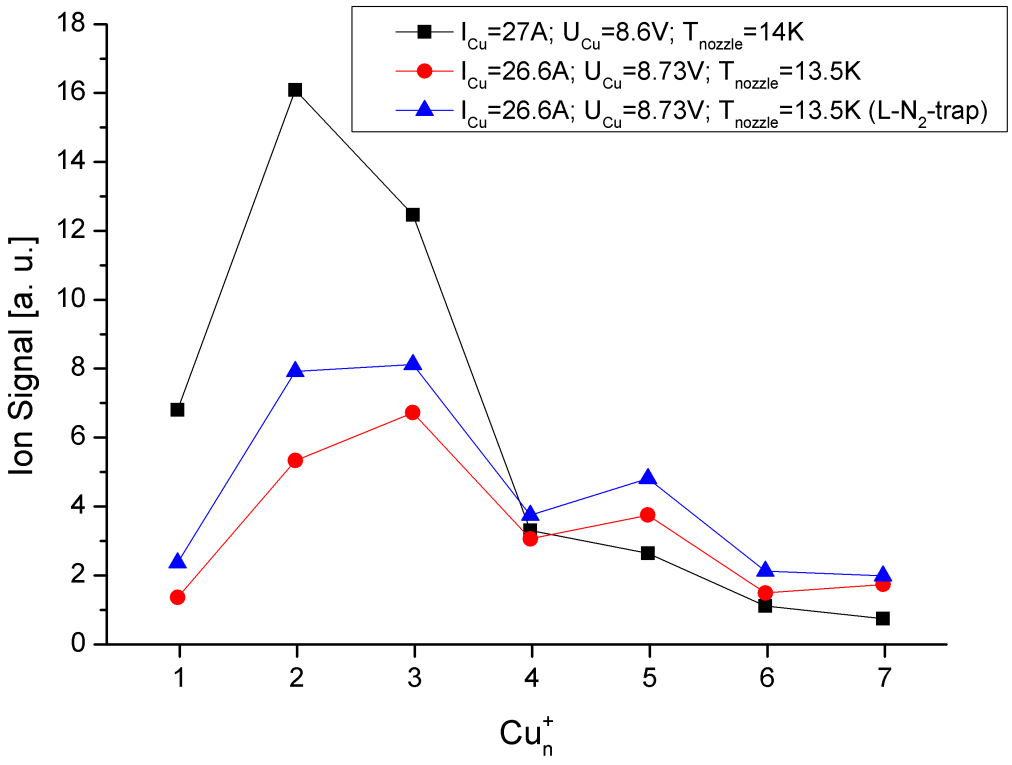

Figure 4.3: Comparison of Cu-cluster detection for filled and empty cold traps. (QMS: $I_{Fil} = 0.25\,\mathrm{mA}$, $U_{SEV} = 2700\,\mathrm{V}$, original voltages for red and blue curve, tilted voltages for black curve)

It has to be noted, that the mass spectrum for the black curve in figure 4.3 was recorded at a nozzle temperature of 14 K and using the QMS in the tilted configuration while the other spectra shown in this figure were produced at a nozzle temperature of 13.5 K with an on-axis QMS assembly. The differences between the two QMS setups are described in chapter 3. Therefore these data sets should only be compared in a qualitative manner. Regardless of these experimental differences the results in figure 4.3 clearly show that in the case of

the latter experiments (blue and red lines) more of the bigger clusters ($n > 4$) are detected and an odd-even oscillation appears where odd cluster sizes are favourably detected. These oscillations are in agreement with the odd-even oscillations of the ionisation potential of small Cu clusters, as even numbered clusters tend to have higher ionisation potentials [43]. Odd-even oscillations in the binding energies would be another explanation for this behaviour, although, according to reference [44] no such oscillations are expected in the case of Cu_n clusters.

In the next step the signal for different cluster sizes is analysed with respect to the temperature of the Cu source and the nozzle. As described in more detail in the experimental section (chapter 3), several difficulties occurred with the evaporation source temperature measurement system. For this reason, the following source temperature values lack accuracy and comparability, and are therefore referred to as "approximate temperatures". In figure 4.4 the ion signals for several small Cu clusters are related to the nozzle and the Cu source temperature. In addition to the Cu cluster signals the signal of He_2^+ at mass eight is shown. This signal is a good indicator for the total number and size of He_N reaching the detector.

The heat-up curves in figure 4.4 were measured by setting a fixed heating current of 30 A at the power supply. Starting from a source temperature of about 700°C this led to a rather fast increase in temperature. During this heating process the temperature of the crucible as well as the ion signals of the Cu clusters and the helium dimer were recorded with a LabVIEW program capable of tuning the mass detection window of the QMS to different values.

For low cold-head temperatures and accordingly big He_N, the heat-up curves for Cu clusters of sizes with up to six atoms could be recorded (note the logarithmic scale in figure 4.4). All pick-up curves show distinct maxima and it is clearly visible that the maxima move towards higher source temperatures for bigger Cu clusters. This property can be used to influence the cluster size distribution. The maxima for the different cluster sizes and temperatures, listed in table 4.1, where obtained by gaussian fits of the data from figure 4.4. As the data for different measurement cycles and cold-head temperatures is not comparable

due to the thermo couple uncertainties, only numbers in the same row shall be compared. By doing so, one can deduce that the maxima move to higher temperatures for cluster sizes from $n = 1$ to $n = 3$, but stay rather constant for the pickup of more Cu atoms. Although the temperature measurements were carried out with a rather cheap system the temperature range for doping the droplets with Cu atoms is in coarse agreement with literature values [3] and a lack of comparability can also be attributed to the unknown geometrical lay-out of the evaporation source in reference [3].

Table 4.1: Cu source temperatures in degree celsius at the signal maxima for several Cu cluster sizes. (T_{noz}...nozzle temperature, $T_{\mathrm{Cu_n^+}}$...temperature corresponding to maximum $\mathrm{Cu_n}$ pickup, $T_{\mathrm{He_2^+}}$...temperature corresponding to maximum $\mathrm{He_2^+}$ signal)

T_{noz} [K]	$T_{\mathrm{Cu^+}}$ [°C]	$T_{\mathrm{Cu_2^+}}$ [°C]	$T_{\mathrm{Cu_3^+}}$ [°C]	$T_{\mathrm{Cu_4^+}}$ [°C]	$T_{\mathrm{Cu_5^+}}$ [°C]	$T_{\mathrm{Cu_6^+}}$ [°C]	$T_{\mathrm{He_2^+}}$ [°C]
14	1004	1020	1027	1025	1026	1016	977
15	984	1000	1009	1009	1017	-	928
16	992	1017	1024	1019	1007	-	924
17	1022	1042	1050	-	-	-	948
18	1006	1027	1037	-	-	-	921

With the impact of dopant atoms on the $\mathrm{He_N}$ in the evaporation source interaction region, energy is transferred to the droplets. By evaporative cooling of He from the droplets surface this energy is removed but leads to shrinkage or, in the extreme case, destruction of the droplets. This explains the steep decrease in $\mathrm{He_2^+}$-signal at higher source temperatures where more Cu is incorporated to the $\mathrm{He_N}$ due to the higher vapour pressure in the pickup region. It is an interesting feature that the $\mathrm{He_2^+}$-signal also shows a clear maximum, which lies at a lower temperature than the Cu-pickup-maximum for all chosen cold-head temperatures. The maximum may be attributed to the fragmentation of big $\mathrm{He_N}$ and a high overall flux of droplets reaching the detector. This assumption is supported by the fact that the maximum in the $\mathrm{He_2^+}$-signal is more distinctive in the case of low cold-head temperatures, thus a droplet beam containing more big droplets.

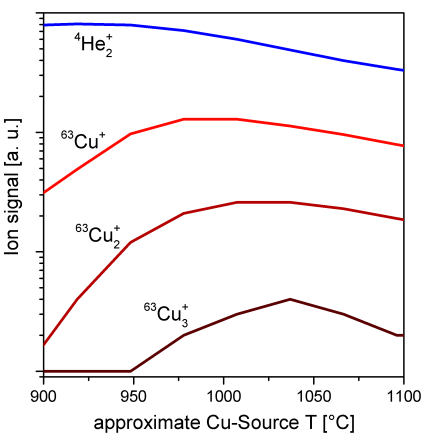

(a) $T_{nozzle} = 18\,\mathrm{K}$

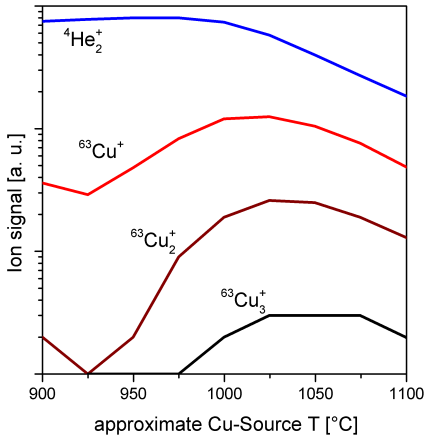

(b) $T_{nozzle} = 17\,\mathrm{K}$

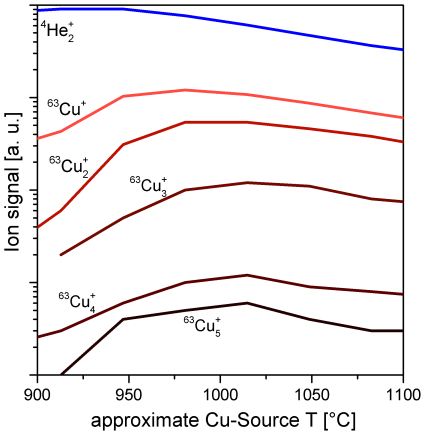

(c) $T_{nozzle} = 16\,\mathrm{K}$

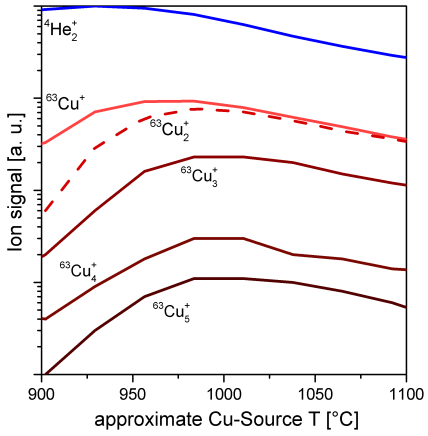

(d) $T_{nozzle} = 15\,\mathrm{K}$

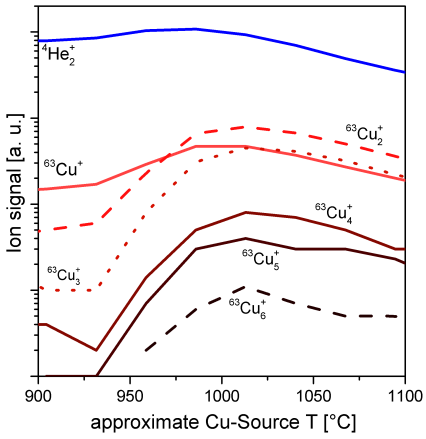

(e) $T_{nozzle} = 14\,\mathrm{K}$

Figure 4.4: Cu source heat-up curves for different nozzle temperatures.

4.2 Mixed CrCu Clusters

During the measurements for this master thesis two evaporation sources were mounted in the vacuum vessel, one resistively heated source used for evaporating Cu and a high temperature electron bombardment source for the evaporation of Cr [12]. On the following pages results from mass spectrometric experiments are presented, showing the successful doping of mixed high melting transition metal clusters to He_N.

4.2.1 Mass Spectrum of CrCu Doped Helium Droplets

First the mass spectrum of the droplet beam doped with both metals at moderate rates is analysed for the Cu and Cr mixed cluster system. Figure 4.5 shows two mass spectra that were recorded at different operation states of the evaporation sources. For a better visibility of the features of interest a mass spectrum of the unseeded helium beam was subtracted from both spectra. The red plot originates from a measurement where both sources were operating, the blue one was recorded with solely the Cr-source switched on. All other experimental values were equal for both spectra. By comparing both spectra it is possible to assign several peaks to CrCu complexes. CrCu, Cr_2Cu, and $CrCu_2$ are clearly visible, bigger mixed clusters were not observed in the intense noise originating from a large number of detected Cu-water and Cr-water complexes. The peaks for Cr in combination with one water molecule and its fragments, and even the peaks for the combination of Cr and two water molecules, have twice the intensity of the Cr dimer peak (blue data in figure 4.5). Nevertheless, figure 4.5 clearly verifies, that mixed CrCu clusters are formed inside the He_N.

Some interesting aspects are not clearly visible in figure 4.5 due to the overlap of the spectra. Therefore a differential spectrum is plotted in figure 4.6. In this differential mass spectrum the features belonging solely to Cr and those attributed to CrCu-clusters are better separated than in figure 4.5. The species responsible for positive peaks in figure 4.6 are more abundant in the CrCu doped beam while negative peaks indicate the opposite. Along with the clusters

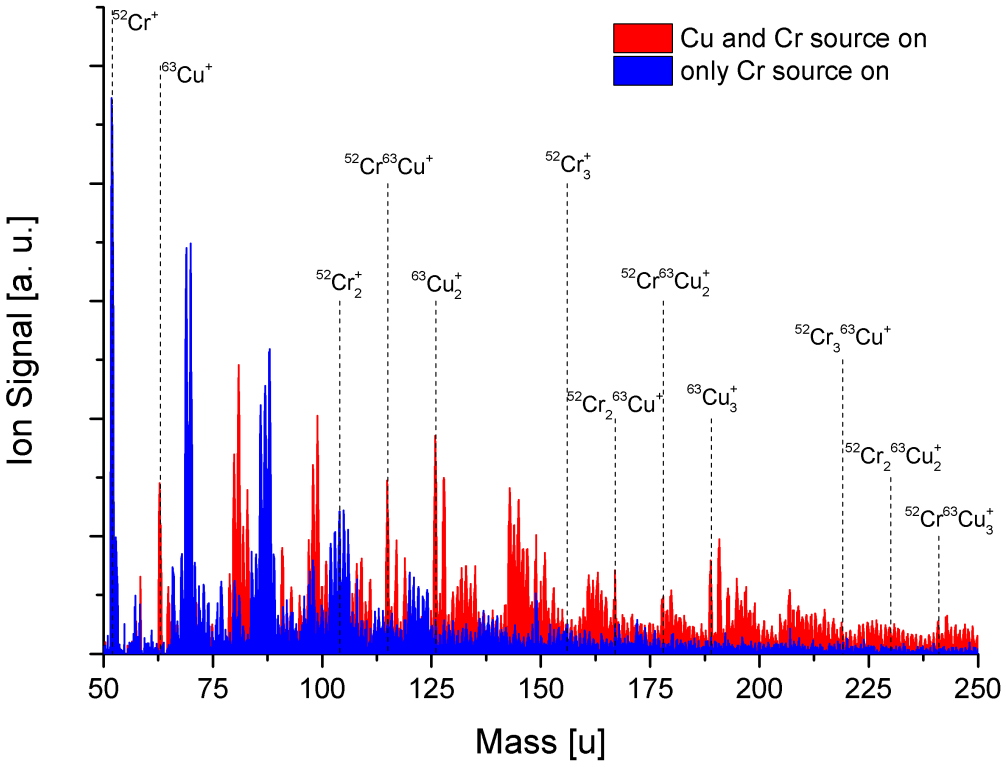

Figure 4.5: Mass spectrum of the Cu and Cr doped He_N beam. (Cu source: $I_{Cu} = 25.3\,A$, $U_{Cu} = 7.9\,V$; Cr source: $P_{Cr} = 120\,W$; Coldhead: $T_{nozzle} = 14\,K$; QMS: $I_{Fil} = 0.5\,mA$, $U_{SEV} = 2700\,V$, original voltages)

containing two or three atoms also two peaks at 241 u and 243 u are visible, consistent with the most abundant isotopic mixtures of $CrCu_3$. The most prominent negative features originate from Cr, Cr_2, and Cr-water complexes. The presence of these negative peaks in the difference spectrum shows that the additional doping with Cu atoms lowers the number of detected Cr atoms and dimers. Most probably this happens because of the destruction of additional droplets due to the second active evaporation source as well as the consumption of Cr for CrCu clusters. This explanation is supported by the fact that negative He_n-peaks appear in the spectrum, indicating that the total flux of droplets is lowered by the additional operation of the Cu evaporative source. The inset of figure 4.6 shows the isotopic pattern of the CrCu peaks, including the calculated isotopic composition (red bars) [42]. The measured peaks at 115 u and 117 u are in good agreement with the calculated values. The peak at 119 u can be assigned to $^{52}Cr^{63}CuHe^+$, as the appearance of dopant-helium complexes in

mass spectra of doped He_N is very common [11].

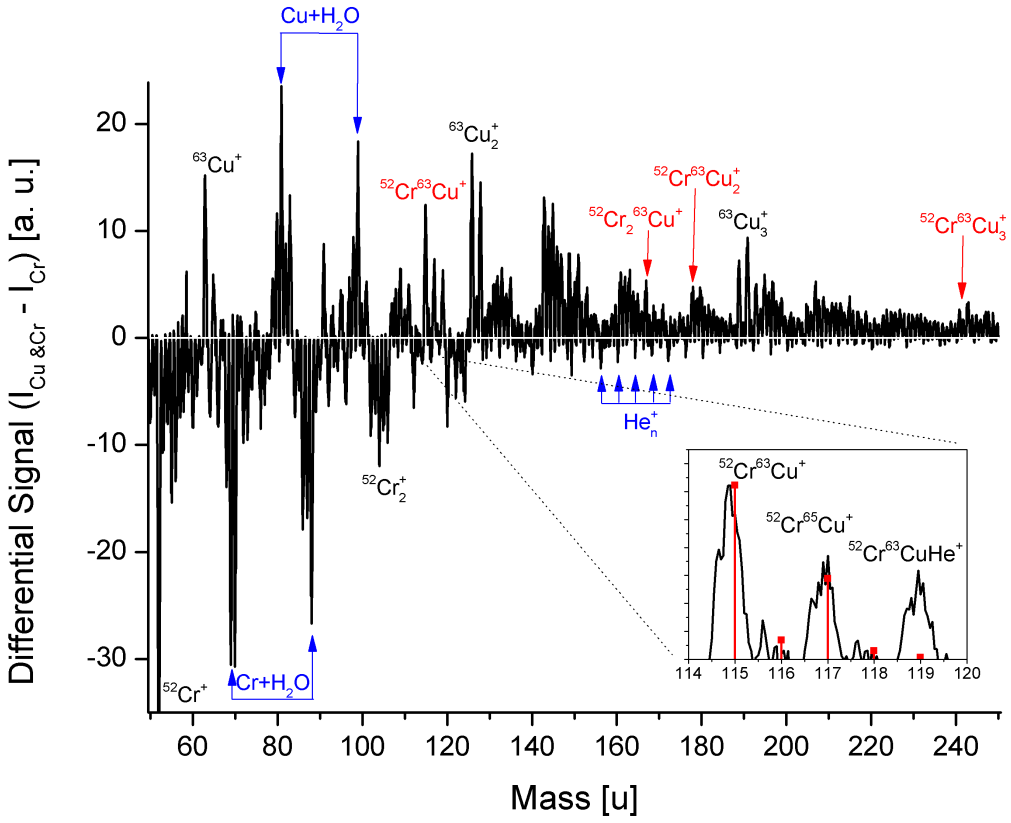

Figure 4.6: Differential signal of the spectra in figure 4.5 (Both sources active minus only Cr source active. Experimental conditions stated in the caption of figure 4.5)

4.2.2 Characterisation of the CrCu Pickup

The next step was to find the optimum experimental values for doping He_N with mixed CrCu clusters. Therefore the three parameters, P_{Cr} (Cr source heating power), I_{Cu} (Cu source heating current), and T_{nozzle} (nozzle temperature) were systematically altered and the corresponding ion signals at the significant masses were recorded.

The considered masses are:

- $^{4}\mathrm{He}_2$ ... $m_{\mathrm{He}_2} = 8\,\mathrm{u}$
- $^{52}\mathrm{Cr}$ ... $m_{\mathrm{Cr}} = 52\,\mathrm{u}$
- $^{63}\mathrm{Cu}$ ... $m_{\mathrm{Cu}} = 63\,\mathrm{u}$
- $^{52}\mathrm{Cr}^{63}\mathrm{Cu}$ ... $m_{\mathrm{CrCu}} = 115\,\mathrm{u}$
- $^{52}\mathrm{Cr}_2^{63}\mathrm{Cu}$ ... $m_{\mathrm{Cr}_2\mathrm{Cu}} = 167\,\mathrm{u}$
- $^{52}\mathrm{Cr}^{63}\mathrm{Cu}_2$ ... $m_{\mathrm{CrCu}_2} = 178\,\mathrm{u}$

By collecting the data one is able to create a map of the configuration space and to find the optimal parameters for the CrCu pickup. In this section several cuts through the three dimensional space of settings are presented, starting with the ion signal corresponding to CrCu^+ (figure 4.7). The three subplots show the dependence of the ion signal on the Cr source heating power and the nozzle temperature for three different Cu source heating currents. The scales are fixed for all three plots, therefore the maximum ion signal can be spotted as the dark red triangle at the top of figure 4.7b. The conditions for the maximum observed CrCu pickup therefore are:

$$I_{Cu} = 25.3\,\mathrm{A}, \qquad P_{Cr} = 150\,\mathrm{W}, \qquad T_{nozzle} = 14\,\mathrm{K} \tag{4.4}$$

From figure 4.7 it is also evident that the region where CrCu is detected extends to higher nozzle temperatures for higher values of the Cu source heating current. This might be attributed to the higher number density of Cu atoms in the pickup cell which raises the probability of the pickup of an Cu atom in the smaller droplets produced at higher nozzle temperatures. Another feature is the steep slope towards low nozzle temperatures (about $\sim 13\,\mathrm{K}$) where the number of droplets is significantly lower.

Along with the maximum CrCu signal it is also of interest to find the best pickup conditions for a high ratio of CrCu to atomic Cu and Cr, which is especially useful if the considered species have overlapping optical spectra. For analysis, the ratio of the signals $\frac{I_{CrCu}}{I_{Cu}+I_{Cr}}$ is plotted in figure 4.8. Compared to figure 4.7, the maximum is shifted towards lower heating powers for both sources and lower nozzle temperatures. The maximum of the $\frac{I_{CrCu}}{I_{Cu}+I_{Cr}}$-ratio is

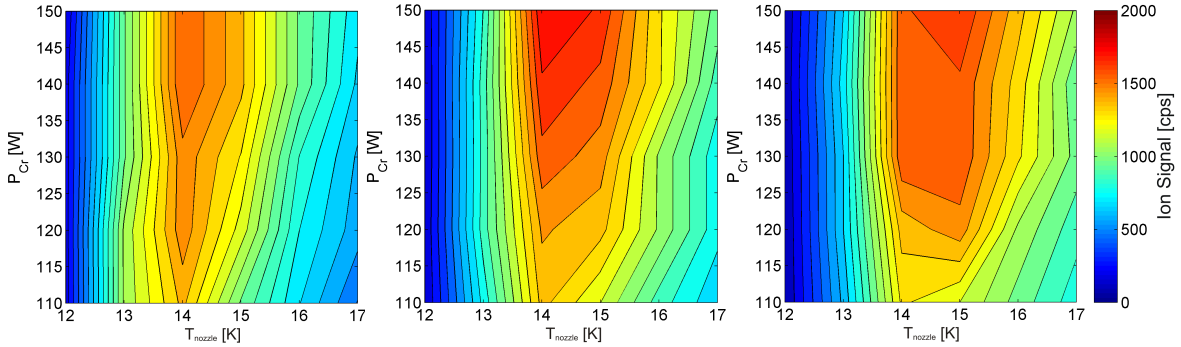

(a) $I_{Cu} = 24.5\,\mathrm{A}$ (b) $I_{Cu} = 25.3\,\mathrm{A}$ (c) $I_{Cu} = 25.8\,\mathrm{A}$

Figure 4.7: Ion signal of the $CrCu^+$ molecule for different nozzle temperatures, Cr heating powers, and Cu heating currents. (colour map applies to all plots)

characterised by the following values:

$$I_{Cu} = 24.5\,\mathrm{A}, \qquad P_{Cr} = 110\,\mathrm{W}, \qquad T_{nozzle} = 13\,\mathrm{K} \tag{4.5}$$

The ratio at this point is 0.38, so the signal from CrCu is almost 40% of the sum of the Cu and the Cr signal. This may sound a lot but one has to consider that the overall CrCu signal at this point is 60% lower than with conditions specified by the parameters 4.4. According to the experimental requirements either the settings specified with parameters 4.4 or the ones with parameters 4.5 are to be chosen.

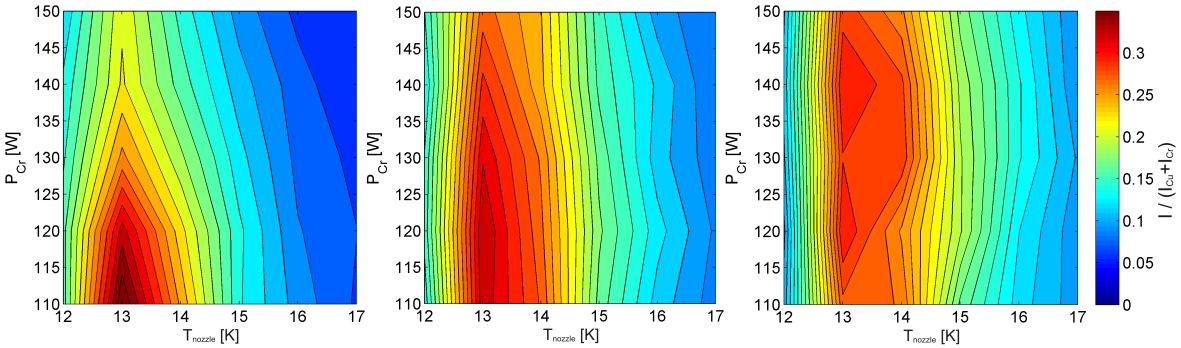

(a) $I_{Cu} = 24.5\,\mathrm{A}$ (b) $I_{Cu} = 25.3\,\mathrm{A}$ (c) $I_{Cu} = 25.8\,\mathrm{A}$

Figure 4.8: Ion yield ratio $\frac{I_{CrCu}}{I_{Cu}+I_{Cr}}$ for different Cu source heating currents. (colour map applies to all plots)

As stated at the beginning of this section, the same data as for the CrCu molecule was also recorded for the two possible mixed trimers. For the Cr_2Cu molecule the results are presented in figure 4.9 and the ones for $CrCu_2$ in figure 4.10.

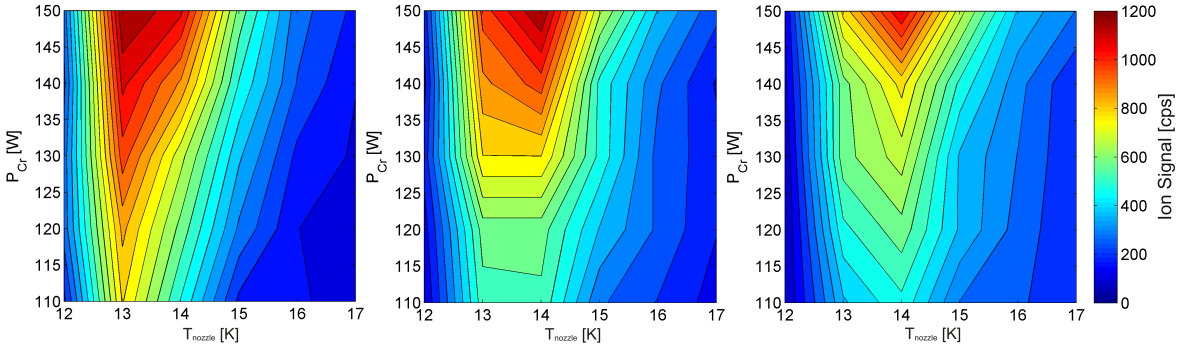

(a) $I_{Cu} = 24.5\,\mathrm{A}$ (b) $I_{Cu} = 25.3\,\mathrm{A}$ (c) $I_{Cu} = 25.8\,\mathrm{A}$

Figure 4.9: Ion signal of the Cr_2Cu^+ molecule for different nozzle temperatures, Cr heating powers, and Cu heating currents. (colour map applies to all plots)

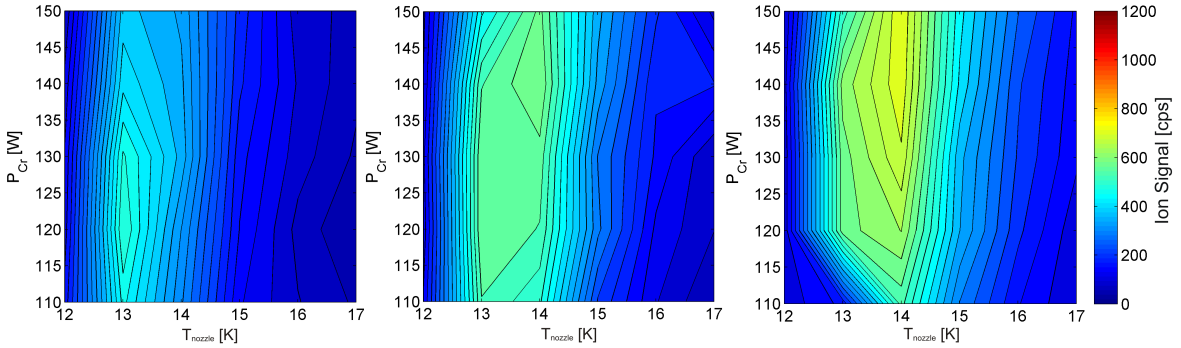

(a) $I_{Cu} = 24.5\,\mathrm{A}$ (b) $I_{Cu} = 25.3\,\mathrm{A}$ (c) $I_{Cu} = 25.8\,\mathrm{A}$

Figure 4.10: Ion signal of the $CrCu_2^+$ molecule for different nozzle temperatures, Cr heating powers, and Cu heating currents. (colour map applies to all plots)

The optimum values for the pickup of Cr_nCu_m clusters are stated in table 4.2. By comparing the ion signal n in table 4.2 it is evident that fewer three atomic molecules than dimers are formed, beyond that the formation of $CrCu_2$ is less favourable than that of Cr_2Cu.

Table 4.2: Optimum pickup conditions for Cr_nCu_m clusters. (T_{nozzle}...nozzle temperature ($\Delta T_{nozzle} = \pm 0.5\,\mathrm{K}$), I_{Cu}...Cu source heating current ($\Delta I_{Cu} = \pm 0.4\,\mathrm{A}$), P_{Cr}...Cr source heating power ($\Delta P_{Cr} = \pm 5\,\mathrm{W}$, n...ion signal ($\Delta n = \pm 200\,\mathrm{cps}$), r...ratio $\frac{Cr_mCu_n}{Cu+Cr}$ ($\Delta r = \pm 0.05$).

	$CrCu$	$\frac{CrCu}{Cu+Cr}$	Cr_2Cu	$\frac{Cr_2Cu}{Cu+Cr}$	$CrCu_2$	$\frac{CrCu2}{Cu+Cr}$
T_{nozzle} [K]	14	13	13	13	14	13
P_{Cr} [W]	150	110	150	150	150	120
I_{Cu} [A]	25.3	24.5	24.5	25.8	25.8	25.8
n [cps]	1800	-	1200	-	740	-
r	-	0.38	-	0.33	-	0.26

4.3 Beam Depletion

In this section the results of the experiments employing the Beam Depletion (BD) technique (see section 3.5.2) are presented. BD experiments were carried out for two species, Cu and Cu_2. The spectrum in figure 4.11 shows the depletion signal for ^{63}Cu, the most abundant Cu isotope. Because of the difficult experimental circumstances a stepwise recording of the beam depletion signal was performed and is referred to as manual scan. Along with the results of the manual scan, the positions of the $^2P_{1/2,3/2} \leftarrow {}^2S_{1/2}$ free atom transitions [21] are marked in the spectrum. A comparison shows a blue-shift of $200\,\mathrm{cm}^{-1}$ and broadening of $500\,\mathrm{cm}^{-1}$ with respect to the free atom transition energies.

Under the experimental circumstances, which are stated in the caption of figure 4.11, a total Cu ion signal of 3500 counts per second was measured throughout the data collection. This means the maximum depletion signal had a relative magnitude of 4%. The data points plotted in the BD spectrum correspond to the mean values of the ion signal over a period of 20 seconds. The error bars represent the standard errors of the datasets. For better visibility a smoothed line, calculated with a simple adjacent-averaging method, is also shown.

During the manual scan (figure 4.11) the pulse energy of the excitation laser was measured with a Coherent Field Max II laser powermeter. With this additional information it is possible to perform a laser power correction, although this correction does not affect the main features of the spectrum in a significant way. Only a slight increase of the high energy flank of the peak occurs (figure 4.12a).

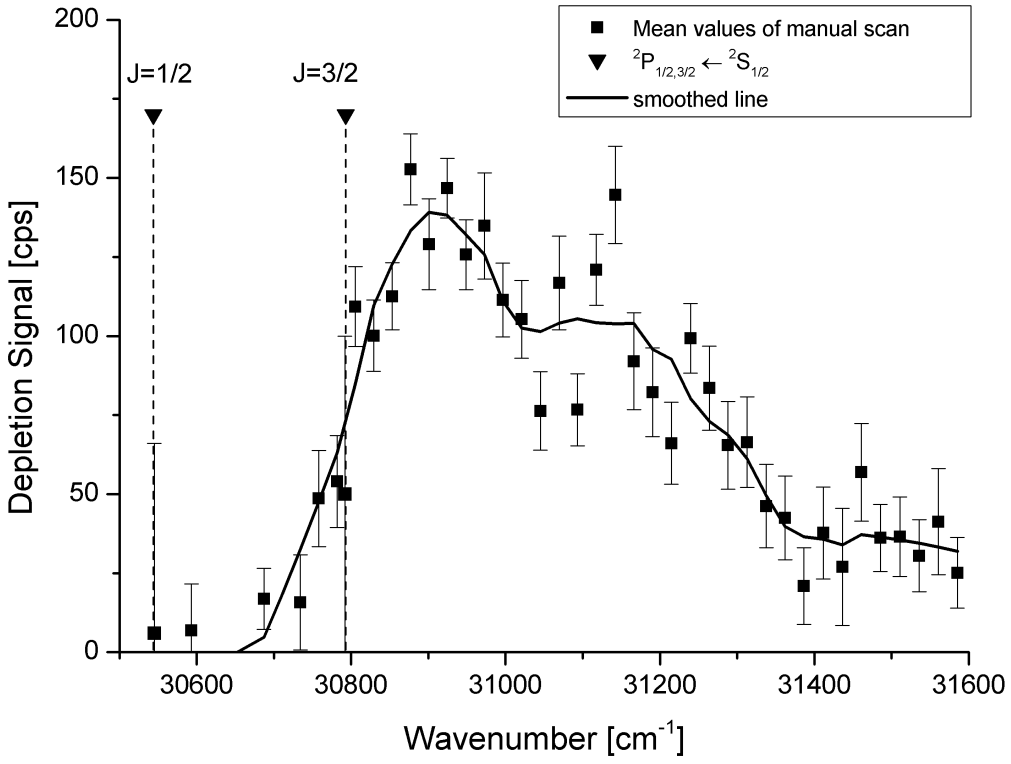

Figure 4.11: Beam depletion spectrum of Cu doped He_N. ($T_{nozzle} = 19\,\mathrm{K}$, $I_{Cu} = 27.5\,\mathrm{A}$; $E_{SHG} = 50 - 100\,\mu\mathrm{J}$; QMS: $M = 63\,\mathrm{u}$, $U_{SEV} = 2700\,\mathrm{V}$, $I_{Fil} = 0.5\,\mathrm{mA}$, tilted voltages)

As described in the experimental section 3.5.2, the need to use SHG introduced issues with beam displacements. While the laser wavelength was scanned over the required range, the laser beam was shifted several millimeters away from its initial position. As the alignment of the droplet beam and the exciting laser plays a crucial role in BD this turned out to be a problem. Therefore, compensation was achieved by realigning and optimising the laser for every chosen excitation wavelength. For continuous scans it was also tried to record spectra without manually tracking the dye laser beam, this resulted in spectra which show an absorption feature in the same region as the manual scan. The shape of the absorption feature is although different from that obtained in the manually tracked scan and varied from scan to scan. Therefore the results of the manual scan are expected to be more reliable than those obtained by continuous scans (figure 4.12b).

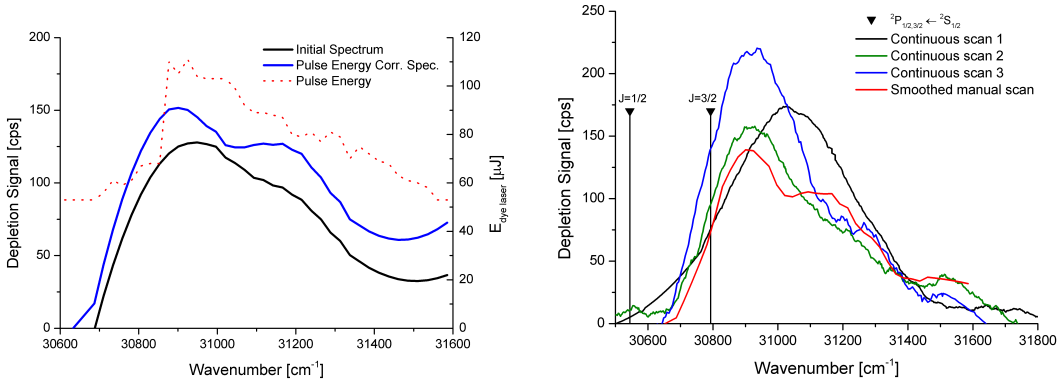

(a) Laser pulse energy correction of the manual scan spectrum.

(b) Comparison of manual and continuous scans.

Figure 4.12: Energy correction and contionuous scans.

The data presented in figure 4.11 was gathered using the following settings for the delay and gate times of the counters (indicated in figure 4.13):

$$A_{delay} = 0.7\,\text{ms} \qquad B_{delay} = 3\,\text{ms} \qquad A_{width} = B_{width} = 3\,\text{ms}$$

Concerning a relatively short laser pulse duration of $20 - 30\,\text{ns}$, this approximately $2 - 3\,\text{ms}$ long depletion signal results from the interaction of one laser pulse with the He_N beam along the whole machine length of approximately 1.5 m. Travelling with a velocity of a few hundred $^m/_s$ it takes milliseconds until the new, undepleted beam part arrives at the QMS.

These counting gate widths and delays after the photodiode trigger pulse were deduced from a delay scan performed at a laser wavelength of 323.35 nm, shown in figure 4.13. The delay time of counter channel A was scanned continuously from zero to ten milliseconds after the trigger pulse while the delay of channel B was fixed at six milliseconds. Both channels had a gate width of one millisecond.

Along with the BD spectra of the Cu atom, also a spectrum of the Cu dimer was recorded. The considered excitation $(c^3\Delta \leftarrow {}^3\Sigma_u^+)$ [1] is expected to be

[1] This triplet transition was chosen because of the similarities in the electron configuration of Cu and alkali metals and the fact that alkali metals form high-spin triplet complexes on the surface of He_N [17]. As well, similar triplet transitions have been reported for Ag_2 in He_N [45].

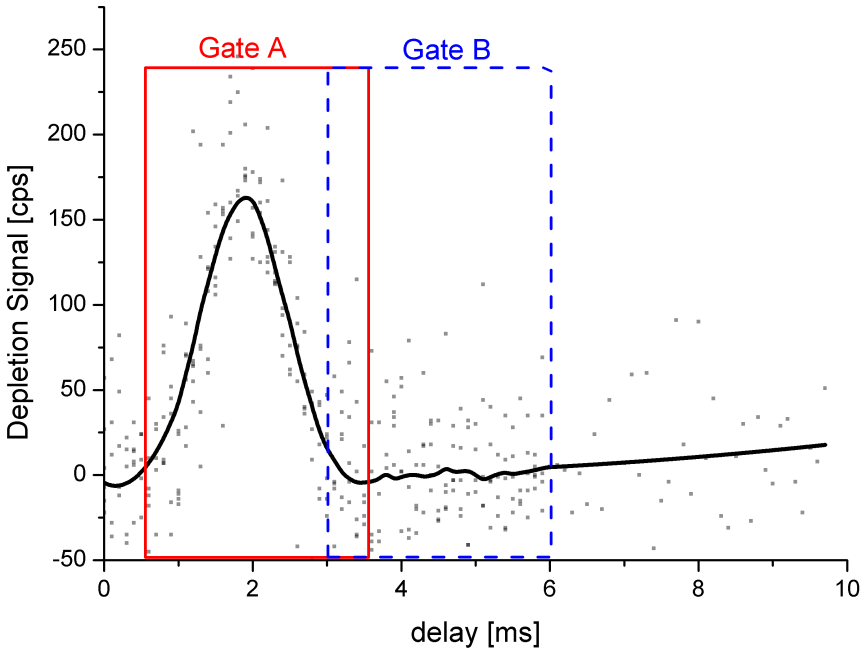

Figure 4.13: Counter delay time scan for BD measurements. ($T_{nozzle} = 19\,\mathrm{K}$, $I_{Cu} = 27.5\,\mathrm{A}$; Laser wavelength: $\lambda = 323.35\,\mathrm{nm}$; QMS: $M = 63\,\mathrm{u}$, $U_{SEV} = 2700\,\mathrm{V}$, $I_{Fil} = 0.5\,\mathrm{mA}$, tilted voltages, Gates set for the BD spectrum in figure 4.11 are indicated.)

centered around 514 nm [46] and can therefore be excited by means of the dye laser without SHG, so the problematic beam displacement did not occur in these measurements. The Spectrum was recorded over a range of two laser dyes (Coumarin 153 and Coumarin 307). However, the signal to noise ratio of the dimer spectrum was much lower than that of the previous atomic measurements and no clear molecular absorption features could be assigned. For completeness the BD spectrum of Cu_2 is shown in figure 4.14.

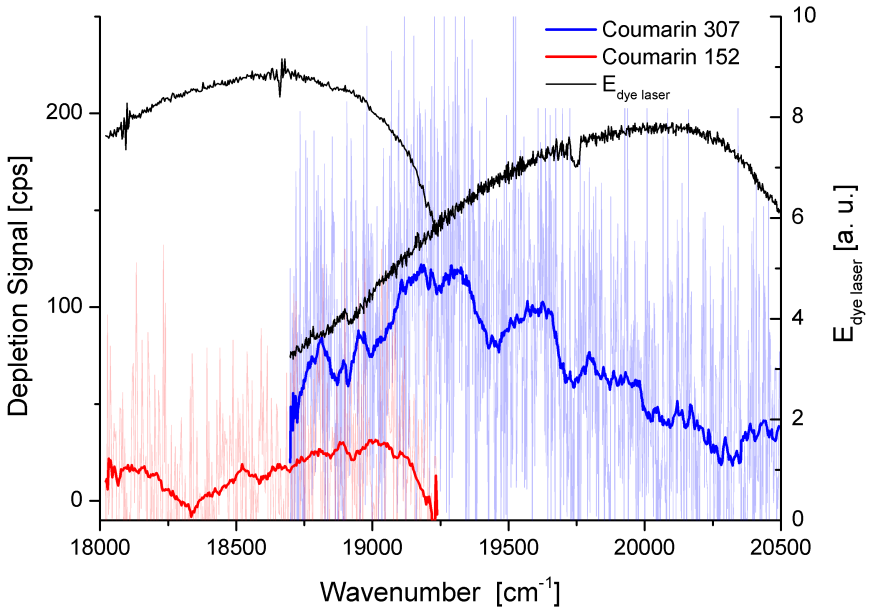

Figure 4.14: BD spectrum of Cu_2 doped He_N. The left scale belongs to the red and blue curve, representing the depletion signals for two different laser dyes. The right scale belongs to the black laser energy curves. ($T_{nozzle} = 15\,\mathrm{K}$, $I_{Cu} = 26\,\mathrm{A}$; QMS: $M = 63\,\mathrm{u}$, $U_{SEV} = 2700\,\mathrm{V}$, $I_{Fil} = 0.5\,\mathrm{mA}$, tilted voltages)

4.4 Laser Induced Fluorescence

The main objective of the LIF measurements was the detection of fluorescent light from the $^2P_{1/2,3/2} \rightarrow {}^2D_{5/2,3/2}$ or $^2D_{5/2,3/2} \rightarrow {}^2S_{1/2}$ transitions after a $^2P_{1/2,3/2} \leftarrow {}^2S_{1/2}$ excitation. The $^2P_{1/2,3/2} \rightarrow {}^2S_{1/2}$ fluorescence was not expected to be well detected for experimental reasons (see section 3.5.3). During the LIF experiments many combinations of experimental conditions were tested, albeit no LIF signal could be observed. In addition to the pulsed LIF described in section 3.5.3, measurements with Continuous Wave (CW) lasers were carried out. The 488 nm and the 514,5 nm line of an Ar^+-laser (Coherent Innova 200) and a 532 nm diode laser (Coherent Verdi-V18), are expected to lie in an absorption band of Cu_2 and were used as excitation radiation. Nevertheless, this different approach did not lead to the detection of fluorescent light. Probable reasons for the absence of fluorescence are discussed in chapter 5.

4.5 Photoionisation

While carrying out the absorption measurements on Cu doped helium nanodroplets, the most promising results were obtained using the photoionisation technique. The gathered PI energy-spectra and PI mass-spectra are presented in this section.

4.5.1 PI Energy-Spectra

In PI experiments the same $^2\mathrm{P}_{1/2,3/2} \leftarrow {}^2\mathrm{S}_{1/2}$ transition as in the BD measurements was examined. Therefore the same laser dye and SHG crystal were used. The whole setup is described in section 3.5.4. The laser pulse energy corrected PI spectrum of Cu doped $\mathrm{He_N}$ in the energy range of the $^2\mathrm{P}_{1/2,3/2} \leftarrow {}^2\mathrm{S}_{1/2}$ transition is shown in figure 4.15 where also the energies of the bare Cu atom transitions $^2\mathrm{P}_{1/2,3/2} \leftarrow {}^2\mathrm{S}_{1/2}$ and $^4\mathrm{D}^\circ_{3/2,5/2} \leftarrow {}^2\mathrm{D}_{3/2}$ [21] are indicated. All assigned features in the figure match the bare atom transition wavenumbers within the measurement uncertainties, as the maximum deviations for the P ← S and D ← D transitions are only eight wavenumbers. The positions of the observed transitions and the NIST [21] values are compared in table 4.3. Further discussion and comparison of the spectrum with beam depletion spectra and theoretical works are given in chapter 5.

Table 4.3: Comparison of observed transition wavenumbers and literature values. ($\bar{\nu}_{obs}$ ... observed wavenumber, $\bar{\nu}_{NIST}$ ... literature value form ref. [21], $\Delta\bar{\nu}$ ... deviation between $\bar{\nu}_{obs}$ and $\bar{\nu}_{NIST}$)

Tansition	$\bar{\nu}_{obs}$ [cm^{-1}]	$\bar{\nu}_{NIST}$ [cm^{-1}] [21]	$\Delta\bar{\nu}$ [cm^{-1}]
$^2P_{3/2} \leftarrow {}^2S_{1/2}$	30538.54	30535.302	3.2
$^2P_{1/2} \leftarrow {}^2S_{1/2}$	30785.56	30783.686	1.9
$^4D^\circ_{5/2} \leftarrow {}^2D_{3/2}$	31169.04	31160.85	8.2
$^4D^\circ_{3/2} \leftarrow {}^2D_{3/2}$	31301.12	31298.716	2.4

All observed transitions are visualised in a Grotrian diagram (see figure 4.16). From the states suitable for PI arrows are drawn up to the ionisation continuum, indicating that ionisation with the 308 nm UV radiation from the XeCl excimer laser is possible. The shaded area directly above the $^2\mathrm{P}_{1/2,3/2}$ excited states

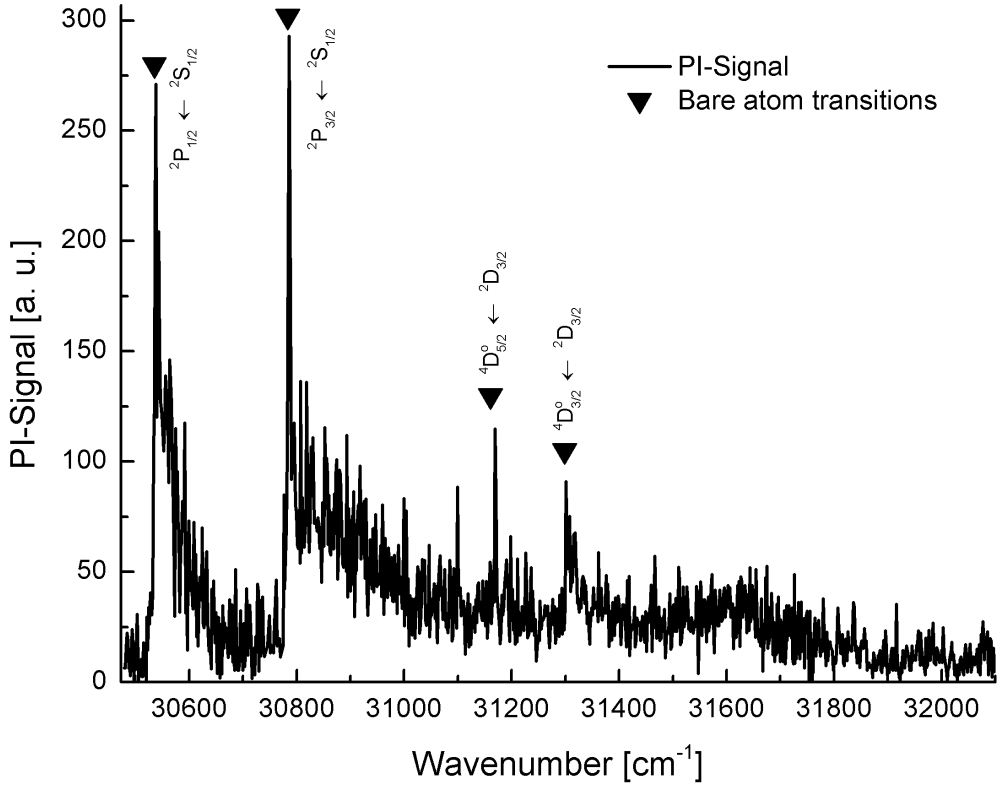

Figure 4.15: PI spectrum of Cu doped He_N. ($T_{nozzle} = 15\,\mathrm{K}$, $I_{Cu} = 26.7\,\mathrm{A}$; $E_{XeCl} = 550\,\mu\mathrm{J}$, SHG laser pulse energy corrected, $E_{SHG} \approx 300\,\mu\mathrm{J}$, $f_{rep} = 100\,\mathrm{Hz}$; QMS: $M = 63\,\mathrm{u}$, $U_{SEV} = 2700\,\mathrm{V}$, $I_{Fil} = 0.5\,\mathrm{mA}$, PI voltages)

indicates the observed droplet-broadened absorption. The dash-dotted vertical line separates the doublet and the quartet system.

The experimental conditions, especially the laser pulse energies where chosen low enough to ensure that non-resonant processes only play a minor role. As a measure for these non-resonant ionisations the simple laser ion yields were noted: $n_{XeCl} \approx 3\,\mathrm{cps}$, $n_{dye} \approx 3\,\mathrm{cps}$ ($\bar{\nu}_{dye} = 31210\,\mathrm{cm}^{-1}$). This is acceptable as it is less than ten per-cent of the average signal in figure 4.15.

As denoted in section 3.5.4, the dye laser beam had to be tracked manually. To show the reproducibility under these circumstances, two subsequent scans under the same experimental conditions were carried out and are compared in figure 4.17. The upper panel of this figure shows the two successively recorded

spectra, the residual of the two spectra is plotted in the lower panel and the mean value (6 cps) and standard deviation (23 cps) are indicated by horizontal lines. As the mean value of the difference signal is quite low and all features in the upper panel appear in both spectra, it is reasonable to say that the manual tracking of the dye laser does not introduce major uncertainties. A constant offset between two subsequent measurements can also be attributed to the long term laser energy variation of the XeCl and dye laser. The relatively large standard deviation can be attributed to the summation of the noise of both measurements. The absence of the features assigned to the D $\leftarrow$ D transitions in figure 4.17 compared to figure 4.15 is probably due to the much lower SHG pulse energy in these measurements.

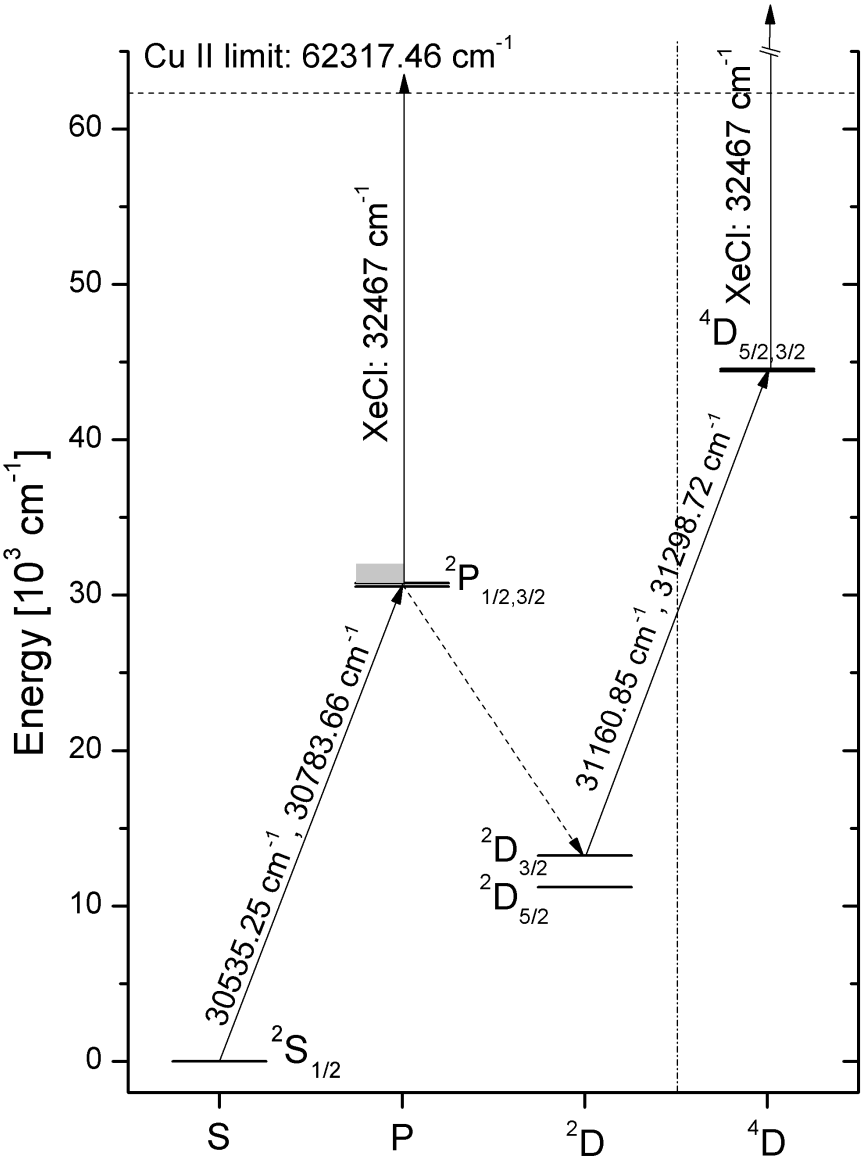

Figure 4.16: Grotrian diagram of Cu. Only states accessed and transitions observed in this work are included. The shaded area marks the observed droplet-bradened absorption. Solid lines indicate observed optical transitions, dashed lines correspond to non-radiative relaxation. The dash-dotted vertical line separates the doublet and the quartet system.

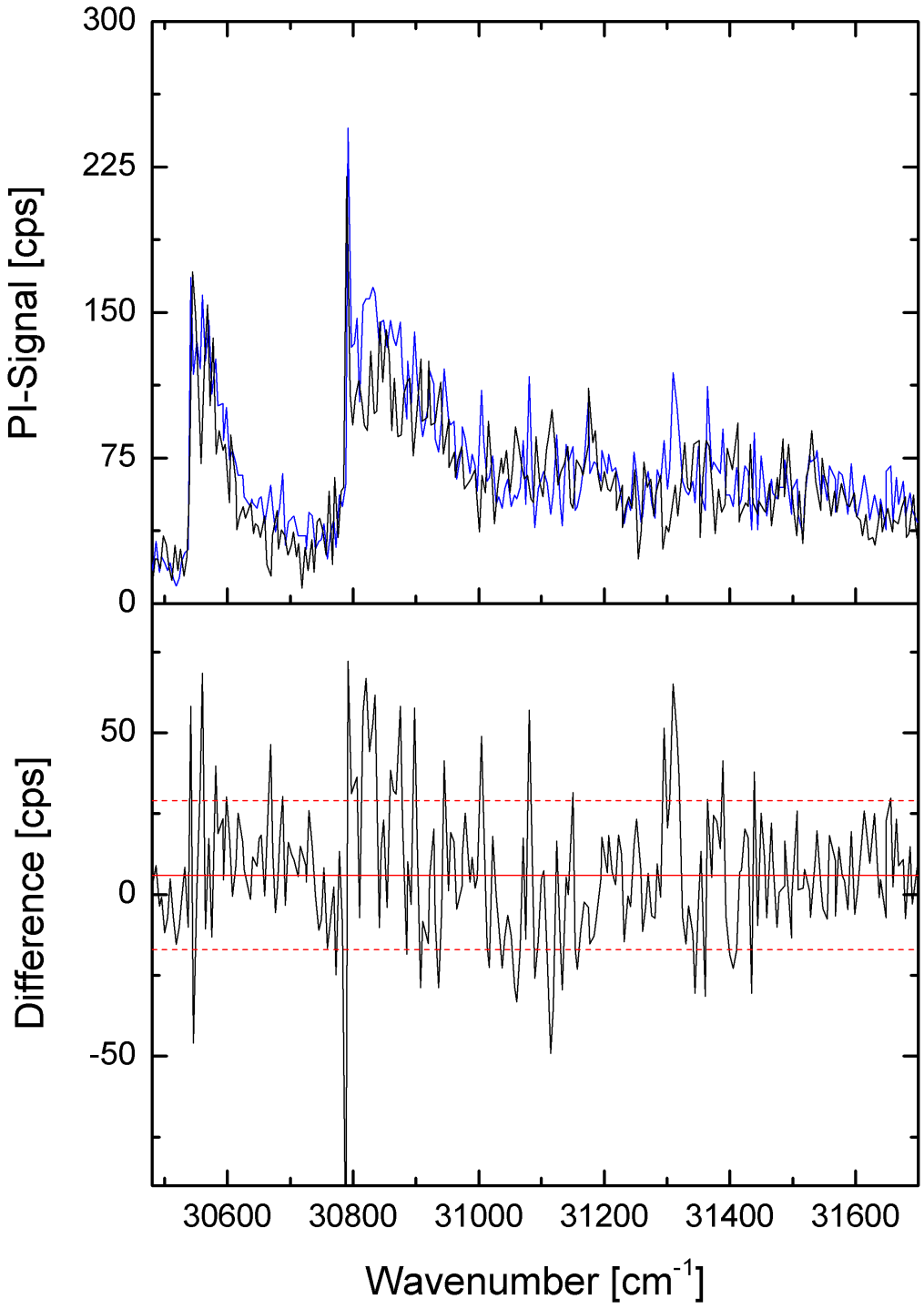

Figure 4.17: Comparison of two subsequent PI scans with identical parameters. ($T_{nozzle} = 15\,\mathrm{K}$, $I_{Cu} = 26.7\,\mathrm{A}$; $E_{XeCl} = 1\,\mathrm{mJ}$, $E_{SHG} \approx 70\,\mu\mathrm{J}$, $f_{rep} = 100\,\mathrm{Hz}$; QMS: $M = 63\,\mathrm{u}$, $U_{SEV} = 2700\,\mathrm{V}$, $I_{Fil} = 0.5\,\mathrm{mA}$, PI voltages)

4.5.2 PI Mass-Spectra

Alongside with the energy (wavelength) dependent spectra, also PI mass-spectra were recorded. This was done with the intention to examine the exciplex formation of Cu and He, therefore PI mass spectra were recorded for several excitation wavelengths and XeCl laser pulse energies. Mass scans were performed with at least ten different sets of experimental conditions. As they all appear very similar, only one scan is shown as an example in figure 4.18. Clearly visible are the bare Cu^+ ions as well as $CuHe^+$. For further analysis of the PI mass spectrum, the counts corresponding to one mass were summed up and plotted as red bars in figure 4.18.

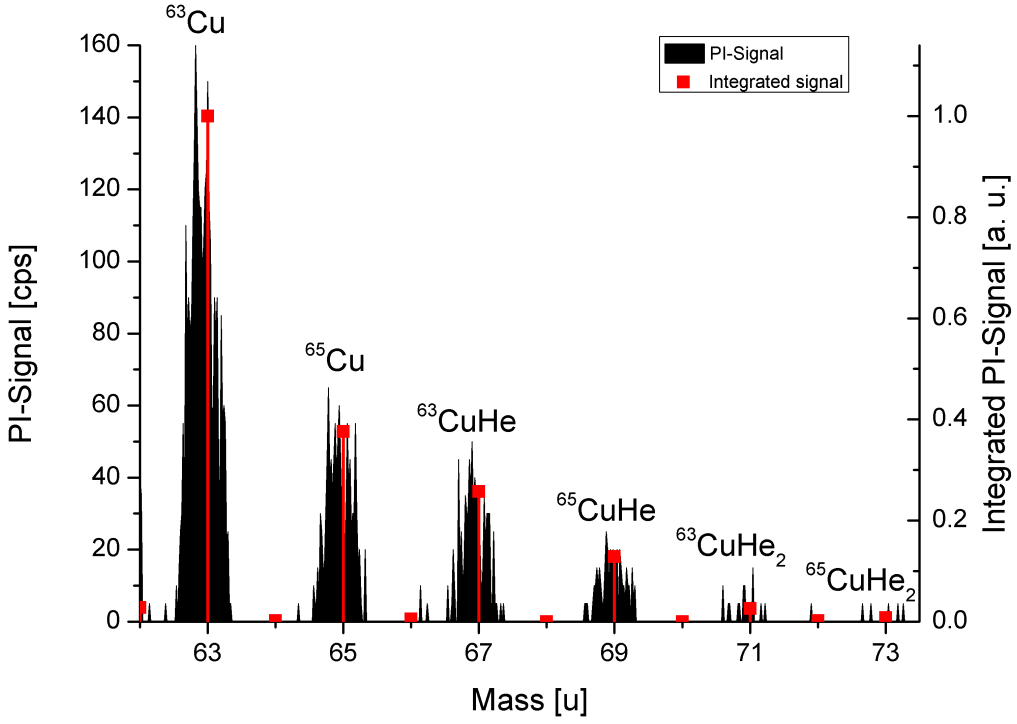

Figure 4.18: PI mass scan of Cu doped He_N. ($T_{nozzle} = 15\,\mathrm{K}$, $I_{Cu} = 26.7\,\mathrm{A}$; $\bar{\nu}_{SHG} = 30900\,\mathrm{cm}^{-1}$, $E_{XeCl} = 3\,\mathrm{mJ}$, $f_{rep} = 100\,\mathrm{Hz}$; QMS: $U_{SEV} = 2700\,\mathrm{V}$, $I_{Fil} = 0.5\,\mathrm{mA}$, PI voltages)

To study the influence of the laser pulse energy on the spectra, a comparison for different XeCl laser pulse energies was carried out by recording several PI mass scans with varying energies that can be found in figure 4.19. The PI

mass-scans presented in this figure were recorded with a dye laser wavelength between 316 nm and 317.5 nm which is clearly out of the area influenced by the strong $^2P_{1/2,3/2} \leftarrow {}^2S_{1/2}$ free atom transitions. For clarity the spectra are normalised to the ^{63}Cu peak. Isotopic shifts are not of concern [47] and so the ^{65}Cu peak should be of the same height in all three spectra. This discrepancy can be attributed to measurement uncertainty and shall be kept in mind for the following considerations.

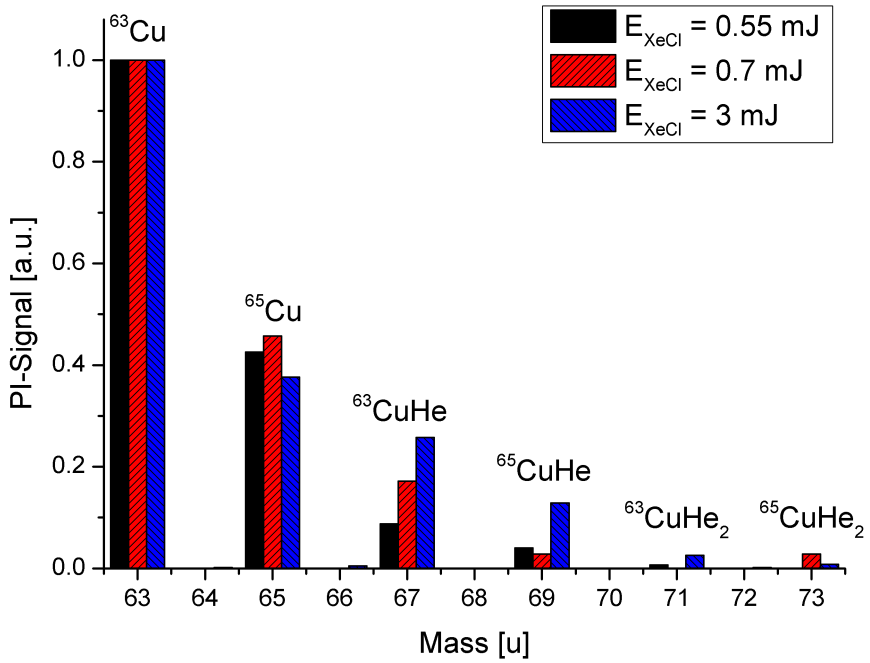

Figure 4.19: Detected ion masses for PI with different XeCl pulse energies ($\bar{\nu}_{SHG} \approx 31400\,\mathrm{cm}^{-1}$).

A clear trend can be deduced from figure 4.19, where a higher XeCl laser pulse energy leads to a higher signal detected at the masses of the CuHe clusters. This fact is most evident at 69 u where the 3 mJ laser energy peak is three times higher than the other two peaks. Therefore, the effect dominates the uncertainty which can be estimated from the 65 u peak.

One could also do a similar comparison for different excitation laser wavelengths. This is shown in figure 4.20 which also includes the case of solely non-resonant ionisation with the XeCl laser. While the progression of the peaks is very similar in the first two cases (dye laser on), a clear difference from that pattern

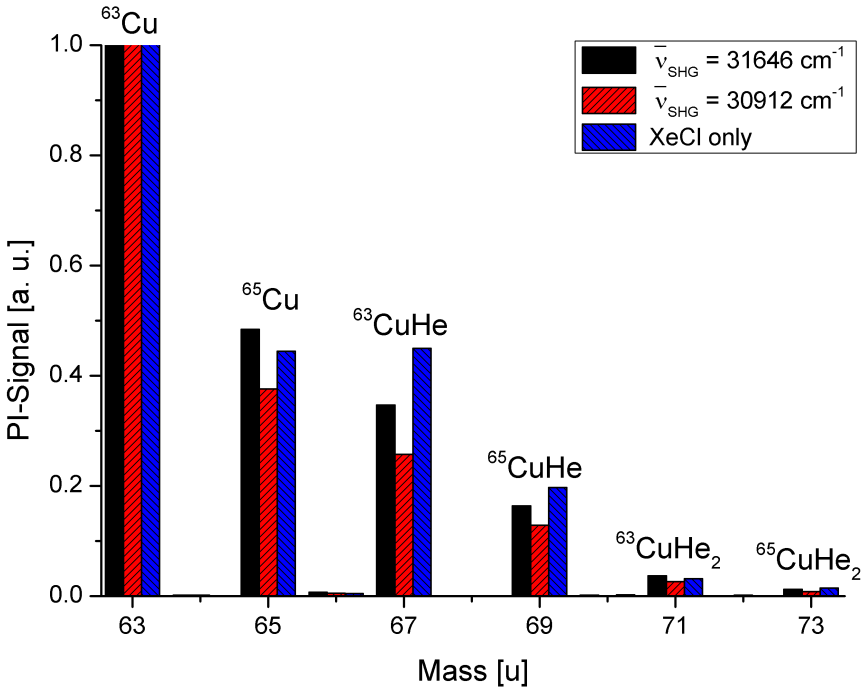

Figure 4.20: Detected ion masses for PI with different excitation laser wavelegths.

is visible in the third case (XeCl laser only). In the latter case the peaks at 67 u and 69 u, associated with ^{63}CuHe and ^{65}CuHe, respectively, are higher compared to the others. This indicates that in the case of solely non-resonant excitation and further ionisation with the XeCl laser the relative amount of Cu-He complexes is higher than in the resonant case. In conclusion, figures 4.19 and 4.20 suggest that a high intensity XeCl laser is favourable for the ejection of Cu atoms out of the droplet which tend to stick to one helium atom.

5 Discussion

The objective of this chapter is the general discussion of the results in chapter 4, especially by linking results from different measurement techniques and comparing them with literature data.

5.1 Electronic Excitations

In a first step of analysis the results of the BD and PI shall be compared. Both spectra are shown in figure 5.1. The most evident difference between the BD and the PI spectrum is the existence of sharp lines at the bare atom transitions in the case of PI, and the absence of these peaks in the BD spectrum.

One possible scenario is that some of the Cu atoms are "spit out" of the droplet by the interaction with the XeCl laser beam, subsequently excited by the dye laser and ionised by a further XeCl laser photon. A 1CR2PI measurement would be a good way to prove this theory, unfortunately, in principle this is not possible as the energy of a second SHG-photon below $31158\,\mathrm{cm}^{-1}$ is not sufficient to reach the free atom ionisation limit. If the excited Cu atom relaxes to the lowest J state, like it was observed for Cr in He_N [48], the threshold for 1CR2PI has an even higher value of $31782\,\mathrm{cm}^{-1}$. Another factor that limits 1CR2PI is the low SHG pulse energy, which might not lead to a sufficient ion yield due to the relatively small cross section of the ionisation step [47]. Therefore, the BD experiments remain the only spectra recorded in the absence of the XeCl laser. Considering this, the PI spectrum in figure 5.1 includes

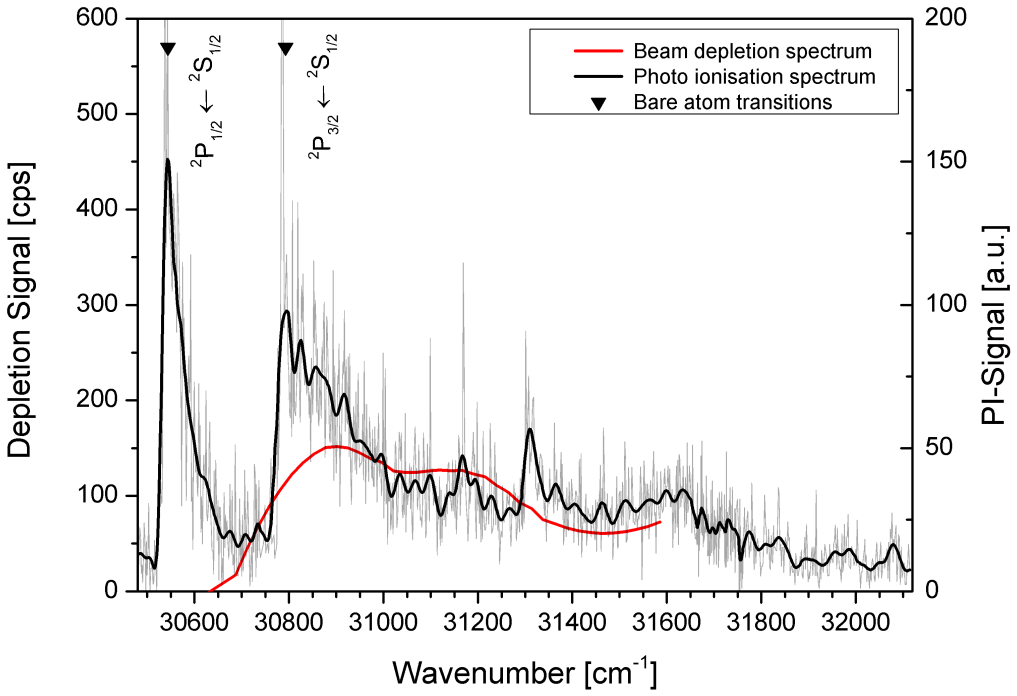

Figure 5.1: Comparison of BD and PI spectra (Both spectra are laser pulse energy corrected. Expermental conditions are stated in the captions of fig. 4.15 and 4.11).

the superposition of a droplet broadened feature and sharp atomic lines. The peak of the $^2P_{1/2} \leftarrow {}^2S_{1/2}$ transition is separated from the rest of the features, therefore, it gives an idea for the line shape of all atomic transitions. They consist of a sharp peak at the free atom transition energy and an $80\,\mathrm{cm}^{-1}$ wide wing to the blue side of the feature. Estimating a similar line shape for the $^2P_{3/2} \leftarrow {}^2S_{1/2}$ transition, a width of $1000\,\mathrm{cm}^{-1}$ can be assigned to the droplet broadened feature. The onset of the feature is blue-shifted by $300\,\mathrm{cm}^{-1}$ which is of comparable magnitude to the spin-orbit splitting. The BD spectrum shows the same blue-shift although, as far as the covered measurement range allows to tell, it is narrower than the PI spectrum. It can be expected that an extension of the BD measurement range and the reduction of the beam deviation would allow a better comparison of the absorption widths in both cases.

Cargnoni and Mella [8] performed an investigation of the solubility of Cu and Ag atoms in He_N by means of a Diffusion Monte Carlo DMC approach and

calculated the absorption spectra for both species using the Lax approximation. Figure 5.2 shows the comparison of the measured PI spectrum (figure 4.15) and two theoretical absorption spectra for a Cu atom submerged in a He_N [8] which are scaled to fit the measured spectrum. The red line represents the calculated absorption spectrum of a Cu atom solvated in a He_N consisting of 100 He atoms. The similar calculation for only twelve helium atoms leads to the blue curve. While the theoretical spectrum for the smaller droplet (blue) clearly shows two separated absorption peaks, one for each spin-orbit component, the spectrum corresponding to the $N = 100$ droplet is blurred out to one wide absorption feature. Between $31000\,cm^{-1}$ and $32000\,cm^{-1}$ the measured PI-signal corresponds very well with the calculated curve for He_{100}. However, the low energy part of the spectrum towards the free atom transitions, diverges significantly from the red curve. This part is in better agreement with the blue curve and so it appears that the PI spectrum is somehow composed of a superposition of both theoretical spectra, which means both small and big droplets contribute to the signal. This strengthens the assumption that the XeCl laser ejects a portion of the Cu atoms from the droplets, leaving them with no, or just a few, helium atoms attached. The peaks of the PI spectrum and the theoretical $CuHe_{12}$ spectrum are separated by $130\,cm^{-1}$, suggesting that $CuHe_{12}$ is not the observed species. Cargnoni and Mella found that the peaks of the $^2P_{1/2,3/2} \leftarrow {}^2S_{1/2}$ transitions are broadened and blue shifted monotonously as the number of helium atoms is increased from twelve to 100 (see figure 5.3). Unfortunately they did not publish any spectra calculated for smaller He_N-clusters, but it can be estimated that the absorption maxima lie somewhere in between the free atom transitions and the $CuHe_{12}$-peaks. Therefore, the peaks observed in the PI spectrum may be assigned to a species of $CuHe_N$ with $N < 12$. For further analysis, the simulated absorption spectrum of Cu in He_{100} (red curve in figure 5.2) was subtracted from the measured PI spectrum (black curve in figure 5.2), the result is depicted in figure 5.4. The resulting shape of the $^2P_{3/2} \leftarrow {}^2S_{1/2}$ transition differs from that of the $^2P_{1/2} \leftarrow {}^2S_{1/2}$ as it is wider. The shape of the two transitions reminds of the D-lines of the heavy alkali metals, rubidium and caesium attached to the surface of He_N [32]. This can be attributed to the similar electron configuration and the interaction of the "spit out" Cu with only a few He atoms attached.

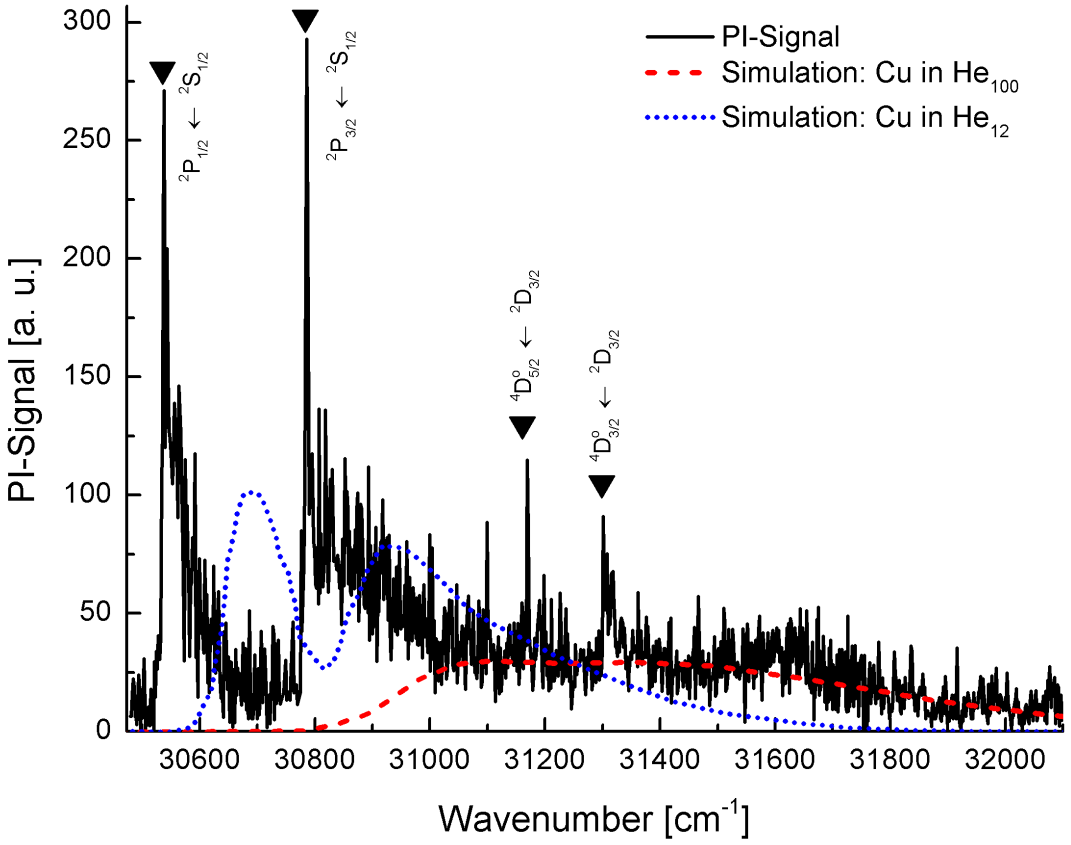

Figure 5.2: Comparison of the Cu PI spectrum and theoretical excitation spectra. (The two theoretical spectra were digitised out of reference [8] and scaled to fit the measured spectrum. The experimental conditions are stated in the caption of figure 4.15)

So far the discussion of the PI spectrum was focussed on the features of the $^2P_{1/2,3/2} \leftarrow {}^2S_{1/2}$ transition, however, this is not the only observed transition in the considered wavelength region. Two additional peaks are observed at 31167 cm^{-1} and 31307 cm^{-1} where two intercombination transitions $^4D^\circ_{5/2} \leftarrow {}^2D_{3/2}$ and $^4D^\circ_{3/2} \leftarrow {}^2D_{3/2}$ are catalogued [49]. These observed lines show the same characteristics as the $^2P_{1/2,3/2} \leftarrow {}^2S_{1/2}$ lines, consisting of a sharp peak and a tail to the high energy side. All other transitions between the ^2D and the $^4D^\circ$ states are located well outside the considered wavelength region and are therefore not observed. Contrary to the $^2P_{1/2,3/2} \leftarrow {}^2S_{1/2}$ transitions the $^4D^\circ_{3/2,5/2} \leftarrow {}^2D_{3/2}$ transitions do not share the $^2S_{1/2}$ Cu ground state as their common initial state. The metastable $^2D_{3/2}$ state can be accessed from

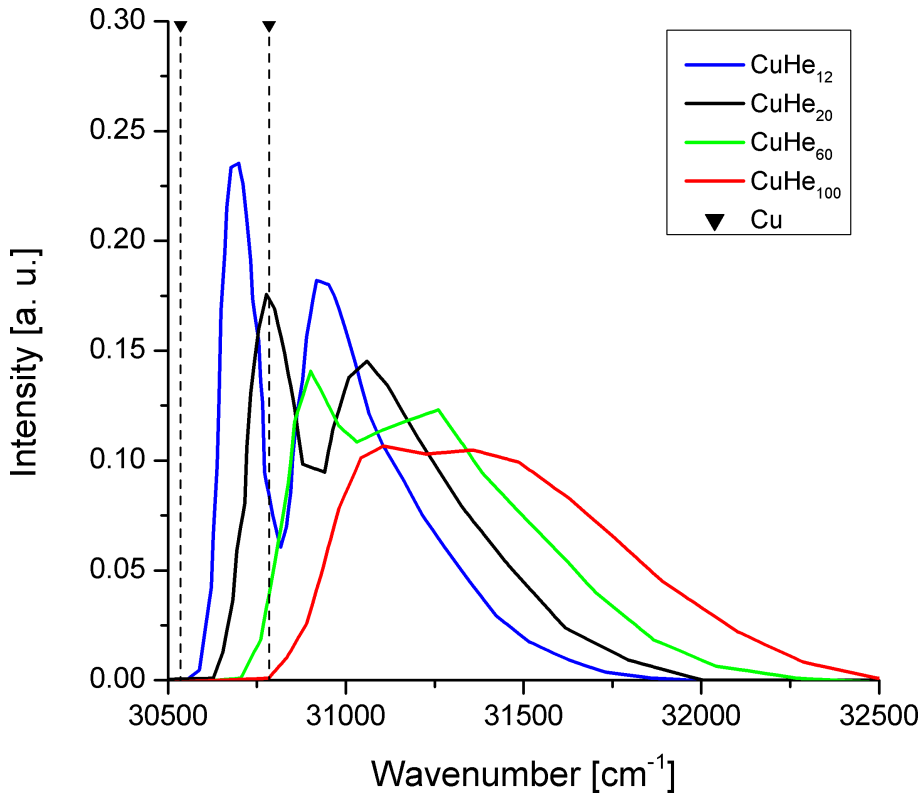

Figure 5.3: Theoretical absorption spectra for different He_N sizes. (adopted from reference [8])

the excited $^2P_{1/2,3/2}$ state by radiative and non-radiative relaxation (see figure 4.16 for the Grotrian diagram of Cu). As no fluorescence for this relaxation was measured, the non-radiative mechanism is to be favoured. The appearance of the two lines as sharp peaks at the bare atomic transition with a wing at high energy side, suggests that the atoms in the metastable state are free atoms or have a small number of helium atoms attached to them. It therefore seems reasonable that upon excitation and ejection of the Cu atoms they relax to the ground state and to the metastable state.

One more feature is the bump at the high energy side of the droplet-broadened absorption band in the PI spectrum (figure 5.2). This feature at approximately $31600\,cm^{-1}$ may not seem to be very significant in comparison to the other peaks, nevertheless it should be mentioned that similar peaks appear in the PI spectra of Cr in He_N(figure 5.6). Figure 5.5 shows the $CuHe_N$ PI spectra for two different pulse energies of the XeCl ionisation laser. At the first sight it is

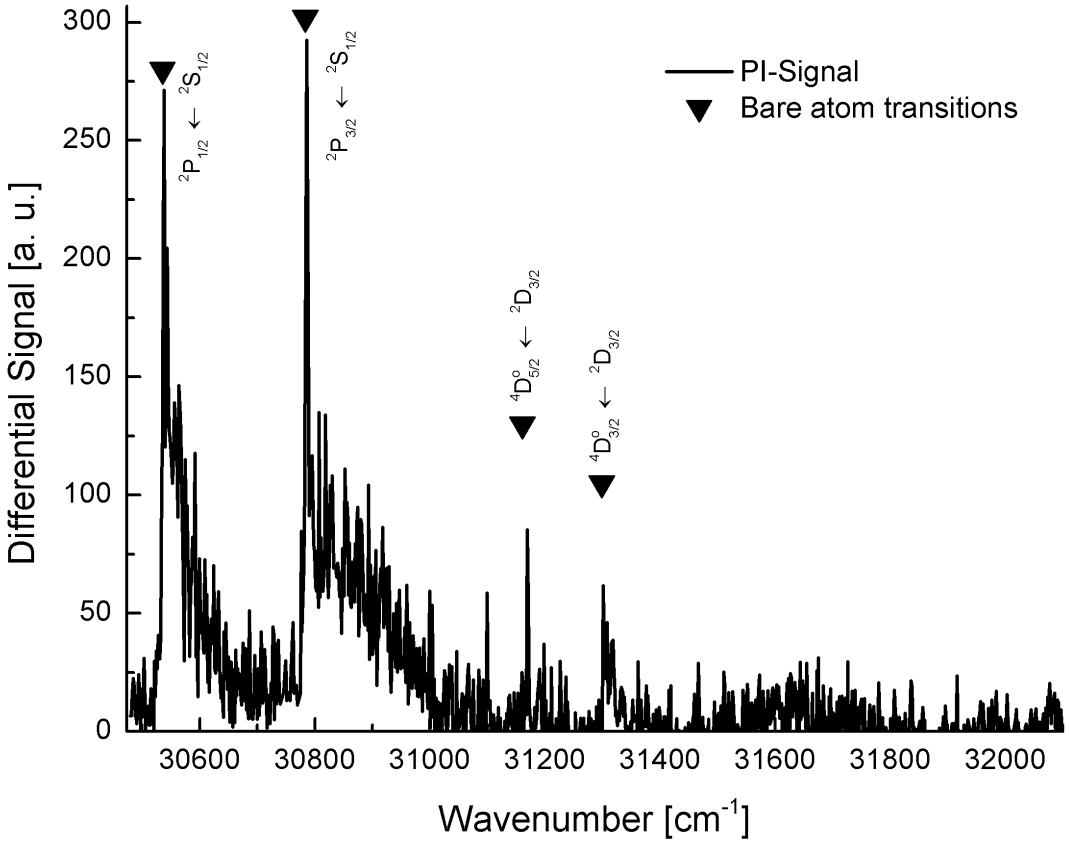

Figure 5.4: Difference of measured PI spectrum (black curve in figure 5.2) and simulated absorption spectrum for Cu in He_{100} (red curve in figure 5.2).

clear that the attenuation of the XeCl laser to almost one tenth of its initial energy has a significant impact on the PI spectrum. Primarily, the overall intensity is diminished, but it is also evident that the bump at 31600 cm^{-1} is less affected by the decrease of the XeCl laser pulse energy than all the other features of the spectrum are, suggesting that it may be ascribed to a process associated exclusively with the dye laser. This is reasonable because one colour PI becomes possible for free atoms at an excitation laser energy of 31158.73 cm^{-1}, which equals half the ionisation potential.

Another possible explanation for this bump can be given by examination of the two $^4D^\circ_{3/2,5/2} \leftarrow {}^2D_{3/2}$ transitions. As argued above, the $^2D_{3/2}$ state is populated after excitation with a laser photon. These metastable Cu atoms are

either free or bound to a few helium atoms resulting in the sharp transition lines in the PI-spectra. The fact that the bump is also quite intense with low XeCl laser pulse energy suggests that after resonant excitation into the droplet broadened $^2P_{1/2,3/2}$ state a non radiative relaxation into the $^2D_{3/2}$ state might take place. During this relaxation approximately 3500 helium atoms are evaporated. The relatively large droplet size in the PI experiments ($\bar{N} \approx 12000$) leads to the possibility that some doped droplets survive this relaxation and are available for further excitation. These submerged Cu atoms in the metastable $^2D_{3/2}$ state are excited to the $^4D^\circ_{3/2,5/2}$ states by a second dye laser photon and subsequently ionized, yet by another dye laser or XeCl laser photon. This would lead to a droplet broadened feature which is blue-shifted with respect to the free atom $^4D^\circ_{3/2,5/2} \leftarrow {}^2D_{3/2}$ transitions exactly like the bump in question is.

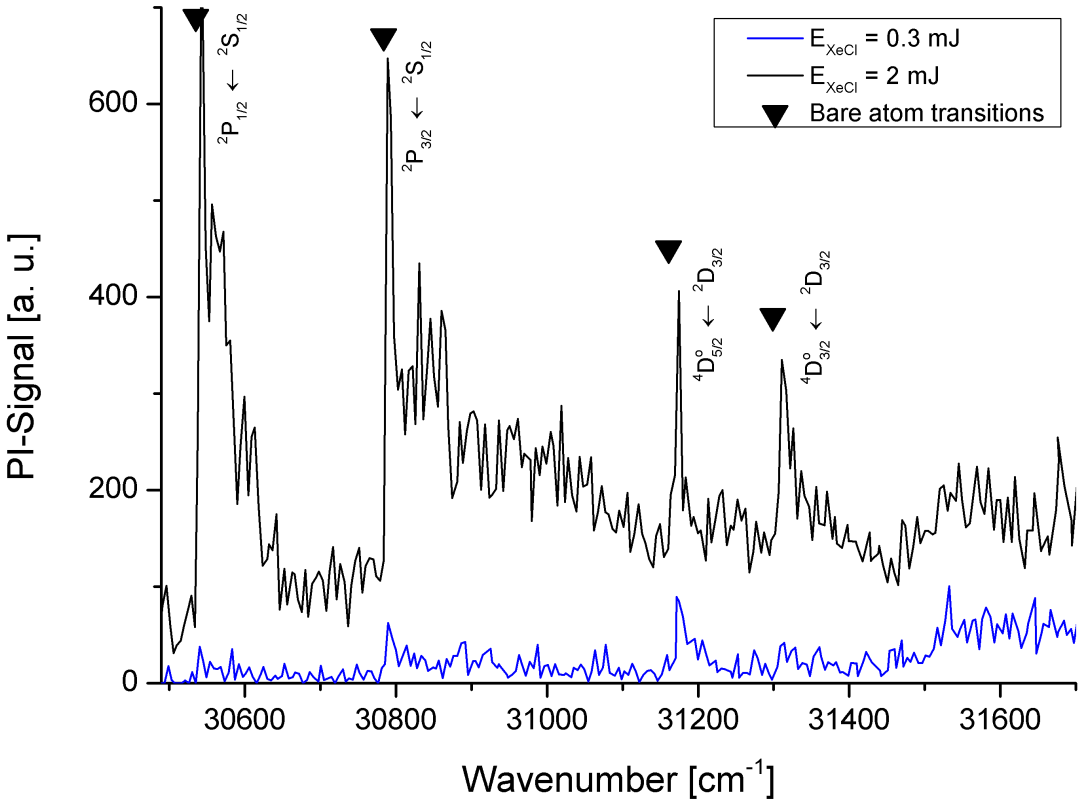

Figure 5.5: PI spectra for two different XeCl laser pulse energies. ($T_{nozzle} = 15\,\mathrm{K}$, $I_{Cu} = 26.7\,\mathrm{A}$; SHG Laser pulse energy corrected, $E_{SHG} \approx 330\,\mu\mathrm{J}$, $f_{rep} = 100\,\mathrm{Hz}$; QMS: $M = 63\,\mathrm{u}$, $U_{SEV} = 2700\,\mathrm{V}$, PI voltages)

To complete the discussion of the PI spectrum, it is compared with a Cr in He_N PI spectrum recorded with a comparable measuring arrangement. A PI spectrum in the wavelength range of the Cr $z^7P_{2,3,4} \leftarrow a^7S_3$ transition is plotted in figure 5.6. This is an allowed transition with three spin-orbit components, with all of them clearly apparent in the PI spectrum. The three peaks are composed of a sharp peak at the free atom transition wavelength and a wing to the high energy side, which is in agreement with the findings for Cu. As well, the three free-atom lines seem to be superimposed to an $\sim 600\,\mathrm{cm}^{-1}$ wide droplet-broadened feature, stretching from $23400\,\mathrm{cm}^{-1}$ to approximately $24000\,\mathrm{cm}^{-1}$. This width is comparable to that observed for the Cu transition ($1000\,\mathrm{cm}^{-1}$).

In the $CrHe_N$ PI spectrum (figure 5.6) a similar bump at the high energy side of the broadened absorption feature appears as it does for $CuHe_N$. It is stronger for Cr than it is for Cu which might be attributed to the experimental conditions. Except for the intensity, the two features have comparable properties. The width of the Cu (Cr) bump is approximately $100\,\mathrm{cm}^{-1}$ ($70\,\mathrm{cm}^{-1}$) and it is blue-shifted from the center of the droplet-broadened absorption by $\sim 280\,\mathrm{cm}^{-1}$ ($\sim 340\,\mathrm{cm}^{-1}$). Unfortunately, also for Cr this bump still lacks of a clear explanation.

The comparison of the PI spectra of Cu and Cr doped helium nanodroplets shows that, despite the coarse differences in electron configuration and excitation energy between the two species, both spectra are composed of similar features. Therefore, the examination of Cu doped helium nanodroplets could give valuable hints in understanding the even more complicated processes in Cr doped helium nanodroplets.

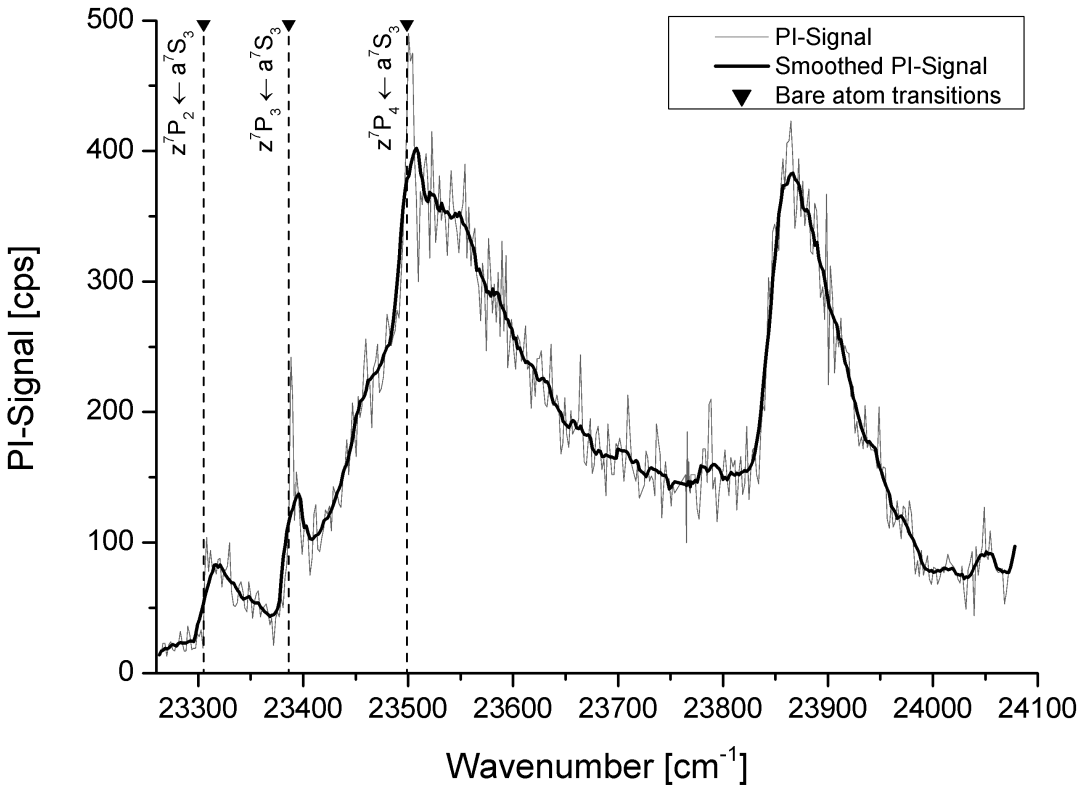

Figure 5.6: PI spectrum of Cr doped He_N. ($T_{nozzle} = 20\,\mathrm{K}$, $P_{Cr} = 180\,\mathrm{W}$; $E_{dye} = 300\,\mu\mathrm{J}$, $E_{XeCl} = 200\,\mu\mathrm{J}$, $f_{rep} = 100\,\mathrm{Hz}$; QMS: $M = 52\,\mathrm{u}$, $U_{SEV} = 2700\,\mathrm{V}$, PI voltages)

5.2 Deexcitation

In this section reasons for the absence of fluorescent light are discussed. It has to be noted, that the argumentation has a speculative nature because the ability of UV detection with this setup is not clear, as stated in the experimental section.

For the discussion all states below the $^2P_{1/2,3/2}$ state and the chosen laser excitation with possible deexcitation pathways are depicted in figure 5.7. All the transitions plotted were observed either in the gas phase [49] or in matrix [5].

After excitation into the $^2P_{1/2,3/2}$ state, there are basically two options for

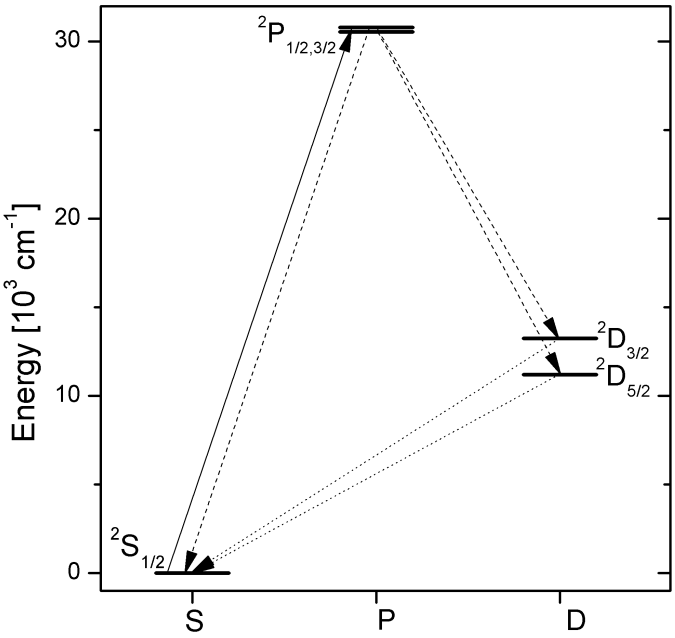

Figure 5.7: Energy level diagram of Cu. The solid line corresponds to the excitation. Dashed lines represent allowed and dotted lines forbidden transitions. The two sub states of the ^{2}P state are treated as one for clarity.

relaxation pathways. First, there is direct radiative relaxation to the ground state. The second possibility is the relaxation into the metastable $^2D_{5/2,3/2}$ state. This $^2P_{1/2,3/2} \rightarrow^2 D_{5/2,3/2}$ transition is also dipole allowed, therefore fluorescent light emission is again possible. A subsequent transition between the $^2D_{5/2,3/2}$ and the $^2S_{1/2}$ states is strictly parity forbidden because both the $^2S_{1/2}$ and the ^{2}D are even states (see table 2.1). To summarise, allowed dipole transitions are the direct $^2P \rightarrow {}^2S$ transition to the ground state and the $^2P \rightarrow {}^2D$ transition to the metastable dark state. With the transition rules applying, all of these transitions were observed by fluorescence in the gas phase [49]. So it has to be discussed, why none of these radiative transitions were observed in the case of Cu doped He_N. The direct $^2P \rightarrow {}^2S$ fluorescence is in the UV range and can therefore hardly be detected with the current measurement setup. This means that further measurements with an improved setup should be performed for clear results. On the other hand, the absence of fluorescent emission on the well detectable $^2P \rightarrow {}^2D$ transition suggests that similar quenching mechanisms

as in solid rare gas matrices [5, 6] inhibit the radiative relaxation of the dipole allowed transitions. In solid rare gas matrices and in bulk liquid He the two allowed transitions were not observed which was attributed to quenching by the strong coupling of the dopant to phonons in the matrix [5] or to Cu^*He_n exciplex formation [6, 50]. One possible scenario after the excitation into the $^2P_{1/2,3/2}$ state is the "spit out" of the Cu atom from the droplet, since the potential energy surface of this excited state has a repulsive component [8]. A similar ejection mechanism was observed for photoexcited silver atoms [51, 52]. It is possible that the photoinduced ejection of the Cu is associated with a non-radiative relaxation to the lower lying states, as it was observed for Cr in He_N [53]. This quenching mechanism might inhibit the fluorescence of the $^2P_{1/2,3/2} \rightarrow^2 S_{1/2}$ and the $^2P_{1/2,3/2} \rightarrow^2 D_{5/2,3/2}$ transitions.

Despite the lack of fluorescence on the dipole-allowed transitions, fluorescent light originating from the parity forbidden $^2D \rightarrow {}^2S$ transition was observed in solid rare gas matrices [5] and, although weaker, in bulk liquid He [6]. This is possible because selection rules are weakened by the dopant-matrix interaction [5]. Similar transitions were also observed for the other coinage metals gold [54] and silver [55] in rare gas matrices. Concerning the $^2D \rightarrow {}^2S$ transition, in liquid, and especially in superfluid He this fluorescence is poorly observable, due to the long decay times ($\sim 100\,\mathrm{ms}$), the atoms diffuse out of the observation volume faster than a photon is emitted [56].

Cu atoms doped to He_N could in principle reach the ^2D metastable level by several pathways: First, a radiative transition from the ^2P state, which was excluded above. Then there is the nonradiative transition, which includes the "spit out" of the dopant due to the repulsive potential of the excited state [8], resulting in a metastable bare atoms. Thirdly, there might be a low probability of an attractive potential so that during the relaxation the Cu resides inside the droplet, passing its excess energy to the surrounding He by coupling of vibrational modes. This raises the droplet temperature above the equilibrium temperature so helium is evaporated from the surface, carrying away the He-binding energy of $5\,\mathrm{cm}^{-1}$ per atom [2]. Thus the energy release from the ^2P to the ^2D state results in a droplet shrinkage of 3800 He atoms. The He_N size for the LIF experiments was chosen rather small ($\bar{N} \approx 6000, T_{nozzle} = 19\,\mathrm{K}$)

because of the good experiences made with LIF of Cr atoms [57], but still a fraction of droplets would survive this shrinkage leading to submerged atoms in the ^{2}D state.

In either of the latter cases when the Cu is in the free atom metastable state or even if the $^2\mathrm{D} \rightarrow {}^2\mathrm{S}$ transition becomes allowed because of the interaction with He, it seems reasonable that the velocity of the $\mathrm{He_N}$ beam is sufficient to leave the observation volume within the lifetime of the metastable state leading to no detectable fluorescence from this channel.

These considerations might answer the question why no fluorescent light originating from Cu doped $\mathrm{He_N}$ was detected. Although, to be sure the measurements should be repeated with an improved experimental setup, like a fluorescence detection that is designed for UV light and a CW laser for wavelengths in the appropriate region. In the unlikely case that a part of the Cu stays inside the droplet, another issue worth re-assessment is the dependency of the de-excitation on the droplet size, as it is possible that larger droplets survive a non-radiative relaxation to the metastable ^{2}D state. If additionally, the gas phase forbidden $^2\mathrm{D} \rightarrow {}^2\mathrm{S}$ transition happens on a short time scale, fluorescence might be observed.

6 Conclusions and Outlook

During the course of this work Cu and Cr doped helium nanodroplets were investigated by exploiting both mass and optical spectroscopy. Preliminary measurements concerned the characteristics of the Cu evaporation source where the source temperature dependence on the heating current was determined. Mass spectra of Cu doped He_N revealed that small Cu clusters with up to seven atoms were formed. In a further step the doping characteristics of Cu to He_N were examined, yielding the optimal pickup conditions for small Cu clusters, which are in coarse agreement with literature findings [3]. The sequential doping of He_N with Cu and Cr lead to the formation of mixed CrCu clusters. CrCu, Cr_2Cu, $CrCu_2$ and $CrCu_3$ were identified and an investigation of their doping characteristics was carried out.

Electronic excitation spectra of Cu doped He_N were obtained exploiting the Photo Ionisation (PI) and Beam Depletion (BD) methods. The PI and BD spectra show a similar droplet broadened absorption assigned to the $^2P_{1/2,3/2} \leftarrow {}^2S_{1/2}$ transition. The appearance of sharp lines at the positions of the free atom transitions in the PI spectrum suggests the ejection of a portion of the dopants by the interaction with the ionising laser. These and other features in the spectra of Cu doped He_N show similarities to those of Cr doped He_N. The similarities of Cu and Cr doped droplets can help to understand the complex excitation dynamics of Cr by investigating the alkali-like Cu atom. The observed excitation spectrum is also in very good agreement with theoretical results in literature [8]. The comparison of measured and simulated spectra supports the assumption that the Cu dopants are ejected from the droplet and subsequently excited and ionised as bare atoms. Laser Induced Fluorescence (LIF) measurements were carried out in order to achieve more information

about the relaxation pathways, however, no fluorescent light was detected suggesting fluorescence is effectively quenched by the surrounding He_N.

The possibility to produce small pure (Cu_n, Cr_n) and mixed (Cr_nCu_m) clusters in a confined, cold environment opens a wide field of further studies where a primary step would be the investigation of the light absorption over a wide wavelength range. Further fluorescence measurements with improved experimental conditions could yield an insight in the comparability of Cu atoms doped to He_N and in matrix [56].

Abbrevations

1CR2PI	one Colour Resonant two Photon Ionisation.
2CR2PI	two Colour Resonant two Photon Ionisation.
ASE	Amplified Spontaneous Emission.
BD	Beam Depletion.
CW	Continuous Wave.
d_{nozzle}	nozzle diameter.
DMC	Diffusion Monte Carlo.
ESR	Electron Spin Resonance.
GPIB	General Purpose Interface Bus.
He_N	helium nanodroplets.
HENDI	Helium Nano Droplet Isolation.
I_{Cu}	Cu source heating current.
I_{fil}	QMS filament current.
LIF	Laser Induced Fluorescence.
MCD	Magnetic Circular Dichroism.
p_{He}	helium nozzle pressure.
PC	Pockels Cell.
PI	Photoionisation.
PID	Proportional Integral Derivative.
PMT	Photo Multiplier Tube.
QMS	Quadrupole Mass Spectrometer.
SEM	Secondary Electron Multiplier.
T_{nozzle}	nozzle temperature.
U_{Cu}	Cu source heating voltage.

Bibliography

[1] J. D. Aiken III, R. G. Finke. A review of modern transition-metal nanoclusters: their synthesis, characterization, and applications in catalysis. *Journal of Molecular Catalysis A: Chemical* **145** (1999) 1

[2] C. Callegari, W. Ernst. *Helium Droplets as Nanocryostats for Molecular Spectroscopy - from the Vacuum Ultraviolet to the Microwave Regime. - in: Handbook of High-Resolution Spectroscopy, edited by F. Merkt and M. Quack.* John Wiley & Sons, Chinchester, 2011

[3] P. L. Stiles, R. E. Miller. Structures and Bonding Nature of Small Monoligated Copper Clusters ($HCN - Cu_n, n = 1 - 3$) through High-Resolution Infrared Spectroscopy and Theory. *The Journal of Physical Chemistry A* **110** (2006) 10225

[4] M. Moskovits, J. E. Hulse. The UV-visible spectra of copper atoms isolated in various matrixes. *The Journal of Physical Chemistry* **85** (1981) 2904

[5] G. A. Ozin, S. A. Mitchell, J. Garcia-Prieto. Fluorescence spectroscopy and photoprocesses of copper, Cu and Cu_2 in rare gas matrixes. *The Journal of Physical Chemistry* **86** (1982) 473

[6] P. Moroshkin, V. Lebedev, A. Weis. Laser ablation and spectroscopy of copper in liquid and solid ^{4}He. *Physical Review A* **84** (2011) 052519

[7] E. Vehmanen, V. Ghazarian, C. Sams, I. Khachatryan, J. Eloranta, V. A. Apkarian. Injection of Atoms and Molecules in a Superfluid Helium Fountain: Cu and $Cu_2He_n(n = 1, ..., \infty)$. *The Journal of Physical Chemistry A* **115** (2011) 7077

[8] F. Cargnoni, M. Mella. Solubility of Metal Atoms in Helium Droplets:

Exploring the Effect of the Well Depth Using the Coinage Metals Cu and Ag. *The Journal of Physical Chemistry A* **115** (2011) 7141

[9] L. Gomez, E. Loginov, A. Halder, V. Kresin, A. Vilesov. Formation of Unusual Copper Clusters in Helium Nanodroplets. *International Journal of Nanoscience* **12** (2013) 1350014

[10] M. Koch. *Magnetic Resonance Spectroscopy of Single Alkali-Metal Atoms Isolated in Superfuid Helium Nanodroplets.* PhD. Thesis, Graz University of Technology, 2009

[11] M. Ratschek, M. Koch, W. E. Ernst. Doping helium nanodroplets with high temperature metals: Formation of chromium clusters. *The Journal of Chemical Physics* **136** (2012) 104201

[12] M. Ratschek. *Doping Helium Droplets: Development of a High-Temperature Pickup Source.* Master Thesis, Graz University of Technology, 2010

[13] D. R. Lide (Editor). *CRC Handbook of Chemistry and Physics.* CRC Press, Boca Raton, FL, 2005

[14] J. P. Toennies, A. F. Vilesov. Superfluid Helium Droplets: A Uniquely Cold Nanomatrix for Molecules and Molecular Complexes. *Angewandte Chemie International Edition* **43** (2004) 2622

[15] M. Lewerenz, B. Schilling, J. P. Toennies. Successive capture and coagulation of atoms and molecules to small clusters in large liquid helium clusters. *The Journal of Chemical Physics* **102** (1995) 8191

[16] M. Hartmann, R. E. Miller, J. P. Toennies, A. F. Vilesov. Rotationally Resolved Spectroscopy of SF_6 in Liquid Helium Clusters: A Molecular Probe of Cluster Temperature. *Physical Review Letters* **75** (1995) 1566

[17] J. Higgins, C. Callegari, J. Reho, F. Stienkemeier, W. E. Ernst, M. Gutowski, G. Scoles. Helium Cluster Isolation Spectroscopy of Alkali Dimers in the Triplet Manifold. *The Journal of Physical Chemistry A* **102** (1998) 4952

[18] A. Przystawik, P. Radcliffe, S. Göde, K. H. Meiwes-Broer, J. Tiggesbäumker. Spectroscopy of silver dimers in triplet states.

Journal of Physics B: Atomic, Molecular and Optical Physics **39** (2006) 1183

[19] V. Mozhayskiy, M. N. Slipchenko, V. K. Adamchuk, A. F. Vilesov. Use of helium nanodroplets for assembly, transport, and surface deposition of large molecular and atomic clusters. *The Journal of Chemical Physics* **127** (2007) 094701

[20] J. Harms, J. P. Toennies, F. Dalfovo. Density of superfluid helium droplets. *Physical Review B* **58** (1998) 3341

[21] A. Kramida, Yu. Ralchenko, J. Reader and NIST ASD Team (2012). NIST Atomic Spectra Database (ver. 5.0), [Online]. Available: http://physics.nist.gov/asd [2013, May 13]. National Institute of Standards and Technology, Gaithersburg, MD.

[22] F. Delbecq, L. Verite, P. Sautet. Electronic Structure and Magnetism of Ordered Palladium-Manganese and Palladium-Chromium Alloys. *Chemistry of Materials* **9** (1997) 3072

[23] M. Wang, B. Wang, Z. Chen. Magnetic coupling interaction for mixed transition metal dimer: Ab initio MRCI(SD) + Q investigation on CuCr. *Chemical Physics Letters* **435** (2007) 5

[24] A. Kant, B. Strauss, S. S. Lin. Mass-Spectrometric Determination of the Dissociation Energies of the Gaseous CuNi, CuCo, and CuCr. *The Journal of Chemical Physics* **52** (1970) 2384

[25] R. J. Van Zee, J. W. Weltner. ESR of the $^6\Sigma$ CrCu molecule at 4 K. *The Journal of Chemical Physics* **74** (1981) 4330

[26] R. J. Van Zee, J. W. Weltner. Erratum: ESR of the $^6\Sigma$ CrCu molecule at 4 K [The Journal of Chemical Physics 74, 4330 (1981)]. *The Journal of Chemical Physics* **75** (1981) 2484

[27] C. A. Baumann, R. J. V. Zee, J. W. Weltner. ESR of bimetallic transition-metal molecules at 4 K. I. CrCu, CrAg, and CrAu. *The Journal of Chemical Physics* **79** (1983) 5272

[28] J. Jortner, N. Kestner, S. Rice, M. Cohen. Study of Properties of an Excess Electron in Liquid Helium . I. Nature of Electron-Helium Interactions. *Journal of Chemical Physics* **43** (1965) 2614

[29] P. Moroshkin, A. Hofer, A. Weis. Atomic and molecular defects in solid ^{4}He. *Physics Reports* **469** (2008) 1

[30] I. V. Hertel, C. P. Schulz. *Atome, Moleküle und optische Physik 1: Atomphysik und Grundlagen der Spektroskopie.* Springer-Verlag Berlin Heidelberg, 2008

[31] W. Demtröder. *Experimentalphysik 3: Atome, Moleküle, Festkörper.* Springer-Verlag Berlin Heidelberg, 2005

[32] O. Bünermann, G. Droppelmann, A. Hernando, R. Mayol, F. Stienkemeier. Unraveling the Absorption Spectra of Alkali Metal Atoms Attached to Helium Nanodroplets. *The Journal of Physical Chemistry A* **111** (2007) 12684

[33] F. Ancilotto, P. Lerner, M. Cole. Physics of solvation. *Journal of Low Temperature Physics* **101** (1995) 1123

[34] A. Hernando, M. Barranco, M. Pi, E. Loginov, M. Langlet, M. Drabbels. Desorption of alkali atoms from He-4 nanodroplets. *Physical Chemistry Chemical Physics* **14** (2012) 3996

[35] K. Histake, K. Matsuda. A study on diffusion pump oil by the mass spectrometer and the gas analysis of the final vacuum. *Journal of the physical society of japan* **8** (1953) 416

[36] Ted Pella, Inc. *Declaration of the manufacturer: Ted Pella, Inc.* P.O. Box 492477, Redding, CA 96049-2477.

[37] Concept Alloys, 11234 Lemen Road, Whitmore Lake, MI 48189. *Technical Data Sheets for CHROMEL® -P* and ALUMEL®*

[38] Lambda Physik Lasertechnik, A subsidary of Coherent Inc., 289 Great Road, Acton, MA. *Lambda Physik FL3001/3002 Dye Laser Manual*

[39] Radiant Dyes Laser Accessories GmbH. *Declaration of the manufacturer: Radiant Dyes Laser Accessories GmbH.* Friedrichstraße 58, D-42929 Wermelskirchen.

[40] Balzers Instruments Postfach 1000 FL-9496 Balzers Liechtenstein, Postfach 1000, FL-9496 Balzers, Liechtenstein. *Quadrupole mass spectrometer system QMG 422 Operating Manual*

[41] Comar Optics Ltd. *Declaration of the manufacturer: Comar Optics Ltd.* 70 Hartington Grove, Cambridge

[42] J. J. Manura, D. J. Manura. Isotope Distribution Calculator and Mass Spec Plotter, 1996 - 2012
`http://www.sisweb.com/mstools/isotope.htm[2013,April]`

[43] M. B. Knickelbein. Electronic shell structure in the ionization potentials of copper clusters. *Chemical Physics Letters* **192** (1992) 129

[44] M. Kabir, A. Mookerjee, A. Bhattacharya. Structure and stability of copper clusters: A tight-binding molecular dynamics study. *Physical Review A* **69** (2004) 043203

[45] V. Lebedev, P. Moroshkin, J. P. Toennies, A. Weis. Spectroscopy of the copper dimer in normal fluid, superfluid, and solid ^{4}He. *The Journal of Chemical Physics* **133** (2010) 154508

[46] M. D. Morse. Clusters of transition-metal atoms. *Chemical Reviews* **86** (1986) 1049

[47] E. Saloman. A Resonance ionization Spectroscopy/Resonance ionization Mass Spectrometry data service. II-Data sheets for Al, Ca, Cs, Cr, Co, Cu, Kr, Mg, Hg and Ni. *Spectrochimica Acta Part B: Atomic Spectroscopy* **46** (1991) 319

[48] M. Koch, A. Kautsch, W. E. Ernst. One- and two-color resonant photoionization of chromium doped helium nanodroplets. *in preparation* (2013)

[49] A. G. Shenstone. The First Spectrum of Copper (CuI). *Philosophical Transactions of the Royal Society of London. Series A, Mathematical and Physical Sciences* **241** (1948) 297

[50] F. Cargnoni, A. Ponti, M. Mella. Coinage metal exciplexes with helium atoms: a theoretical study of $M^*(^2L)He_n(M = Cu, Ag, Au; L = P, D)$. *Physical Chemistry Chemical Physics* **in press** (2013)

[51] E. Loginov, M. Drabbels. Excited State Dynamics of Ag Atoms in Helium Nanodroplets. *The Journal of Physical Chemistry A* **111** (2007) 7504

[52] D. Mateo, A. Hernando, M. Barranco, E. Loginov, M. Drabbels, M. Pi. Translational dynamics of photoexcited atoms in ^{4}He nanodroplets: the case of silver. *Physical Chemistry Chemical Physics* **in press** (2013)

[53] A. Kautsch, M. Hasewend, M. Koch, W. E. Ernst. Fano resonances in chromium photoionization spectra after photoinduced ejection from a superfluid helium nanodroplet. *Physical Review A* **86** (2012) 033428

[54] D. Leutloff, D. M. Kolb. Fluorescence Spectra of Matrix Isolated Ag and Ag_2. *Berichte der Bunsengesellschaft für physikalische Chemie* **83** (1979) 666

[55] S. Mitchell, J. Farrell, G. Kenney-Wallace, G. Ozin. Optical emission and absorption studies of silver atoms in rare gas matrixes at 12 K; silver atom cryophotoaggregation. *Journal of the American Chemical Society* **102** (1980) 7702

[56] P. Moroshkin, V. Lebedev, A. Weis. Vibronic Transitions of Atomic Bubbles in Condensed ^{4}He. *Journal of Low Temperature Physics* **162** (2011) 710

[57] A. Kautsch, M. Koch, W. E. Ernst. Electronic Relaxation after Resonant Laser Excitation of Cr in Superfluid Helium Nanodroplets. *The Journal of Physical Chemistry A* **in press** (2013)

[58] Pfeiffer Vacuum Technology AG, Asslar, Deutschland. *DualGauge TPG 262 Operating Instructions*, 2004
`http://www.idealvac.com/files/brochures/Pfeiffer_TPG262_Operating_Instructions.pdf[2013,September]`

[59] Voltcraft, Conrad Electronic SE, Hirschau, Deutschland. *Voltcraft k204 Datalogger Manual*
`http://www.produktinfo.conrad.com/datenblaetter/100000-124999/100518-da-01-en-Schnittstelle_Voltcraft_K204_Datalogger.pdf[2013,September]`

[60] D. C. Morton. Atomic data for resonance absorption lines. I - Wavelengths longward of the Lyman limit. *Astrophysical Journal Supplement Series* **77** (1991) 119

A Appendix

A.1 Drawings

A.1.1 Cu Source Lid

A new lid for the Cu-source, made of molybdenum, was constructed (see figure A.1 for technical drawing). The lid was CNC-milled by the institute's workshop, where also a tool for holding the molybdenum sheet while manufacturing was made.

The four flaps of the lid have to be bent by 90 degrees to fit to the crucible. Special care has to be taken not to brake the flaps, especially when bending them back (see figure 3.2 for consequences).

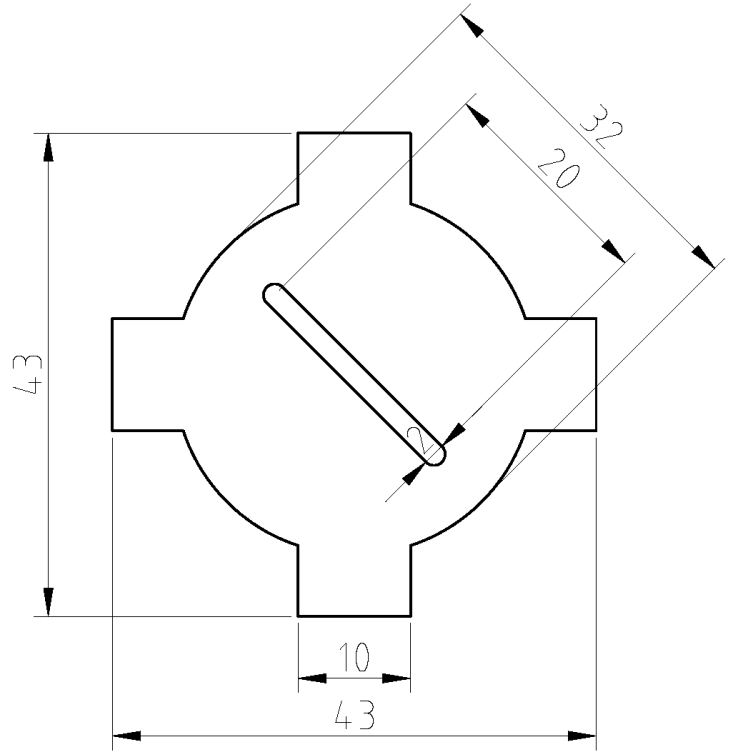

Figure A.1: Tecnical drawing of the Cu source lid. (material . . . molybdenum sheet, thickness = 0.8 mm)

A.2 Programs

A.2.1 Pressure Readout

A proper record of the pressures in the vacuum chambers is very useful for reasons of reproducibility. The following Python™ script reads the pressure values from the pressure gauges in the pickup- and measurement chamber (Pfeiffer Vacuum Dual Gauge and Single Gauge). The script is based on a similar program used by the helium scattering group. Detailed information on the connection and the transfer protocol can be found in reference [58]. This script is a very simple approach which reads out the pressures every given interval inside an infinite loop, therefore to stop the pressure readout, one has to close the Python™ console. The acquisition interval can be altered by changing the value of the variable *aquisition_ interval* to the desired number

of seconds. If the connection of the pressure gauges is changed to a different serial port the according ports need to be changed in lines 32 and 33 of the script. If stopped and restarted the program will continue to write in the same file without deleting the present data.

```
1  import serial    # for communication over RS232
   import time
3  import os

5  aquisation_interval = 120
   CR = '\n'
7  ENQ = '\x05'
   sleeptime_rs = 0.2
9  sensor = '1'

11 def readPressure(port):
       ser = serial.Serial(port, 9600, timeout=5, parity='N',
       bytesize=8, stopbits=1)
13
       ser.write('PR1\r\n'.encode('latin1'))    # send request for
       value of Sensor 1
15     time.sleep(sleeptime_rs)
       ack = ser.read()   # read acknowledgement
17     time.sleep(sleeptime_rs)
       ser.write('\x05\r\n'.encode('latin1'));        # send enquiry
19     time.sleep(sleeptime_rs)
       value = ser.read(ser.inWaiting()) # read value
21     ser.close() #close port
       return value
23
   file1 = open('pressurelog_1.txt','a')
25 file1.write('%Time'+'\t'+'P_mc [mbar]'+'\t'+'P_pc [mbar]'+'\n')
   file1.close()
27
   var = 1
29 while var ==1 :
       file1 = open('pressurelog_1.txt','a')
31
       p_mc = readPressure(1)
33     p_pc = readPressure(4)
       p_mc = p_mc[5:15]
35     p_pc = p_pc[4:12]
```

```
37      print('pressurelog:'+time.ctime()+'\t'+p_mc.decode('utf8')+'\t
    '+p_pc.decode('utf8')+'\n')
        file1.write(time.ctime()+'\t'+p_mc.decode('utf8')+'\t'+p_pc.
    decode('utf8')+'\n')
39      file1.close()

41  time.sleep(aquisation_interval)
```

A.2.2 Temperature Readout

The temperature measurements for the characterisation of the Cu source were carried out with a Voltcraft k204 Datalogger. This device is capable of measuring four temperatures simultaneously with four Type-K thermocouples. The corresponding temperature values were read out with a LabVIEW program (see figure A.2) via a RS-232 connection. A standard LabVIEW example VI ("Basic Serial Write and Read.vi") was used to establish the connection to the device and extended to provide all necessary functions like the conversion of the 45 bit hexadecimal data word to a floating-point number (see reference [59] for a description of the transmission protocol). The Datalogger must be connected to the readout computer via an optocoupler, because otherwise the data transmission fails after some time. It is also important to disable the termination character when initialising the serial connection.

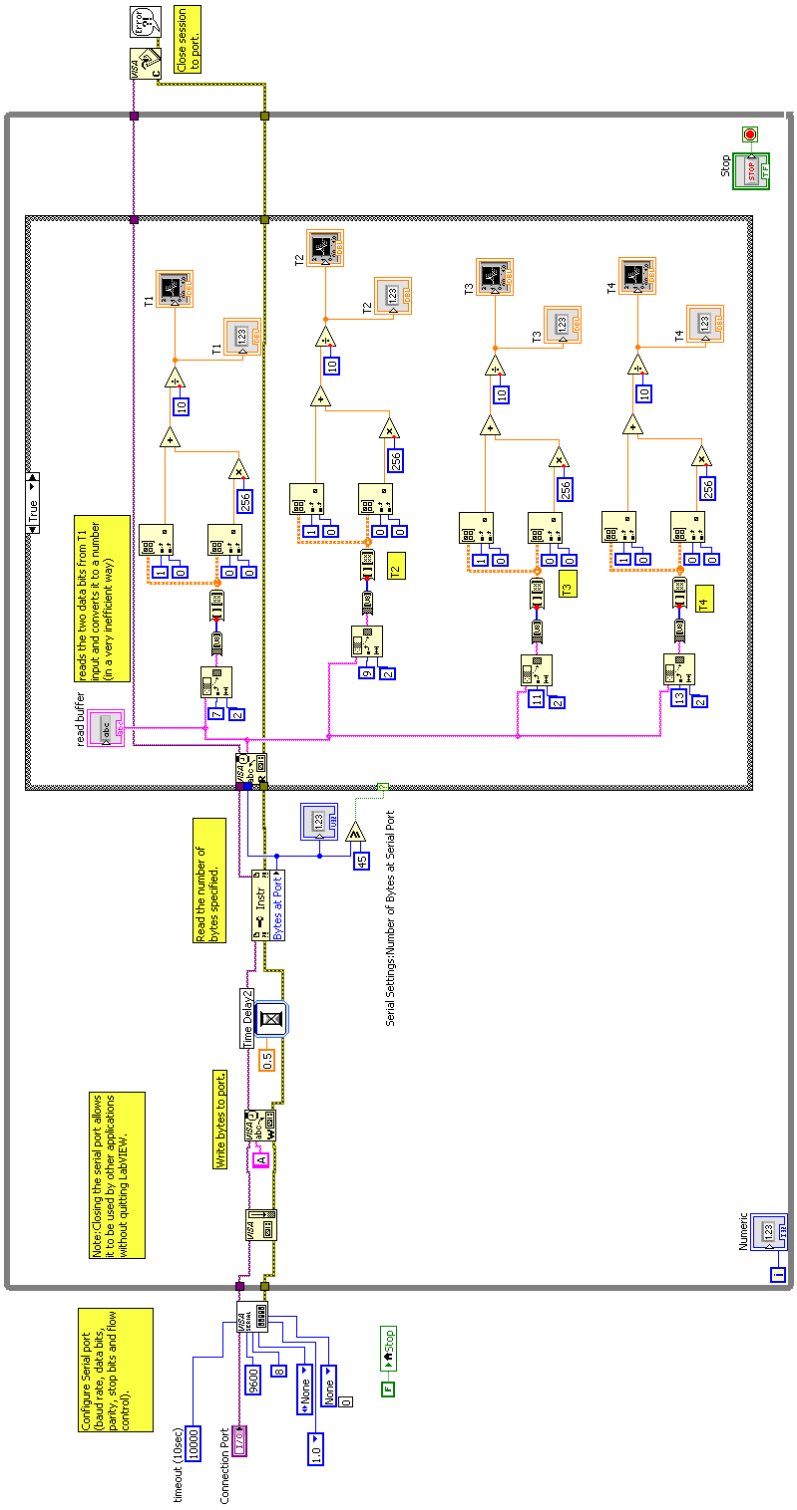

Figure A.2: Temperature Readout program structure.

A.2.3 Wavelength Conversion

The output of the wavemeter in use (Coherent Wavemaster) can be switched between air- and vacuum wavelength. It is sometimes necessary to convert these two quantities afterwards. The IAU (International Astronomical Union) standard for the conversion of vacuum to air wavelength is given by Morton's formula [60]

$$\lambda_{air} = \frac{\lambda_{vac}}{1.0 + 2.735182 \cdot 10^{-4} + \frac{131.4182}{\lambda_{vac}{}^2} + \frac{2.76249 \cdot 10^8}{\lambda_{vac}{}^4}} \tag{A.1}$$

where λ_{air} is the air wavelength in Å and λ_{vac} is the vacuum wavelength in Å. The following MATLAB® function numerically inverts this formula to convert from air- to vacuum wavelength.

```
function [vac] = wavelengthconversion_1(air)

%converts wavelength in air (nm) to wavelength in vacuum (nm)
%by numerical evaluation of IAU-Standard (Mortens formula)

a = air*10;
v = a-100;

treshold = [2,1,0.1,0.01,0.001,0.0001];
step = [1,0.1,0.01,0.001,0.0001,0.00001];

differ = a - v ./ (1.0 + 2.735182E-4 + 131.4182 * v.^-2+ 2.76249E8
    * v.^-4);

for j = 1:length(treshold)
    for i = 1:length(a)
        while differ(i) > treshold(j)
            v(i) = v(i) + step(j);
            differ(i) = a(i) - v(i) ./ (1.0 + 2.735182E-4 +
   131.4182 * v(i).^-2+ 2.76249E8 * v(i).^-4);
        end
    end
end

vac = v./10;
```

```
24 end
```

A.2.4 Control of SHG crystal tilter

The following MATLAB® function is used to calculate the crystal position in accordance to the current dye laser wavelength. The equation in line nine and the coefficients in lines three to seven, relating the crytal position and the fundamental wavelength, are taken from reference [38]. The variables *correct* and *kalib* are attempts to optimise the crystal positioning and need to be adjusted every time the crystal is reinstalled. This function is integrated in the MATLAB® script for operation of the FL3002 dye laser.

```
1  function [CrystalPosAscii]=crystalposition(WL,correct,
       StatischeMatrix)

3  a1c=4.35771719;
   a2c=-0.02089183;
5  a3c=1.900566E-4;
   a4c=-2.702003E-6;
7  a5c=1.700701E-8;
   X0c=588.4;
9  CrystalPosMilliRad=a1c*(WL-X0c)+a2c*(WL-X0c).^2+a3c*(WL-X0c).^3+
       a4c*(WL-X0c).^4+a5c*(WL-X0c).^5;
   CrystalPos=12000-CrystalPosMilliRad./(1000*1.9841E-5)+610;
11
   kalib = -1103.1 + 1.768*WL;  %empirical calibration function
13 CrystalPos = ceil(CrystalPos + kalib);
   CrystalPos = CrystalPos+correct;
15


17 if CrystalPos<1|CrystalPos>23999;
       disp('Crystal reached End!!! Stop loop manually!')
19     pause
       CrystalPos=12000;
21 end

23 disp(['Actual crystal motor counts: ',num2str(CrystalPos)]);
   CrystalPosAscii = DyeLaserDecToAscii(CrystalPos, 4);
```

A.3 A "quick" Guide to Adjust a Pockels Cell

A Pockels Cell (PC) is an optoelectric device which allows to rotate the polarisation direction of light. This is also the usual application of a wave plate, the advantage of a PC is the birefringence that can be controlled by the applied high voltage. At the quarter wave voltage ($V_{\lambda/4}$) the optical path difference of orthogonal polarisations equals a quarter of the light wavelength. At this voltage linearly polarised light is transformed to circularly polarised light. This effect can be used for Magnetic Circular Dichroism (MCD) measurements.

To align a PC one can use a simple setup of two crossed polarisers with the PC in between them (see figure A.3). In the first step the PC is centered to the laser beam. With a setup like in figure A.3, including the lens paper, the screen, and the PC turned off, a structure like in figure A.4a should appear on the screen. The polarisation of the light is disturbed by the lens paper which leads to a pattern, referred to as the *maltese cross*, after passing the PC. The next adjusting step is to center the circles of the maltese cross around the dot of the laser beam by tilting the PC with respect to the laser beam. If a voltage is applied to the PC the pattern is distorted and looks like in figure A.4b.

When all this worked out, the final adjustment is made with the help of a power meter which takes the place of the screen. The lens paper has to be removed and the second polariser should be mounted to allow rotating it around the beam axis. For circularly polarised light ($V_{\lambda/4}$ at the PC) the rotation of the second polariser should not have any influence on the measured laser power and for linear polarised light (0 V at the PC) the difference should be maximal. The task is to find the suitable tilting angles of the PC that satisfies both conditions.

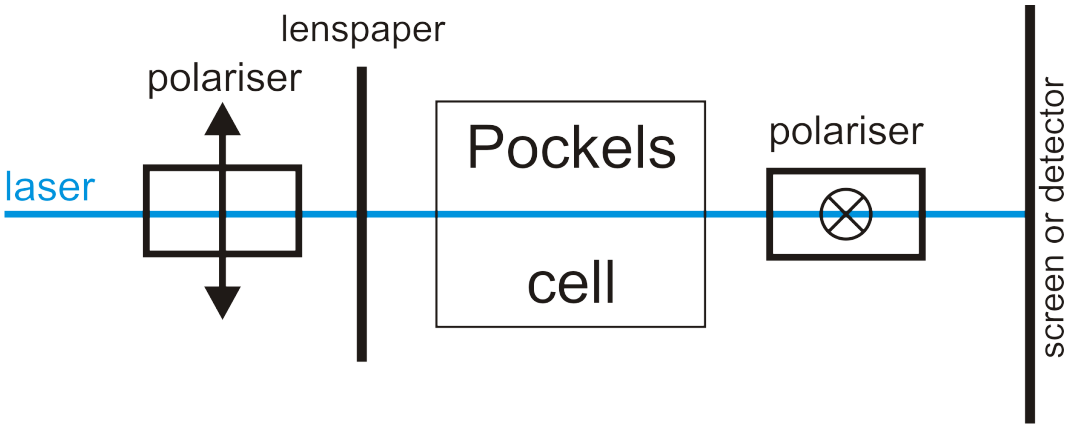

Figure A.3: Setup for Pockels Cell adjustment.

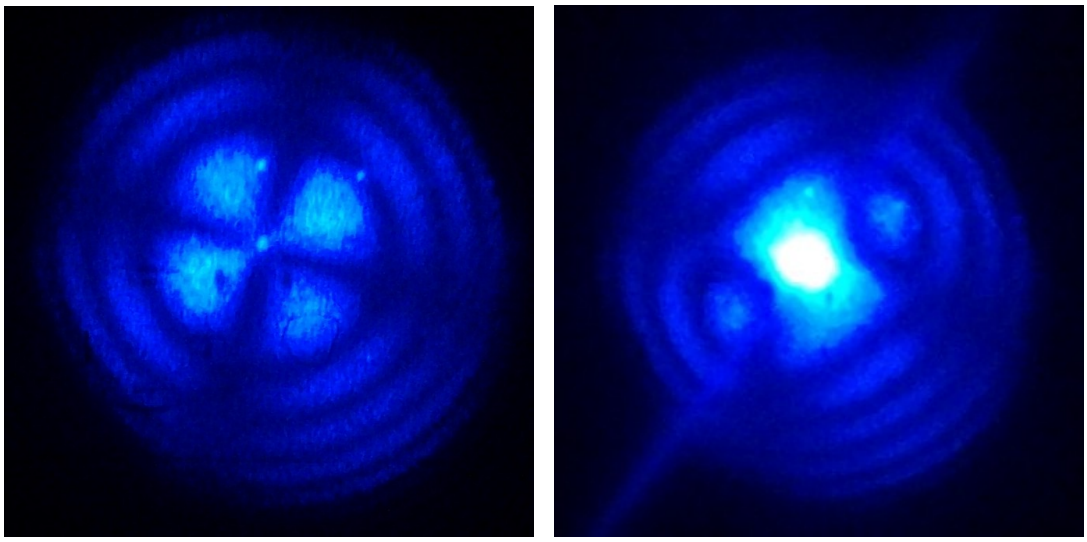

(a) HV off. (b) HV on.

Figure A.4: Characteristic pattern produced by the Pockels cell.